

University of Southern Queensland  
Faculty of Health, Engineering & Sciences

**Tactile sensing instrument design for discriminating  
features of deforming tissue structures within beef striploin**

A dissertation submitted by

W.Marshall

in fulfilment of the requirements of

**ENG4112 Research Project**

towards the degree of

**Bachelor of Instrumentation & Control Engineering**

Submitted: October, 2020

# Abstract

Automation has limited applications in meat processing, as automated cutting devices must follow predictable trajectories while maintaining acceptable line speeds. Primal cuts like striploin display significant variations in physical properties; the way each sample deforms under load is difficult to predict. Recent industry success with x-ray guided robotics for preliminary small-stock carcass processes, has not yet translated into similar results for the beef industry. Imaging devices are being considered for processes like striploin trimming, although research is currently ongoing.

The requirements for manipulating the *in vivo* soft-tissue of humans during robotic assisted surgery differ from those for processing beef workpieces, but increased understanding of deforming tissue structures is evident in the design of robot-assisted surgical manipulators. Real-time response to tissue deformation and haptic feedback to operators of probes, rollers and grippers, enables discrimination of critical states and hidden features within a deforming soft-tissue medium.

This project investigates a modelled tactile sensing scheme, utilising rolling contact to discriminate non-visible structural features of a beef striploin. Evidence based models for static structural deformation and viscoelastic beef tissues are applied to a representative geometric model for striploin. Prototype instrument kinematics and spring force profiles are combined to form a system model to predict wheel-tissue interactions between the instrument and a workpiece with variable composition of fat and lean tissues.

Technology is key for the future of an industry highly dependent on skilled manual labour, sensitive to diverse customer requirements and adverse market fluctuations. Tactile sensing is fundamental in traditional beef processing. Viable complementary technology is likely to emerge with improved understanding of this underutilised sensing mode and the potential for new industrial applications of tactile instrumentation.

University of Southern Queensland  
Faculty of Health, Engineering & Sciences

**ENG4111/2 *Research Project***

**Limitations of Use**

The Council of the University of Southern Queensland, its Faculty of Health, Engineering & Sciences, and the staff of the University of Southern Queensland, do not accept any responsibility for the truth, accuracy or completeness of material contained within or associated with this dissertation.

Persons using all or any part of this material do so at their own risk, and not at the risk of the Council of the University of Southern Queensland, its Faculty of Health, Engineering & Sciences or the staff of the University of Southern Queensland.

This dissertation reports an educational exercise and has no purpose or validity beyond this exercise. The sole purpose of the course pair entitled “Research Project” is to contribute to the overall education within the student’s chosen degree program. This document, the associated hardware, software, drawings, and other material set out in the associated appendices should not be used for any other purpose: if they are so used, it is entirely at the risk of the user.

**Dean**

Faculty of Health, Engineering & Sciences

# Certification of Dissertation

I certify that the ideas, designs and experimental work, results, analyses and conclusions set out in this dissertation are entirely my own effort, except where otherwise indicated and acknowledged.

I further certify that the work is original and has not been previously submitted for assessment in any other course or institution, except where specifically stated.

W.MARSHALL

██████████

# Acknowledgments

I thank my supervisor Peter Brett for his technical guidance and conceptual inspiration, and Fraser Border for his insights into beef robotics research.

Thanks also to my family for their support, understanding and enduring patience, during unusual and challenging times.

W.MARSHALL



# Contents

<b>Abstract</b>	<b>i</b>
<b>Acknowledgments</b>	<b>iv</b>
<b>List of Figures</b>	<b>x</b>
<b>List of Tables</b>	<b>xv</b>
<b>Chapter 1 Introduction</b>	<b>1</b>
1.1 Project Aim . . . . .	1
1.2 Project Justification . . . . .	1
1.3 Objectives . . . . .	3
1.4 Assumptions . . . . .	4
1.5 Project Methodology . . . . .	5
<b>Chapter 2 Literature Review</b>	<b>7</b>
2.1 Australian beef industry automation - Overview . . . . .	7
2.2 Discriminating states and features of deforming tissues using tactile sensing	20
2.3 Modelling the rolling tactile sensor and beef workpiece . . . . .	29

<b>CONTENTS</b>	<b>vii</b>
2.3.1 Geometric Model of the Workspace . . . . .	30
2.3.2 Surface Force Modelling . . . . .	35
2.3.3 Modelling the Wheel-Tissue Interactions . . . . .	35
<b>Chapter 3 Sensor Design</b>	<b>38</b>
3.1 Operational Concept . . . . .	38
3.1.1 Document Overview . . . . .	38
3.1.2 System Overview . . . . .	39
3.1.3 Limitations . . . . .	40
3.1.4 Assumptions . . . . .	41
3.1.5 Functional Requirements . . . . .	42
3.1.6 Design Requirements . . . . .	42
3.1.7 States and Modes . . . . .	43
3.1.8 Operating Environment . . . . .	46
3.1.9 System and Subsystem Components . . . . .	47
3.1.10 Safety/Risk Assessment . . . . .	49
3.2 Mechanical Design . . . . .	49
3.2.1 Hardware Architecture . . . . .	50
3.2.2 Prototype Instrument Product Baseline . . . . .	66
3.3 Design Outcomes . . . . .	69
<b>Chapter 4 Performance Modelling</b>	<b>71</b>



---

4.1	Force Characteristics - Prototype Instrument . . . . .	71
4.1.1	Instrument Weight and Balance . . . . .	71
4.1.2	Spring Force . . . . .	74
4.1.3	Wheel Reaction Force . . . . .	78
4.1.4	Test Rig Towing Force . . . . .	79
4.2	Static Workpiece Deformation Model . . . . .	79
4.2.1	Design parameters into the Static Force Model . . . . .	79
4.3	System Model . . . . .	88
<b>Chapter 5 Results</b>		<b>91</b>
5.1	Prototype Instrument Modelling . . . . .	91
5.2	Static Force Modelling . . . . .	92
5.3	Quasi-Steady System Modelling . . . . .	94
5.4	Design Parameter Sizing . . . . .	96
5.4.1	Workpiece-Trailing Arm Clearance (gap) . . . . .	96
5.4.2	Test Rig Towing Force . . . . .	97
5.4.3	Wheel Dimensions . . . . .	99
<b>Chapter 6 Discussion and Design Review</b>		<b>102</b>
6.1	Modelled Instrument Performance . . . . .	102
6.2	Key Parameters: Instrument and Workpiece . . . . .	105
<b>Chapter 7 Conclusions</b>		<b>109</b>

<b>References</b>	<b>112</b>
<b>Appendix A Project Specification</b>	<b>117</b>
<b>Appendix B Supporting Information</b>	<b>120</b>
B.1 Hazard Analysis and Risk Assessment . . . . .	120
B.2 Spring Datasheet . . . . .	122
B.3 Ultrasonic Transducer Datasheet . . . . .	124
<b>Appendix C Models and Code</b>	<b>126</b>
C.1 Bill of Materials (BOM) Model . . . . .	126
C.2 BOM and System Model Faceplate . . . . .	128
C.3 Model/Function Code (MATLAB) . . . . .	129

# List of Figures

1.1	Roller-based Tactile Sensing Instrument Design Overview . . . . .	5
2.1	Red Meat Processing (in red) - Value-add (a) and Employment (b) . . . . .	8
2.2	Beef Cattle Geographic Distribution in Australia, ABS 2016 . . . . .	9
2.3	Automation, Data and Measurement: Relevance to the Beef Value Chain	10
2.4	Manual Beef Processing: Coupling Visual and Tactile Sensing . . . . .	11
2.5	Large Beef Carcasses at A Teys Facility in Rockhampton. . . . .	13
2.6	Vision-Tactile Sensing modes used to make Z-cuts in European Beef Carcasses	14
2.7	Robotic Visual-Tactile Sensor Fusion - Beef Cutting Research - ARMS Project, France . . . . .	15
2.8	Robotic Beef Processing - Modified Schematic . . . . .	17
2.9	Ultrasonic Scanner used in Pork Processing Automation and in Beef Striploin Trimming Automation Trial . . . . .	18
2.10	Australian Abattoirs - Still not Highly Automated in 2020 . . . . .	19
2.11	Beef Ageing and Isotropic Properties - Electrical (a) and Mechanical (b) .	21
2.12	Deformation Forces for Beef with Parallel Force-Fibre Orientation . . . . .	22
2.13	Wheel-Fat-Meat Composite Layer Compression . . . . .	22

---

2.14	Adipose Tissue Structure and Stress-Strain Relationship . . . . .	24
2.15	Shear Stress-Strain Relationships of Adipose and Connective Tissues . . .	24
2.16	Variations in Young's Modulus for Changes in Strain Rate . . . . .	25
2.17	Beef Deformation with Cylindrical Indenter . . . . .	26
2.18	Rolling indenter Sensitivity to Depth of Tissue Structural Features . . . .	27
2.19	Beef Striploin Tissue Structures . . . . .	28
2.20	Beef Striploin Tissue Structures - Measurements . . . . .	28
2.21	Test Rig Design Drawing . . . . .	31
2.22	Variations in Beef Striploin Surface and Composition . . . . .	31
2.23	Rolling Tactile Sensor Concept Including Test Rig Interface . . . . .	32
2.24	Circular Arch Surface Approximations for Force Modelling . . . . .	32
2.25	Roller-Arch Geometry and Interaction Model . . . . .	33
2.26	Roark's Formulas and Model for a Concentrated Radial Load on a Circular Arch . . . . .	34
2.27	Free Body Diagram (FBD) Example - Wheel over Arch . . . . .	35
2.28	Wheel-Tissue Interaction Models . . . . .	36
2.29	Piecewise Roller Deformation Analysis . . . . .	37
3.1	Operational Concept Diagram - Tactile Sensing Instrument Traversing a Beef Striploin . . . . .	39
3.2	States and Modes - Tactile Sensing Instrument . . . . .	44
3.3	Initialisation Mode - Tactile Sensing Instrument . . . . .	45

---

3.4	Active Mode - Tactile Sensing Instrument . . . . .	46
3.5	System-Subsystems Schematic Diagram - Tactile Sensing Instrument . . .	47
3.6	Functional Block Diagram - Tactile Sensing Instrument . . . . .	48
3.7	Workspace Reference Plane (x-y) Including Instrument, Workpiece and Test Rig Work Surface . . . . .	51
3.8	Minimum Edge Distance and Spacing for Holes in accordance with EN-1993	53
3.9	Key Wheel Dimensions for System Design . . . . .	53
3.10	Wheel Details Including Material Thickness and Geometric Simplifications	54
3.11	Wheel-Yoke-Arm Detail Drawing - 25mm Radius Wheel - 6mm Diameter Wheel Bore . . . . .	55
3.12	Trailing Arm Component Dimensions and Profile . . . . .	56
3.13	Trailing Arm and Roller Dimensions and Clearances . . . . .	57
3.14	Circle Segment Definition and Mathematics . . . . .	58
3.15	Wheel-tissue Interactions with Modelled Trailing arm and Wheel Mecha- nism for Deforming Workpiece . . . . .	59
3.16	Spring Buckling, Slenderness Ratio, Compression ratio, End Fixture . . .	61
3.17	Spring Mechanism - Parts and Assembly Drawings . . . . .	63
3.18	Prototype Instrument and Workpiece Scale Drawing . . . . .	66
3.19	Wheel BOM and Piece-part Drawing . . . . .	67
3.20	Trailing arm BOM and Piece-part Drawing . . . . .	67
3.21	Yoke BOM and Piece-part Drawing . . . . .	68
3.22	Spring Mechanism BOM . . . . .	68

---

3.23 Spring Mechanism Piece-part Drawing . . . . .	69
4.1 Preloaded Instrument FBD . . . . .	72
4.2 Instrument in Sensing State FBD . . . . .	72
4.3 Centre of Gravity - Trailing arm and wheel Assembly . . . . .	73
4.4 Static Force Balance in the Work Space . . . . .	74
4.5 Spring Mechanism Detailed View - Spring Length and Angles . . . . .	76
4.6 Circular Segment Formulas for Spring Motion . . . . .	76
4.7 Equivalent Arch - Modelled Workspace and Roark's Formulas . . . . .	80
4.8 Roark's Formulas for a Concentrated Radial Load with Right End Fixed .	80
4.9 Roark's Equivalent Arch Refined in Terms of Instrument and Workpiece Parameters . . . . .	81
4.10 Equivalent Arch and Wheel in the Workspace . . . . .	82
4.11 Static Deformation Results - Wheel Elevation $C_y$ for Non-Deforming Sur- face, 12mm and 4mm Thick Fat Layers . . . . .	86
4.12 Simplified Static Elastic Deformation of the fat Layer . . . . .	87
4.13 System Model - Tactile Sensing Instrument and Beef Striploin Workpiece	88
4.14 Kelvin-Voigt Viscoelastic Model . . . . .	88
4.15 35mm Wheel Deforming the Surface 10mm . . . . .	90
5.1 Spring Compression Ratio over the Length of the Trailing Arm . . . . .	92
5.2 Drawing Package Dimensions to Verify Spring Compression Range . . . . .	92
5.3 Wheel Reaction Force over the Workspace . . . . .	93

---

5.4	Static Deformation Results - Wheel Elevation Cy for Non-Deforming Surface, 12mm and 4mm Thick Fat Layers . . . . .	94
5.5	Quasi-static Deformation Time Response - 4mm Fat Layer over Viscoelastic Workpiece . . . . .	95
5.6	Deformation of Different Fat Layer Thickness at Average Peak Sampling Time . . . . .	96
5.7	Wheel-tissue Interactions with Modelled Trailing arm and Wheel Mechanism for Deforming Workpiece . . . . .	97
5.8	Wheel Reaction Force x-axis and y-axis Components over the Workpiece .	98
5.9	Spring and Test Rig Force Contributions for Static Equilibrium . . . . .	98
5.10	Wheel Width Variations and Effect on Deformation Predictions . . . . .	99
5.11	35mm Wheel Deforming the Surface 10mm . . . . .	100
5.12	Local Deformation Stress Under Different Wheel Dimensions . . . . .	101
6.1	Comparison of Wheel-tissue Contact for Viscoelastic and Elastic Materials	104
6.2	Key Design Parameters - Tactile Sensing Instrument and Workspace . . .	105
B.1	Hazard Analysis & Risk Assessment. Template adapted from . . . . .	121
C.1	Design Calculation Model for the Bill of Materials (BOM) . . . . .	127
C.2	BOM and System Modelling Faceplate . . . . .	128

# List of Tables

6.1 Key Design Parameters . . . . .	105
-------------------------------------	-----



# Chapter 1

## Introduction

### 1.1 Project Aim

To design a roller-based tactile sensing device that will provide a guide for cutting machines, separating fat tissues from muscle when trimming primal beef cuts. The investigation supports development of suitable design parameters, to enable evaluation of functional performance using analytical tools.

### 1.2 Project Justification

The outcomes of this project have the potential to support advances in automation technology for the beef processing industry. Real-time sensing and discrimination of key features in non-visible tissue interfaces could enhance machine perception capabilities to guide cutting devices in high-value beef processing applications.

The Australian red meat and livestock industry is a significant contributor to the national economy. The red meat processing sector has experienced 5-yearly growth in turnover of only half that seen in on-farm beef production (Meat & Livestock Australia Limited 2019). This equates to approximately one quarter of the overall industry turnover, 15% of the value-add from goods produced by the industry and only 3% of value added to the Australian manufacturing industry. The export value of processed meat however, is 90% of the 15 billion dollar/year meat and livestock export industry. The large volumes

of available stock, relatively high export value and demand, contrasted with significantly lower growth and negligible value-adding impact across industries, suggests that beef processors may be constrained by current work practices and the availability of effective automation technology. Food product manufacturing, the highest value-adding sector in Australian manufacturing (Meat & Livestock Australia Limited 2019), adds over five times the value of goods in manufacturing compared to meat processors. Automation is a key component in the processing and manufacture of food and other products.

The numbers of workers employed in beef processing are also significantly lower than those in on-farm production, although processing contributes to twice the number of indirect jobs for every person employed compared to production (Meat & Livestock Australia Limited 2019). The meat processing worker numbers lag those in other food manufacturing by the same proportion as the value added by each industry. The impacts of automation appears to include an increase in the productivity of an industry, and the evidence suggests that the number of workers employed by an automated industry can also increase. The beef processing industry is limited by the high cost of labour in Australia, accounting for 70% of costs (Australian Competition & Consumer Commission (ACCC) 2017), in an international market where major competitors such as the United States and Brazil see processing cost per-head of half to two-thirds of Australia's cost respectively. Beef processing has only a few major stakeholders in the industry, with 5 plants across Australia employing more than 100 people in 2018 (Meat & Livestock Australia Limited 2019). Processors establish facilities in geographical locations constrained by the distances to grazing land, competition from other processors and availability of export facilities. The availability of skilled labour in these regions is critical to production utilising manual processes, particularly beef boning, cutting and trimming of high-value primal cuts of beef.

Automated beef processors of the future, have the potential to boost regional labour opportunities, where workers would be required in supply-chains and technical supervision or maintenance activities. The beef processing industry could grow across more regions of Australia, improving employment and skills-based education outcomes.

Finally, tactile sensing technologies have not been applied to beef processing research and industry trials to the same extent as radio frequency (RF), X-ray and laser technologies for example (Greenwood, Gardner & Ferguson 2018), (Meat & Livestock Australia Limited 2015). It is interesting to note that medical research and technological advancements

in robotic surgery and minimally invasive techniques, is being supported in part, by understanding the potential for tactile sensors to guide robotics. Tactile sensing in medical research and practice, occurring within an environment where RF/X-ray/laser imaging and diagnostic equipment are already commonplace. It makes sense that research into effective, safe and sustainable automation for an industry dependent on human tactile sensing capabilities, considers the potential for instrumentation that builds upon this well established functional baseline with complementary technologies that support growth right across this high-value industry sector.

### 1.3 Objectives

1. Investigate relevant literature, information and similar work involving beef industry automation, robotics and meat cutting.
2. Investigate relevant literature, information and similar work involving tissue deformation in response to applied force (stress), influence variables such as temperature and relevant sensing techniques and technology.
3. Model the tool-tissue interactions expected during operation of a roller-based sensing scheme used to discriminate features of tissue deformation in a beef workpiece.
4. Derive technical specifications and determine assumptions for a roller-based tactile sensor system design.
5. Design the tactile sensing scheme. Specify the range of operating conditions, output presentation and intended interface design for mechanical and electronic considerations. Develop engineering artefacts including specifications, drawings and verification plan.
6. Model the performance of the tactile sensing system, within the context of discriminating critical states and features of beef striploin primals with observable tissue structure and deformation.

## 1.4 Assumptions

1. The restrictions imposed on Australians during the COVID-19 pandemic have resulted in USQ policies preventing staff and student access to a range of USQ facilities and resources. The design of this sensor is not supported by hardware manufacture, experimentation or measurements in a laboratory. Models have been developed, based on related research into soft tissue behaviour and other formal techniques to predict structural deformations of materials under load. The results of modelling, combined with the engineering artefacts detailing the instrument design, are assumed to be adequate to support future manufacture and experimental work
2. The models applied during the instrument design are assumed to be a suitable starting-point for establishing an understanding of the tool-tissue interactions between the instrument and a deforming workpiece. The geometric form, viscoelastic properties and structural composition of a soft-tissue sample are key characteristics influencing the physical behaviour of a beef sample under load. While the model parameters have been determined through analysis of methods and results in the literature, there will likely be modifications required to refine and build upon models needed to support a prototype instrument
3. Each beef striploin sample is different, with unique characteristics that make tactile sensing with a single instrument difficult. Assuming that future experimental work will lead to better understanding of the tool-tissue interactions between beef and the instrument, adjustments to the instrument geometry and tactile response characteristics will be required. The prototype instrument has been designed to be adaptable to change and supportable with low-cost, off-the-shelf components as well as custom component manufacturing with 3D printing if available
4. Design-specific assumptions are detailed further in Section 3.1.4.

## 1.5 Project Methodology

A review of the beef processing industry in Section 2 (Project Objective 1) has identified the need for efficient automated processes that deliver productivity, quality and maximum value-add to the industry, by optimising the deployment of automation technology and human labour. Current trials and a small number of new system integrations however, aim to replace the tactile sensory modality of human workers with vision/imaging systems designed to guide robotic cutting devices. This project seeks to address the salient issues facing the industry, while investigating the sensor-technology gap identified in the literature. The subsequent design process is informed by reported customer requirements, detailed analytical modelling and an appreciation of the rich source of information available from the energy-flows within a tactile sensing scheme.

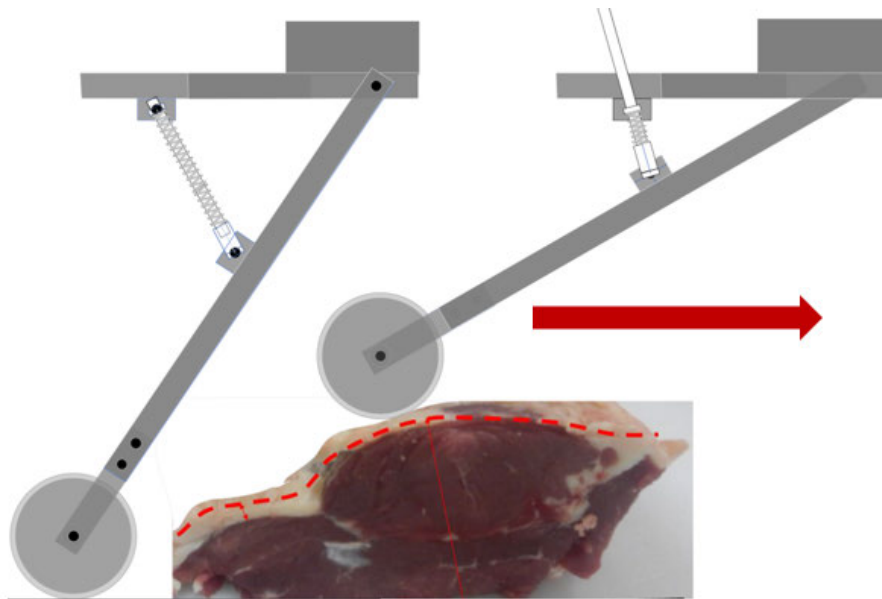


Figure 1.1: Roller-based Tactile Sensing Instrument Design Overview (Meat image: (Khodabandehloo 2016))

Striploin is removed from a bovine carcass with a layer of fat over one surface, distributed in non-uniform thicknesses across the workpiece. Industry representatives have specified the range of observed variability in physical striploin parameters, a target range for trimmed fat layer thickness, as well as key metrics for the throughput expected in a viable automated processing facility. The design decision to implement a roller-based mechanism addresses the key functional requirements to implement technology that scans one striploin in 15 seconds to discriminate the variations in fat thickness and guide a cutting

device that trims the fat layer to within 4 - 12mm thickness (Khodabandehloo 2016).

The wheel needs to be supported as it traverses the highly variable range of workpiece geometries. The mechanism must not contact the surface other than at the wheel-tissue interface, and a test rig apparatus provided by the USQ Centre for Agricultural Engineering (CAE) provides the drive-force to move the mechanism at a user-adjustable speed and elevation above the work surface. These important interfaces are managed by the formal design process detailed in Chapter 3, where functional and derived technical requirements are defined and allocated to design (Project Objective 4).

The analytical design tools in Chapter 3 support a product baseline from which to manufacture a prototype instrument (Project Objective 5). The prototype kinematics are applied to a model workspace in Chapter 4 to establish spring-force profiles at the wheel-tissue contact surface. Static deformation within the representative workpiece tissue structure is conducted using a specific form of Roark's formulas for stress and strain that applies to a small beam in an arched geometry (Young & Budynas 2002). The literature review (Project Objective 2) has informed the determination of a reasonable magnitude of Young's modulus for the fat layer in the static deformation model (Comley & Fleck 2012). Other reported mechanical characteristics of adipose tissue (fat) in the literature include the isotropic cellular structure of fat and compression, tension and shear (Yoo, Gupta, Lee, Kavehpore & Demer 2011) strain test results, which have been considered in optimising the initial model.

Further investigation of similar work involving tissue deformation and sensing techniques, identified a suitable viscoelastic model (Kelvin-Voigt) to apply to the muscle tissue component of the composite system model (Moreira, Liu, Zemiti & Poignet 2012) (Project Objective 3). The classical spring-damper models are reported to be suitable reference models for real-time force control systems, in contrast to finite element models (FEM) for example. Sangpradit, Liu, Dasgupta, Althoefer & Seneviratne (2011) have reported that a FEM-based rolling indenter model can take in  $\approx 10$  minutes to process a 150mm scan over a deforming surface.

The system model has been run for a 35mm radius wheel over a 100mm representative striploin arch, with performance measures including the predicted discrimination of fat layer thicknesses of 4, 12, 20, 30 and 50mm (Project Objective 6).

## Chapter 2

# Literature Review

### 2.1 Australian beef industry automation - Overview

The Australian beef industry is the third largest exporter of beef behind Brazil and India (Meat & Livestock Australia Limited 2019) (Greenwood et al. 2018). Australian beef consumption per capita was approximately three times the world average in 2018, with the world's consumption of beef increasing 1% per year over the last two decades (Meat & Livestock Australia Limited 2019). The export value of processed red meat is significant, providing around 90% of meat and livestock export returns in 2018 (Meat & Livestock Australia Limited 2019) and similarly in 2014-15 (Australian Competition & Consumer Commission (ACCC) 2017). The high cost of processing meat in Australia is evident in relatively low impact 3% value-add in the manufacturing sector and low levels of growth year-on-year in the red meat processing sector (Meat & Livestock Australia Limited 2019). The Australian Competition & Consumer Commission (ACCC) (2017) also report significant reductions in beef processing businesses since the 1980s, with some efficiencies being created through automation and the processing capacity increasing through efficiencies of scale. Beef Central (2019) claim that government regulation is crippling the beef processing industry, with labour and energy costs also reported to be significant obstacles to success in the global market. The graphics in Figure 2.1 from Meat & Livestock Australia Limited (2019) show the relatively small impact of value-add from red meat in the food manufacturing sector (a), while the employment numbers are relatively steady over time in the processing sector (b), where increases were due largely to beef/mixed farming and live-export related activities.

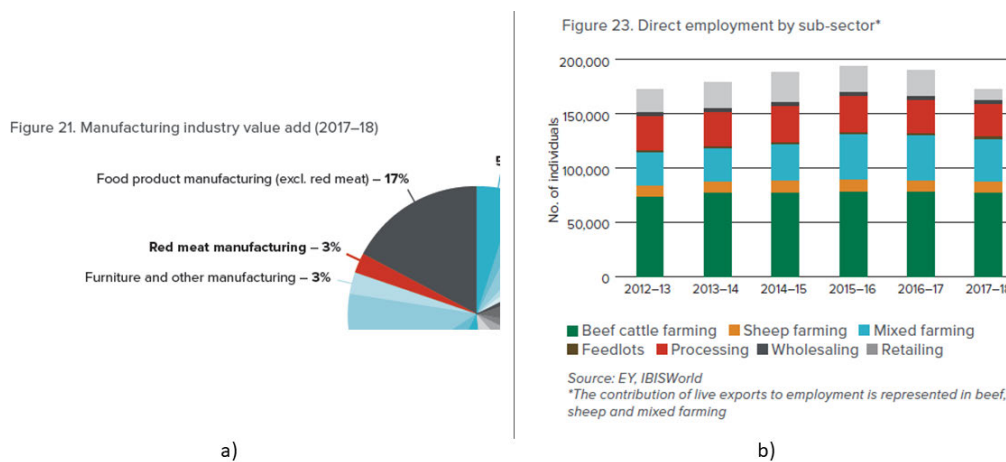


Figure 2.1: Red Meat Processing (in red) - Value-add (a) and Employment (b) (Meat & Livestock Australia Limited 2019)

The scale of processed beef supply domestically is strongly influenced by supermarket demand and processing requirements for small number of processors, who engage in long term contracts to provide beef products that service shopping centre customer impulses and convenience (Australian Competition & Consumer Commission (ACCC) 2017). The case for automation should be strong therefore, when product specifications are consistent over time and processors avoid unexpected configuration changes and re-tooling. Teys Australia has a significant stake in domestic beef processing capabilities (Australian Competition & Consumer Commission (ACCC) 2017), and the company has supported ongoing research and development of automation for the industry through co-funding a research facility in a plant at Rockhampton, Queensland (Fairfax Media 2019).

The advancement of automated beef processing may address problems associated with the concentration of a small number of processors in particular areas of the country (Australian Competition & Consumer Commission (ACCC) 2017), which impacts the outlying regions of northern, southern and Western Australia for example where large herds are present but processing options are limited (see Figure 2.2). Graziers face constraints around viable breeds, climate, transport distance and ultimately the capabilities of a processor to accept different types and size of animals to meet particular requirements. Some producers are limited to live exporting due to lack of viable processing options or none at all (Australian Competition & Consumer Commission (ACCC) 2017).



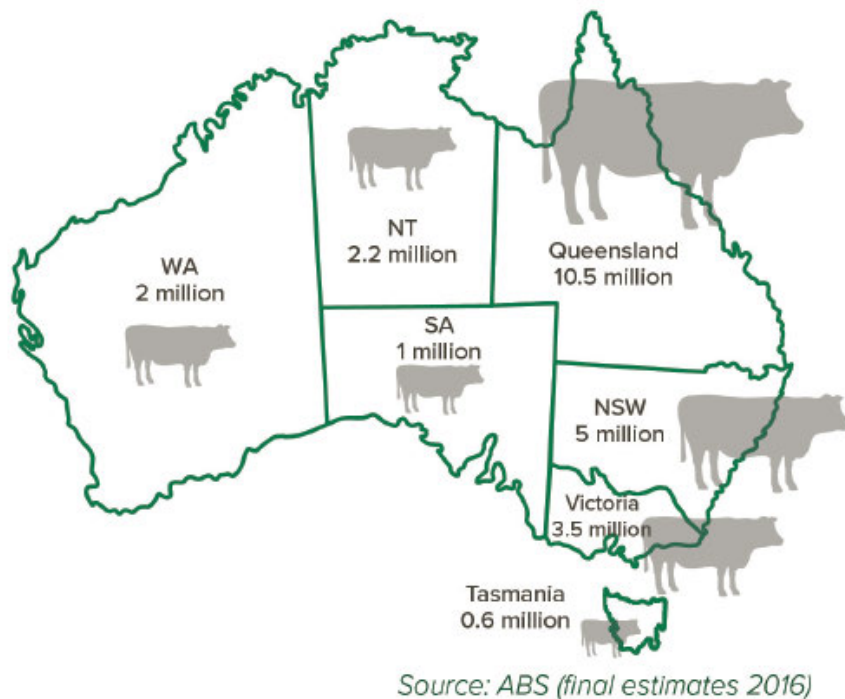


Figure 2.2: Beef Cattle Geographic Distribution in Australia, ABS 2016 (Greenwood et al. 2018)

The evidence suggests that traditional, manual processing of beef products is likely to contribute to producers and processors missing out on the potential returns from the expanding domestic and global demand for beef. When more affordable, robust automation and advanced process control technologies become available, there may be opportunities for smaller processors to invest in automation in more facilities across Australia. Flexible, adaptive technology could open up new, high-value markets for beef. This may include mainstream domestic supermarket supply chains with tight product specifications, who currently have influence over the limited number of large-scale processors in some regions. Alternatively, more high-value niche markets in restaurants and butcher shops (Australian Competition & Consumer Commission (ACCC) 2017) may be an option, when government, transport, energy and labour costs (Beef Central 2019), (S.G. Helibron Economic & Policy Consulting 2018) are alleviated by regional networks of smaller, agile processing plants. The need for automation, big-data and objective measurements in the beef value chain is well documented and supported in the literature (Greenwood et al. 2018), (Meat & Livestock Australia Limited 2015), (Cook, Martchenko, Hughes, Shirazi & Starling 2017), (Sim 2019), (Condon 2019).

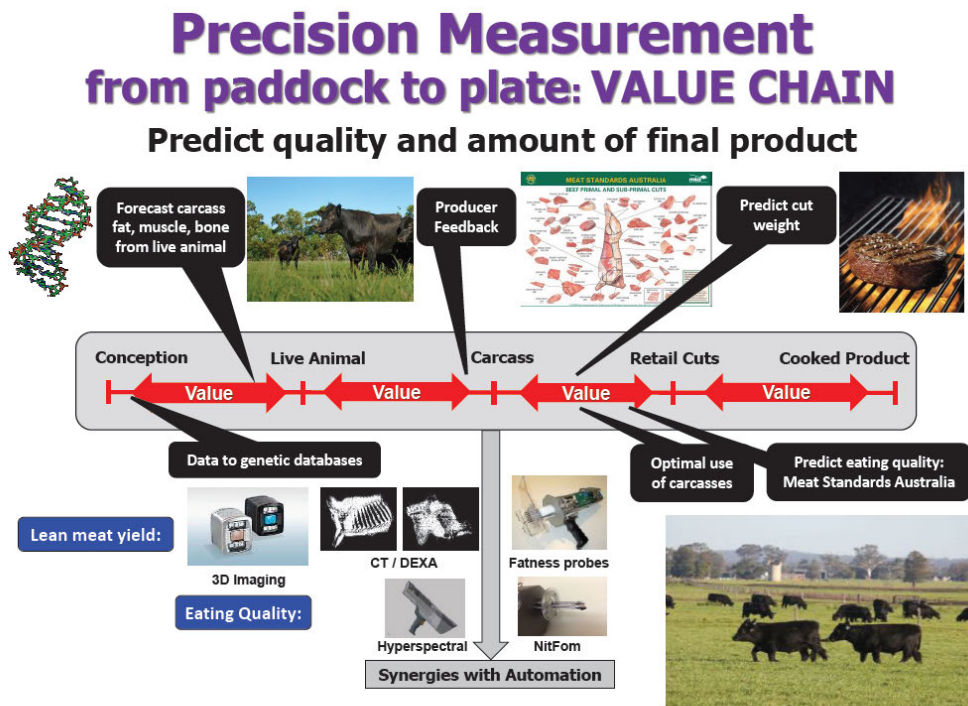


Figure 10. Objective measurement technologies and data links across the Australian beef value chain will enable feedback from the market and better management decisions to improve production and processing efficiencies and compliance with market specifications.

Figure 2.3: Automation, Data and Measurement: Relevance to the Beef Value Chain (Greenwood et al. 2018)

Automation and advanced process control for beef processing is the focus of Teys Australia in Rockhampton (Fairfax Media 2019), the University of Southern Queensland (Border, Khodabandehloo & Brett 2019) and the Australian Meat Processor Corporation (Khodabandehloo 2016). In France, similar research has been conducted into robotic cutting techniques (Nabil, Belhassen-Chedli & Grigore 2015) and technology solutions that seek to address labour shortages and working conditions for beef processors (Guire, Sabourin, Gogu & Lemoine 2010). Objective measurement technology is a feature of the recent work in Australia (Meat & Livestock Australia Limited 2015), (Cook et al. 2017), and the application of equipment typically associated with medical facilities is common across the Australian research into beef processing technologies. X-ray, Magnetic Resonance Imaging (MRI), laser spectroscopy, hyper-spectral imaging, electrical probes (Meat & Livestock Australia Limited 2015) and ultrasound (Khodabandehloo 2016) are examples of the technology being implemented or considered.

The industry focus to date appears to be on replacing the tactile sensing functions of human workers with vision and imaging equipment. This technology provides information about the hidden features of a workpiece and has been used to guide cutting tools with

whole carcasses, which have bone structures and some dynamic stability. Limited success is evident however, in beef processing applications for soft tissues that deform under loads at the tool-tissue interface.



**Fig. 1.** Separation steps of the round and shank of beef muscles.

Figure 2.4: Manual Beef Processing: Coupling Visual and Tactile Sensing (Nabil et al. 2015)

Dual-energy X-ray absorptiometry (DEXA), applicable to bone density, fat and muscle distribution measurements (Meat & Livestock Australia Limited 2015), has been integrated into lamb processing facilities (Sim 2019) owned by Australia's largest meat processing employer (Meat & Livestock Australia Limited 2019) JBS Australia . The JBS Australia farm assurance and supply chain manager claims that the investment in DEXA-based robotic boning of lamb carcasses, implemented in 2015, was paid-back in 3 years at one of their plants (Sim 2019). The further impacts of automation realised by JBS Australia and reported by Sim (2019) include:

1. Coupling DEXA imaging with robotics was critical in boosting the value of lamb processing since 2015, with accurate cutting lines to maximise return on high-value cuts
2. Reducing human contact with meat increases shelf-life, which supports export market opportunities with the United States for example
3. Data from DEXA scanning is also used to provide feedback to producers in terms of yield and other animal physical/health characteristics. This also adds value to the product however, the critical return on investment would likely take too long through carcass measurements and data alone; the DEXA-robotics coupling is considered necessary for real cost-benefit

The Meat and Livestock Australia (MLA) general manager also commented on DEXA-based automation in the Sim (2019) report, with respect to possibilities for the beef processing industry:

1. DEXA-based automation will continue to be implemented in small stock processing plants (e.g. sheep), but the uptake in large beef carcass facilities will be limited
2. The second largest employer of meat processors, Teys Australia (Meat & Livestock Australia Limited 2019), is trialling this automation technology in Rockhampton. Widespread adoption of this system is not likely across the beef processing industry, in the short term.

Condon (2019) reports further on the automation of beef processing at Teys' Rockhampton research facility:

1. DEXA and computer-aided tomography (CT) technology would be used to guide robotics in cutting tasks
2. A number of robotic installations would be required to focus on different parts of the beef carcass, requiring guidance from DEXA and CT scanners
3. Robotic cutting would ensure high-value segmentation of the beef carcasses, preparing the beef workpieces for further processing tasks carried out by humans
4. A Teys representative estimates a timeline of 5-7 years or possibly longer for the research project into DEXA/CT for beef processing
5. Teys also claim that the most difficult aspect of implementing automation is the sensing and analysis of carcass properties, compared to the task of guiding the trajectory of robotics
6. Teys are sharing knowledge derived from research conducted at the Rockhampton R&D facility. Potential technology solution providers are invited to use the facility for future projects, subject to MLA and Teys approval.



Figure 2.5: Large Beef Carcasses at A Teys Facility in Rockhampton (Condon 2019). (Note relative size and physical variability over the sample).

The European experience with X-rays and robotics in beef processing is similar to that reported by Australian industry and researchers. Some success has been forthcoming with sheep and pigs, due in part to less variation in physical carcass characteristics (Guire et al. 2010). The variability of beef cattle dimensions (250-400kg and 1.7 to 2.2m spine length) combined with the cultural/regional and quality considerations regarding the European specifications for beef primal cuts, makes the application of this technology more difficult for beef processors.

Tactile sensing technology does not receive detailed investigation within the available Australian literature, however research in Europe provides an insight into possibilities for such technology in beef processing automation. The work of Guire et al. (2010) was in response to the issues with X-ray guided robotics outlined earlier. Rather than use X-ray imaging to determine cutting trajectories, the researchers fused vision and tactile sensors to establish what is termed the Z-cut, which separates the beef half-carcass into fore and aft quarters.

The vision and tactile sensing systems of Guire et al. (2010) combine to form the basis of control for three main phases of robotic cutting:

1. Vision to establish theoretical cutting path
2. Tactile sensing and control to follow a path based on force feedback. e.g. following a bone with the blade edge
3. Vision-tactile sensor fusion to adjust the blade position to find a prescribed level of force feedback at particular regions of the carcass.

Figure 2.6 shows the vision system lighting reference marks (left) and the force-sensitive robot controlled blade (right) following a cutting trajectory. Some challenges include:

1. As the process involves the right and left hand sides of the carcass separately, the operators found that different positioning and orientation of carcasses was required to enable success within the constraints of the robotic-cell workspace
2. The Z-cut is a relatively well defined cutting path, guided in part by ribs and the spine of the carcass. Future work on more complex beef processing operations would require increased capacity of the robotic cell to adapt to each task.

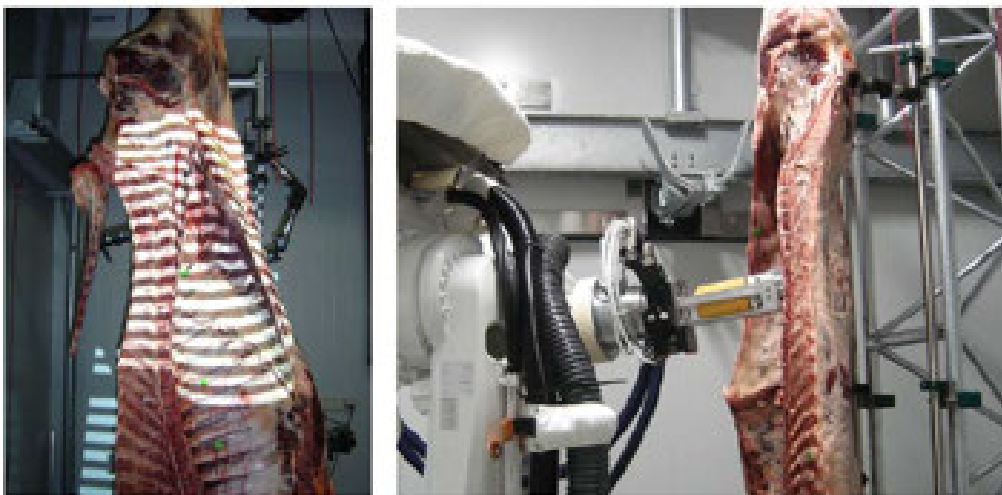
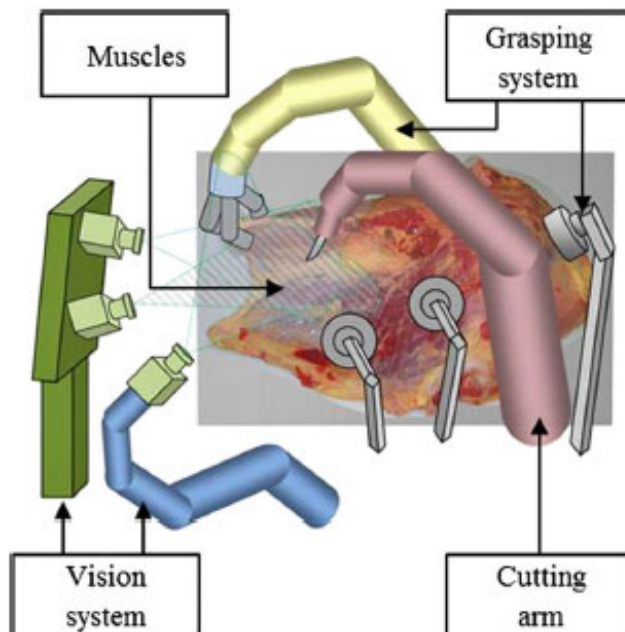


Figure 2.6: Vision-Tactile Sensing modes used to make Z-cuts in European Beef Carcasses (Guire et al. 2010)

The challenge of increasing the adaptability and capacity of a robotic cell in more complex cutting tasks has been demonstrated in the work of Nabil et al. (2015), also in France. The imaging systems described so far, whether passive camera-based vision or active RF/X-ray/ultrasonic emitter-based imaging systems, have advanced the machine



perception capabilities of robotics. Nabil et al. (2015) suggest however, that this is only a starting point in task definition and dynamic perception. The dynamic capabilities require additional support when cutting tasks become more complex, in the case of purely soft material manipulation for example when bones and other references are not available. Soft material modelling is suggested to be a potential capability enhancement for robotic cutting. Appropriate geometric models of the workpiece and force models involving classical mass-spring approximations for example, combine to inform predictions of the soft material deformations under load. The tool-tissue interactions are key feedback parameters of the force-control system, while vision sensors monitor and update the geometric model of the deformable material (meat) being manipulated. Figure 2.7 shows how visual-tactile sensor fusion is applied in the model-based robotic cutting system.



**Fig. 2.** Task adaptation of muscle separation proposed in the ARMS project. Transcription of meat muscle separation tasks into robotized actions and systems.

Figure 2.7: Robotic Visual-Tactile Sensor Fusion - Beef Cutting Research - ARMS Project, France (Nabil et al. 2015)

The researchers have acknowledged the collaboration with organisations in their local meat processing industry (Nabil et al. 2015). These research partners provided guidance in performing quality, complex manual beef-cutting operations, which was used to formulate geometric models and design experimental tests to characterise beef muscle characteristics. Building on the strengths of the beef processing industry is also a goal of the tactile instrumentation design presented in this report. Inspection of the hardware

architecture in Figure 2.7 does suggest that the system is heavily reliant on robotic resources, with 3 arms required for one cut. Although as Border et al. (2019) point out, these complex automation tasks must also include a strategy for supporting the workpiece during processing, including consideration for the prevention of bruising and damage.

Modelling a workpiece with a detailed finite element model (FEM) also presents a problem for beef product variations such as inhomogeneous tissue structures and the different size and shape of workpieces described across the available literature. A highly adaptable model or library would likely be required to support the system in an automated industrial setting.

Another potential challenge, not obvious from the diagram, is the computational resources and time required to resolve complex finite element models. The researchers do acknowledge that this is a limitation of FEM for real-time system applications, and that modelling needs to be optimised once critical states and features of the deformable materials are understood. Important concepts were investigated with the more complex models, such as the anisotropic behaviour of beef where reaction forces at the tool-tissue interface are different depending on the relative alignment of muscle fibre directions, also described by Damez & Clerjon (2008) and Honikel (1998). The operational models developed by Nabil et al. (2015) are derived from the initial FEMs, and demonstrate the application of classical mass-spring and tensor-mass elastic models. The limited applications for FEM in real-time systems is also acknowledged by Sangpradit et al. (2011) and Moreira et al. (2012), suggesting that classical viscoelastic models such as the Kelvin-Voigt, Kelvin-Boltzmann and other spring-damper configurations are more suitable for tactile sensing systems used to control tool-tissue interactions. The application of simple, viscoelastic models over purely elastic approximations of natural soft tissues is examined further in the next sections. Beef and similar tissue structures are shown to exhibit viscous damping in conjunction with linear spring action, when loaded by external forces from tools that indent and otherwise deform the tissue structure.

Australian researchers are investigating the advancement of automation in complex beef processing tasks, potentially adding value downstream from the initial carcass processes such as boning and portioning. Striploin primals are one product for which the value-add may be improved through novel automated techniques, particularly targeting the removal of excess fat tissue from the surface of beef striploin pieces. (Border et al. 2019) identify promising approaches to beef automation and machine perception which, as outlined in



earlier examples, describes potential vision and imaging technology solutions. X-ray devices have been found to be ineffective in real-time applications where control of cutting devices with respect to deforming tissue interfaces is required (Border et al. 2019). Ultrasound transceivers have demonstrated effectiveness in detecting tissue interfaces at the line speeds required in pork processing, and work by Khodabandehloo (2016) published by the Australian Meat Processing Corporation (AMPC), further investigates the potential for ultrasonic-guided cutting automation to remove fat from striploin to specified levels of fat thickness over the workpiece. Border et al. (2019) conclude their review of sensing technologies to complement machine vision and perception with an example tactile sensing. A surgical process in which soft tissues undergo cutting by a drill, which is guided through specific regions of the tissue structure. This has been achieved through sensing and analysis of force feedback signals, identifying key signal characteristics and providing sensory information to the machine in order to ensure safe and effective outcomes from the process.

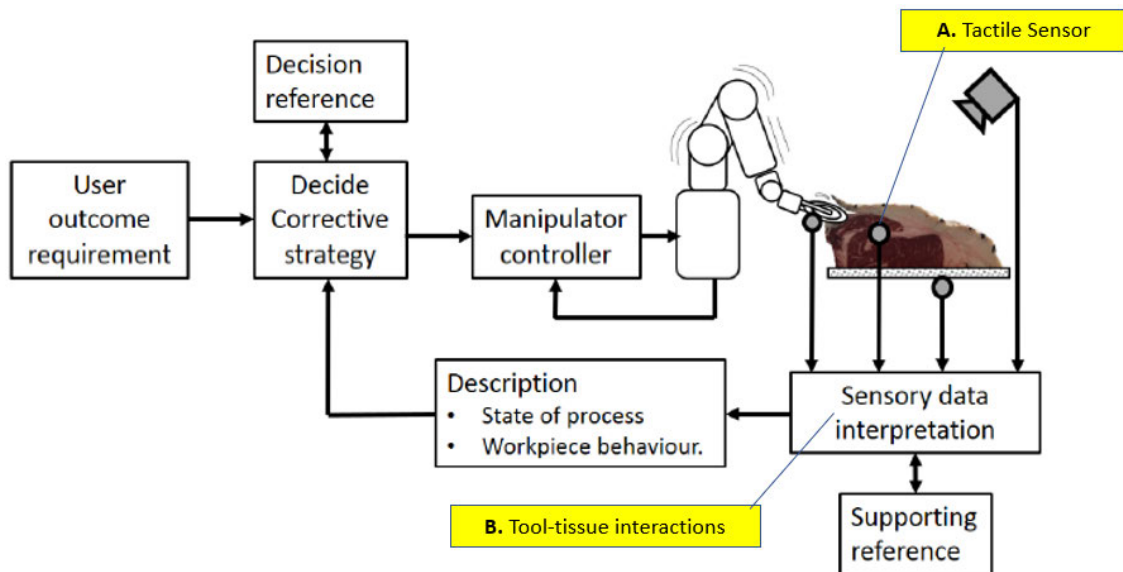


Figure 2.8: Robotic Beef Processing - Modified Schematic (Border et al. 2019)

Figure 2.8 represents a closed-loop robotic system designed by Border et al. (2019). Modifications to this schematic (in yellow) outline the potential for a tactile sensing integration to aid in the prediction of cutting trajectories to trim fat from beef striploin. Key functional blocks are defined, with a tactile sensor (A) providing real-time feedback from tool-tissue interactions at the workpiece. The sensor data (B) is interpreted along with other data, which is applied to models/references to determine control strategies. Predictions of future workpiece behaviour guide cutting paths to maintain product specifications

with an aim to increase product value-add.

Khodabandehloo (2016) reports on key specifications directly applicable to the design of a tactile sensing instrument (Project Objective 4):

1. Width of striploin up to 150-300mm. Height of 60-150mm from the upper surface of the striploin to the working surface. The product can vary in length and equipment should accommodate up to 300-700mm in length
2. A variation in fat thickness over the surface of the striploin potentially up to 75mm, down to 2mm minimum. The gradient of fat thickness variations up to 50mm height over 25mm distance in a single specimen
3. 4-12mm +/- 2mm fat thickness over the striploin surface is the target specification for the final product
4. Industry automation must be suitable for line speeds of one striploin workpiece in 15s. Point measurements are not going to be suitable and a scanning tactile sensor will be required.

***Trials using  
ATTEC 3D  
trimmer with  
ultrasonic  
sensor***

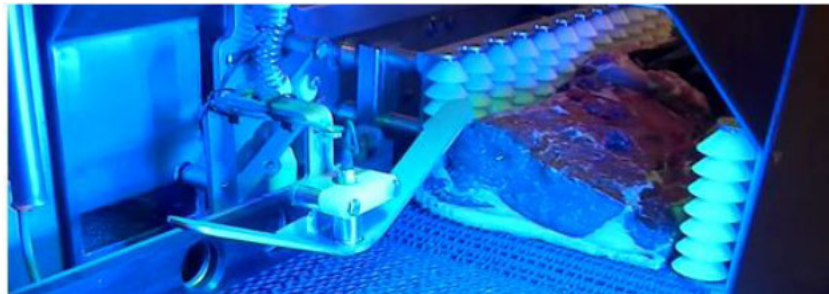


Figure 2.9: Ultrasonic Scanner used in Pork Processing Automation and in Beef Striploin Trimming Automation Trial (Khodabandehloo 2016)

The Australian beef industry has been shown to have low levels of automation in place, which is also evident in Figure 2.10 where Nason (2020) reports on the potential vulnerability of the mostly manual-labour industry during disruptions such as a global pandemic. The current imaging technology in sheep and pork processing plants are not expected to contribute effectively to automated beef processing for some time, and the efficiency gains in carcase cutting and boning will only be a start in improving the value-add for the red meat processing industry.

There are still many manual cutting and trimming operations to complete once a carcass has been cut into pieces, and for these, the meat worker must use their hands. There is clearly a place for new technologies to complement the automation of beef processing, and tactile sensing is a concept that fits the requirement for guiding automated tool-tissue interactions.

Tactile sensing is dependent on understanding the behaviour of a workpiece once tools and other manipulators are applying variable contact-forces to the medium. The review of research in the next section identifies some key characteristics of soft tissues including meat and fat (adipose), which are the two primary components of a beef striploin workpiece.



Figure 2.10: Australian Abattoirs - Still not Highly Automated in 2020 (Nason 2020)

## 2.2 Discriminating states and features of deforming tissues using tactile sensing

Soft tissues including muscle, adipose (fat), organs and synthetic materials have been manipulated and modelled in a wide range of research experiments. The aim of the work reviewed in this report has been to predict the behaviour of tissue structures under variable contact loads. Information is available from research into beef processing and the medical profession. Both sectors are actively investigating possibilities for increased automation and robotics, although understanding the interactions between tools and tissues is largely the focus of medical research into robotic-assisted surgery.

The available research involving tactile sensing and the beef industry is largely focussed on assessing the eating quality of beef, rather than structural features of tissues being deformed by contact loads. This research however, provides useful information to support anecdotal evidence provided by the USQ Centre for Agricultural Engineering (CAE), suggesting that beef striploin samples exhibit higher stiffness in the fat layer compared to the meat/muscle component of the workpiece. The reason for this may be influenced by the age of the samples at the time they are received by USQ and subsequently applied to experiments. The age of a beef striploin workpiece in an abattoir is likely to be lower than those received by USQ, and while an accurate estimate of age is not known at this time, the modelling applied in this project is sensitive to the elasticity of the fat and the viscoelastic properties of the meat. Both of these properties have been shown to vary with age.

The age of beef post-mortem affects the mechanical and electrical properties of natural soft tissues such as beef. Temporal variations in the chemical and structural composition of the medium affect the amount of influence the muscle fibres have on experimental sensor interactions (Zamora, Debiton, Lepetit, Lebert, Dransfield & Ouali 1996). Stiffness of beef samples increased significantly during the first 24 hours post-mortem (Figure 2.11a), followed by the deformation reaction-force reducing by half every 4 to 5 days of ageing. The contact force in these and other similar meat toughness experiments (Wang, Sun, Wang, Hu, Chen & He 2009) (Figure 2.12) was applied parallel to the muscle fibres. This emphasises the anisotropic reaction force characteristics of the meat, which exhibits higher resistance to deformation when the force is applied parallel compared to

perpendicular deformation. Derington, Brooks, Garmyn, Thompson, Wester & Miller (2011) report that muscle fibre angles change significantly across a beef striploin, which exhibits variations in toughness when tested in different regions of the sample. The authors also cite evidence suggesting that chilling influences the tension of muscle fibres and the resulting fibre directions. Temperature affects all measurements in some way, and the influence of temperature on sensors and workpieces in an abattoir would need to be considered when experimentation using tactile sensors and chilled beef is conducted at the USQ CAE laboratories.

Similar effects of ageing on the electrical properties of beef have been reported by Damez, Clerjon, Abouelkaram & Lepetit (2007) (Figure 2.11b) and Damez & Clerjon (2008). Anisotropic differences in capacitance and resistance reduce over similar time periods as observed in mechanical testing by Zamora et al. (1996). Electrical properties approach equal values when measured perpendicular or parallel to muscle fibres after approximately 14 days.

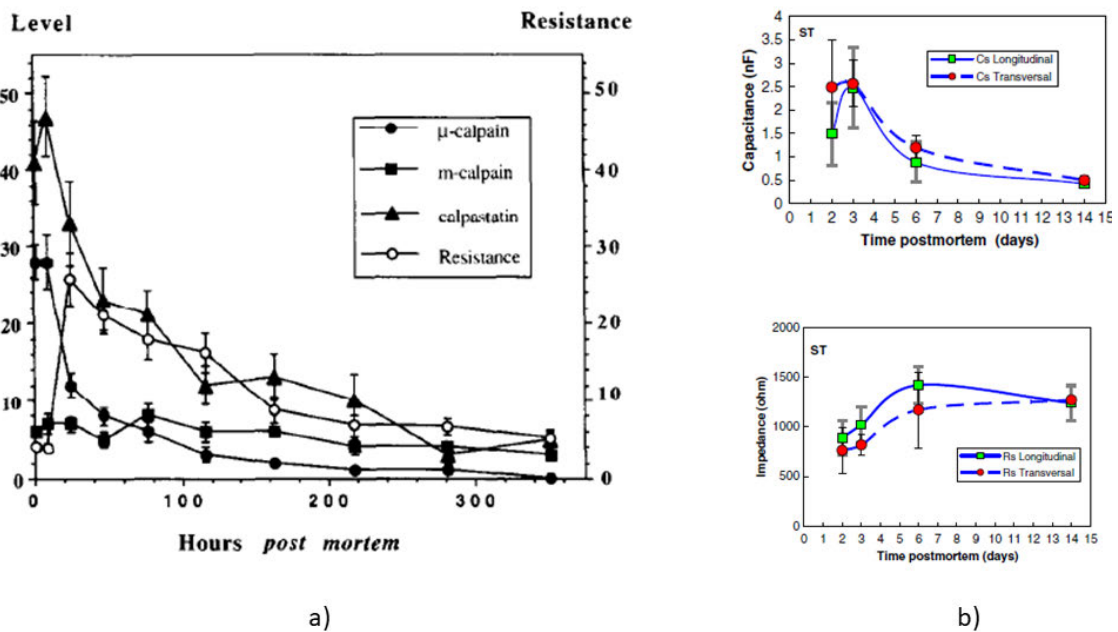


Figure 2.11: Beef Ageing and Isotropic Properties - Mechanical a) (Zamora et al. 1996) and Electrical b) (Damez et al. 2007)

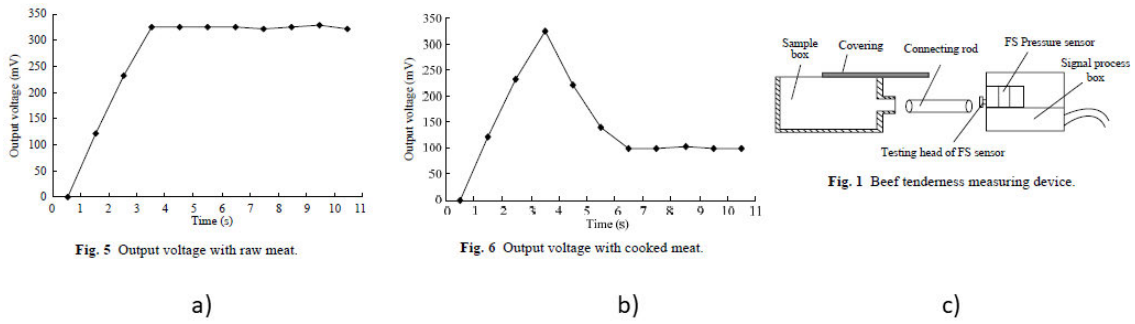


Figure 2.12: Deformation Forces for Beef with Parallel Force-Fibre Orientation(Wang et al. 2009)

The tactile sensing concept detailed in this report involves rolling contact between a wheel and the fat layer on the surface of the striploin, see Figure 2.13. There is a composite layer of compressed materials that combine to produce the reaction force under the wheel. The relevant properties of fat are detailed first, in research conducted to measure the compressive, tensile and shear modulus of adipose (fat) tissues found in porcine and bovine samples.

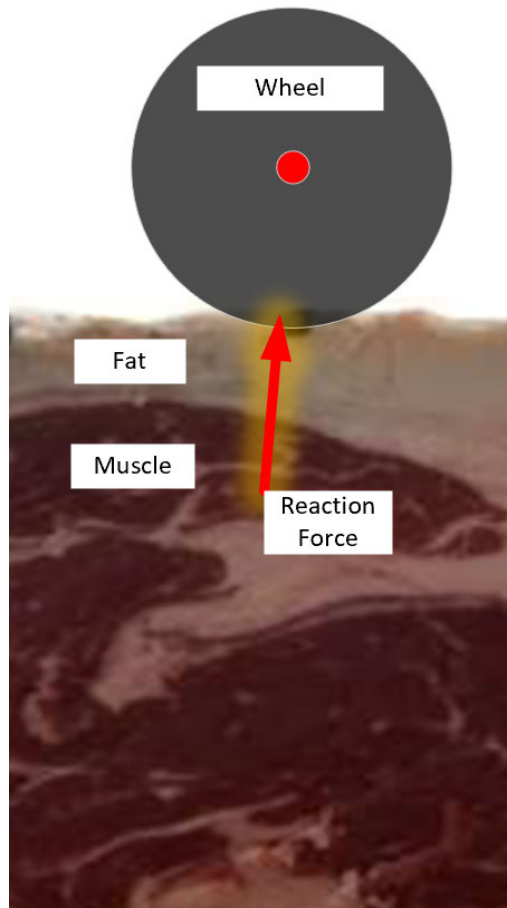


Figure 2.13: Wheel-Fat-Meat Composite Layer Compression

Research by Comley & Fleck (2012) into the mechanical properties of porcine adipose tissues provides insights into features including an isotropic structural membrane (Figure 2.14a) that effectively determines the stiffness of fat tissue under tension and compression. Fat tissue can be approximated as isotropic due to irregularity of microstructures within the specimens (Yoo et al. 2011), and (Comley & Fleck 2012) report further on the microstructure of fat tissue that can be modelled as an isotopic material. The stress-strain relationship (Figure 2.14b) is highly symmetrical during cyclical testing of tension and compression, which also highlights a condition at  $\approx 25\%$  deformation where fat tissue becomes highly rigid, opposing further compression or extension.

This evidence is useful in the development of a concept of operation for the tactile sensing instrument. The outer layer of fat can be considered relatively consistent in its structural form, which supports the decision to first model the form of the meat as an arched fat layer over muscle. The compressive features of the fat membrane are then assumed to deform relative to the applied force under the contact-area under the wheel. The maximum deformation point near the centre of the wheel may tend to 'lock-up' (Comley & Fleck 2012) after sufficient deformation, transferring the force to the muscle where viscoelastic characteristics could then influence the dynamic deflection outputs from the instrument.

The work of Yoo et al. (2011) involved the comparison of bovine fatty tissue (76% adipose) with connective tissue (2% adipose) from the orbital cavity. These experiments involved shear stress testing only, however the results indicate that lean bovine connective tissues display up to five times the shear strength of fatty tissues under the same loading conditions. The structural model of (Young & Budynas 2002) detailed later in this report, has provisions for shear modulus constants. The fat-layer model could be augmented with estimations of shear modulus, should future experimentation require adjustments to better characterise the properties of fat.



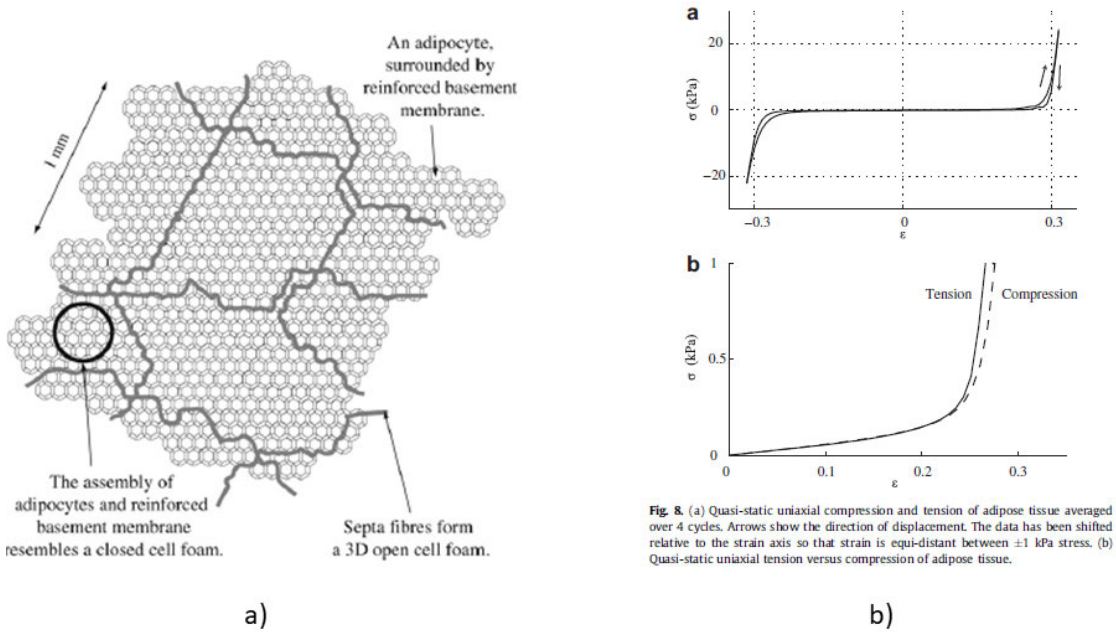


Fig. 8. (a) Quasi-static uniaxial compression and tension of adipose tissue averaged over 4 cycles. Arrows show the direction of displacement. The data has been shifted relative to the strain axis so that strain is equi-distant between  $\pm 1$  kPa stress. (b) Quasi-static uniaxial tension versus compression of adipose tissue.

Figure 2.14: Adipose Tissue Structure and Stress-Strain Relationship (Comley & Fleck 2012)

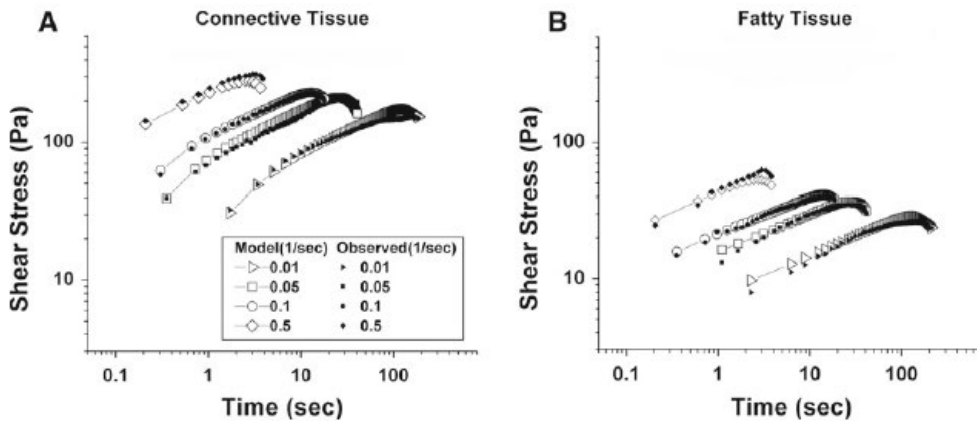


Fig. 9 Mean shear stress of 5 samples as a function of time for shear rates of 0.01, 0.15 0.10 and 0.50(1/s). Solid symbols represent experimental data, while open symbols represent model values. Shear stress increased with shear rate, and specimens failed faster at higher shear strain rates since all comparable specimens failed at similar strain. Error bars have been omitted for clarity. a Connective tissue. b Fatty tissue

Figure 2.15: Shear Stress-Strain Relationships of Adipose and Connective Tissues (Yoo et al. 2011)

The elastic modulus of fat tissue is essential in building the structural model (Young & Budynas 2002). Comley & Fleck (2012) have provided test results that show Young's Modulus for fat ranged from 1kPa to over 1MPa, increasing sharply with strain rates over  $100s^{-1}$  (Figure 2.16). The fat samples tested in these trials however, were only 3 hours post-slaughter. It is assumed that the fat layer of striploin samples display high levels of stiffness and elastic modulus. The upper range of elastic modulus therefore



(1MPa) is considered a reasonable starting point for establishing the modelling required for Project Objective 3. The rate of deformation is also important, and these parameters are discussed further in the modelling details.

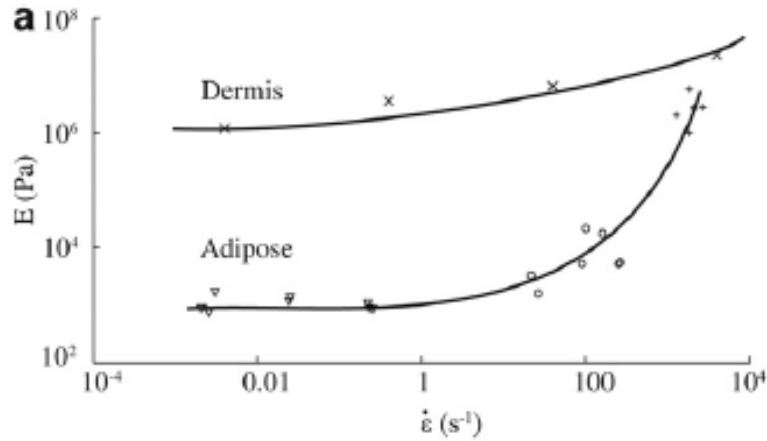


Figure 2.16: Variations in Young's Modulus for Changes in Strain Rate (Comley & Fleck 2012)

Moreira et al. (2012) experimented with force relaxation measurements and modelling using a sample of beef, deformed with a cylindrical indenter (Figure 2.17). The measurements were used to predict unknown coefficients across a range of viscoelastic models. The model most accurately representing the experimental results was used to design an active-observer control system. Force feedback and viscoelastic interaction modelling using classical spring-damper models controlled the tool-tissue interactions between a robotic manipulator and soft tissue. This work aimed to improve technological advances in robotic surgery by guiding the robot relative to contact force and tissue deformation in real time. The efficiency of computing a spring-damper dynamic force model is potentially more suitable for real-time implementation than complex finite element models (FEM) (Moreira, Zemiti, Liu & Poignet 2014). For example, rolling indentation testing conducted by Sangpradit et al. (2011) at 45mm/s across a 150mm test piece would take  $\cong 3.3s$ , where the simulation of the same test using FEM took 10 minutes. FEM also requires detailed knowledge of workpiece-specific mechanical properties, which may be difficult to generalise for significantly variable workpieces such as humans (Sangpradit et al. 2011) or beef striploins.

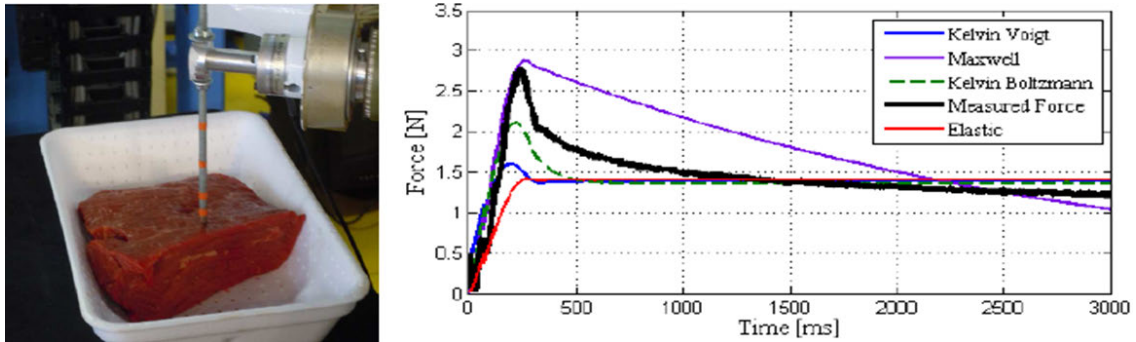


Figure 2.17: Beef Deformation with Cylindrical Indenter (Moreira et al. 2012)

Summarising the work of (Moreira et al. 2012):

1. Indenter is 6mm diameter with a flat end. The results are for an 10mm indentation.
2. Peak interaction force  $\cong 2.75N$  occurs  $\cong 250ms$ . For a 10mm displacement that suggests an average peak deformation stress  $\cong 97$  kPa, at a deformation rate of  $\cong 40mm/s$
3. The most accurate viscoelastic model compared to experimental results was the Kelvin-Boltzmann model. This is a modified Kelvin-Voigt model, incorporating an additional series spring element
4. The Kelvin-Voigt model had a realistic response and settled at the appropriate steady state after deformation. Error was most prevalent when modelling the dynamic deformation of the workpiece.

Sangpradit et al. (2011) conducted rolling indentation testing using a wheeled probe over both natural and synthetic viscoelastic test pieces. The rolling mode of indentation was preferable based on the medical context of the research, where surgeons operating robotics in minimally invasive surgery may need to scan a relatively large area of soft tissue. In this situation, a series of point measurements would not be feasible.

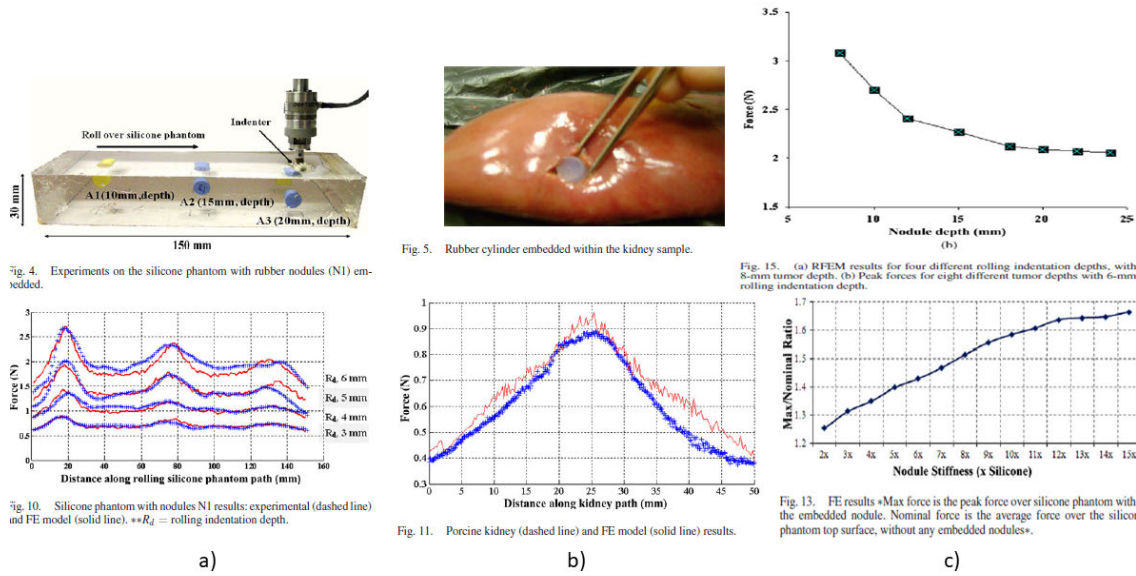


Figure 2.18: Rolling indenter Sensitivity to Depth of Tissue Structural Features (Sangpradit et al. 2011)

Observations from Sangpradit et al. (2011):

1. Indenter wheel size is 8mm diameter, rolled at 45mm/s, with the force sensing probe mounted perpendicular to the samples (a)
2. Local deformation forces could be used to detect a range of embedded nodules of higher stiffness relative to the silicone phantom (b), (c).
3. When the depth of nodules under the surface was more than 15mm, the ability to discriminate different stiffness nodules was significantly reduced, likewise when the deformation depth was less than 5-6mm.
4. The absolute values of forces measured was low, and the ratio between the wheel reaction force over a high-stiffness area compared to areas of low stiffness was less than 2 (low-level discrimination required).

The composition of beef and fat along a vertical sensing axis is expected to vary considerably over each workpiece, as shown in Figure 2.20 (Border et al. 2019). The macro-level features of this workpiece include the composition of beef and fat in different regions of the cross-section, as well as interfaces between the beef and fat that define the underlying geometric structure of the beef.



Figure 2.19: Beef Striploin Tissue Structures (Border et al. 2019)

The hidden features of striploin however, are lower stiffness lean muscle tissues relative to the surface fat layer. To discriminate changes in thickness of fat-over-meat, the instrument will need to be sensitive to the deformation characteristics of the meat underneath, which won't simply 'push-back' harder as the wheel passes over. With sufficient deformation depth to transfer contact force through the fat to the muscle, it is reasonable to expect that the instrument could respond to the muscle-fat interface profile if certain characteristics of the viscoelastic muscle tissue are incorporated into the design of the instrument and reference models used to interpret the response.

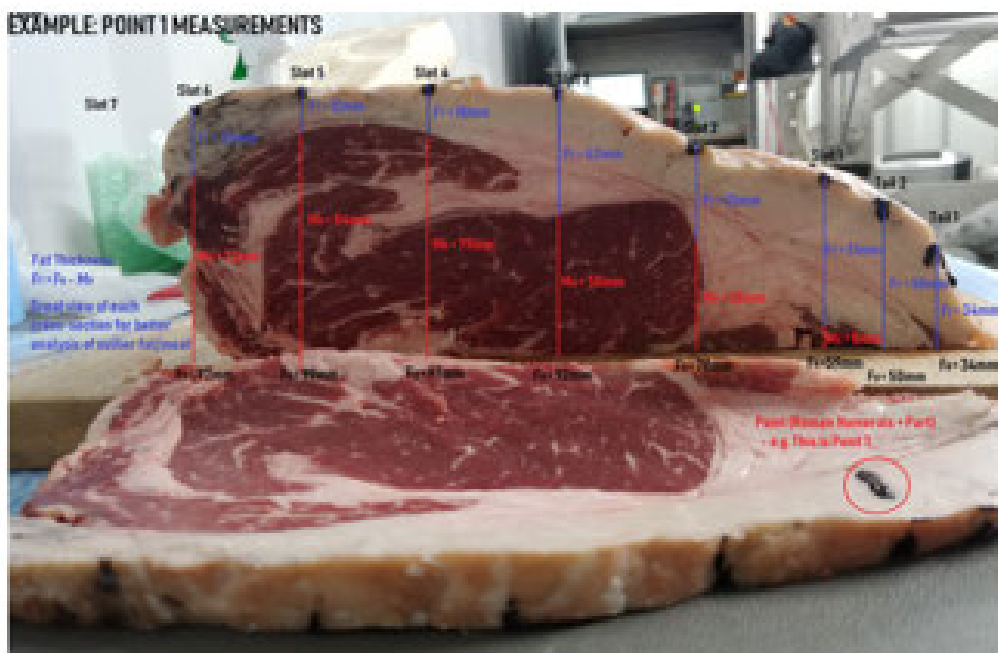


Figure 2.20: Beef Striploin Tissue Structures - Measurements (Border et al. 2019)

Moreira et al. (2012) applied a Kelvin-Boltzmann model to an active observer (AOB) control system, to maintain the magnitude of applied force from a robot-actuated indenter onto a viscoelastic beef workpiece. The choice of this model over a standard Kelvin-Voigt, Maxwell and elastic model was the closeness of the response to experimental results. All models approached a reasonably similar steady state force, representing the tissue stiffness, but the dynamic behaviour due to viscous damping characteristics varied across the models. Moreira et al. (2012) found that a spring constant ( $K$ ) of around 200-400 N/m for trim beef sample and around 15-50 for viscosity coefficients ( $B$ ). As the system was a dynamic control system, the Kelvin-Boltzmann model was considered a suitable choice and the AOB system was shown to be stable and robust.

Roberts (1994) reviews the Voigt, Maxwell and standard linear solid models of viscoelastic materials. The standard linear solid model is recommended as a more reasonable approach to modelling viscoelastic materials due to the quantitative anomalies in the other two approaches. These include the complete relaxation of stress in the Maxwell model, after a sudden application of force to the material, and the infinite delta function force in the Voigt model relaxation.

The deformation model being investigated in Section 2.3.2 is a static model, which being applied in a quasi-steady state context with a series of contact points being considered over the surface. The static limitations of the deformation model suggest that a simple Kelvin-Voigt viscoelastic model is suitable for preliminary work. Complex, high-order spring-damper arrangements with the standard linear solid model (Roberts 1994) for example, may be required if future experimental work characterising the instrument-workpiece dynamics is limited by the two-element viscoelastic model.

## 2.3 Modelling the rolling tactile sensor and beef workpiece

The instrument design from product baseline through to predictions of performance, is based on modelling:

1. Geometry of the workpiece, instrument kinematics and the physical constraints of the USQ CAE test rig

2. Wheel reaction force profiles as the wheel is positioned over the arched workpiece
3. Deformation of the surface layer, a representative arch of high-stiffness, isotropic fat tissue
4. Contact area under the wheel, including when fully dynamic scanning of the instrument is considered in terms of preliminary results produced by quasi-steady static deformation modelling.

### 2.3.1 Geometric Model of the Workspace

The tactile sensor design includes a mechanical interface with a test rig, purpose built for the USQ CAE research into beef processing automation (Cooney 2020). The test rig, shown in Figure 2.21 has both fixed and variable geometry components moving on 3 linear Cartesian axes to position devices over a beef striploin:

1. work surface (1)  $800mm \times 370mm$
2. gantry (2) located at  $257mm$  elevation from the work surface (1) The gantry is fitted with a linear actuator to position the tool attachment interface (3) in the y axis
3. moving tool attachment interface (3) with a flange in the x plane for attachment of the tactile sensor at variable elevation in the z axis above the work surface. The flange is expected to provide an interface at  $\cong 170mm$  to  $300mm$  z axis elevation above the work surface

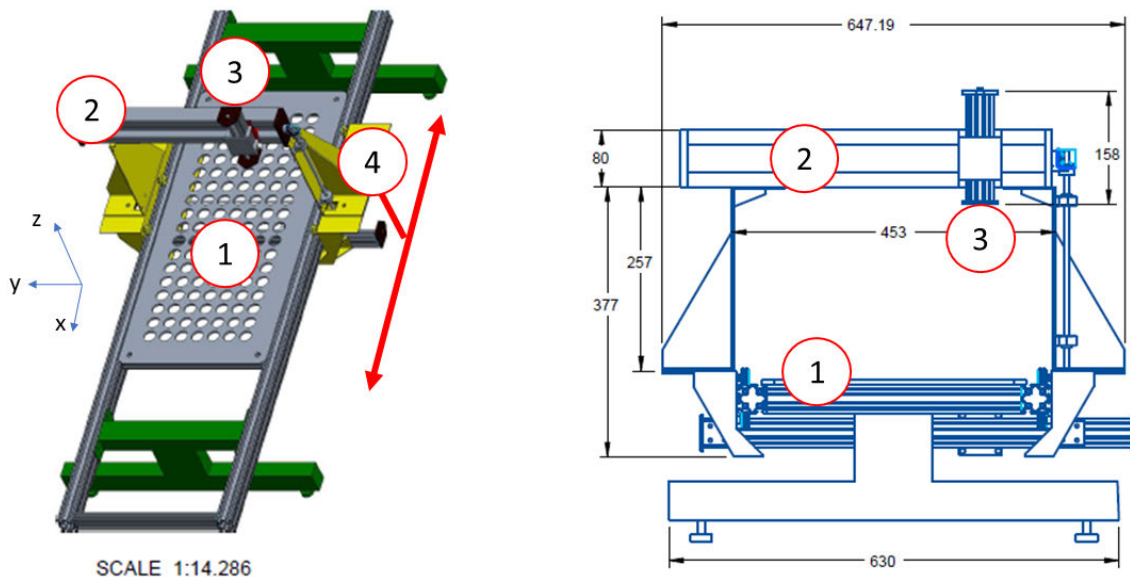


Figure 2.21: Test Rig Design Drawing(Cooney 2020)

The tactile sensor design for striploin tissue discrimination is required to scan samples with expected variations in elevation of up to  $150\text{mm}$  over a scan length of  $200$  to  $300\text{mm}$ , with gradients in some sections of over  $60^\circ$ . (Khodabandehloo 2016). Figure 2.22 is another example of a beef striploin primal cut, emphasising the variations in geometry and composition which complicates the implementation of automation for cutting and trimming processes (Khodabandehloo 2016).

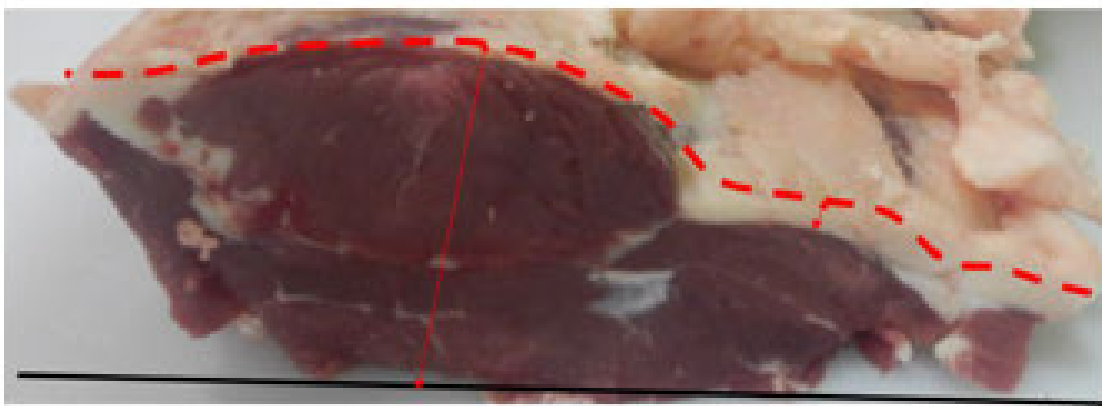


Figure 19: Primal piece height variability poses complications for automation over and above the fat thickness variation with primal orientation as shown.

Figure 2.22: Variations in Beef Striploin Surface and Composition (Khodabandehloo 2016)

Figure 2.23 shows a basic diagram outlining the concept for the hardware configuration.

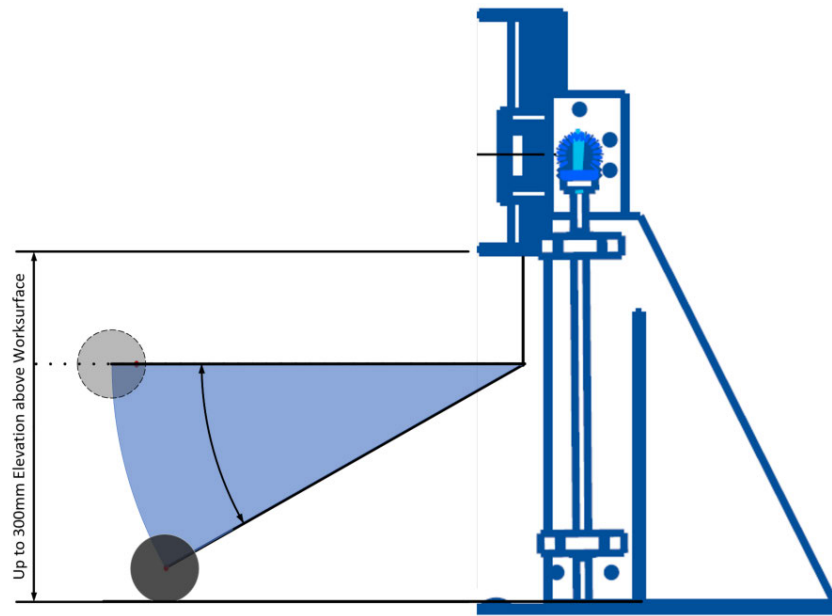


Figure 2.23: Rolling Tactile Sensor Concept Including Test Rig (Cooney 2020) Interface

The geometric model of the beef workpiece is critical to the application of a force model, as described further in Section 2.3.2. Approximating the workpiece as a series of arches helps with refining a problem statement; the model examines the roller interacting with the representative structure placed on a horizontal surface. The roller is confronted with the leading edge of the meat and rides up over this feature, refer to Figure 2.24.

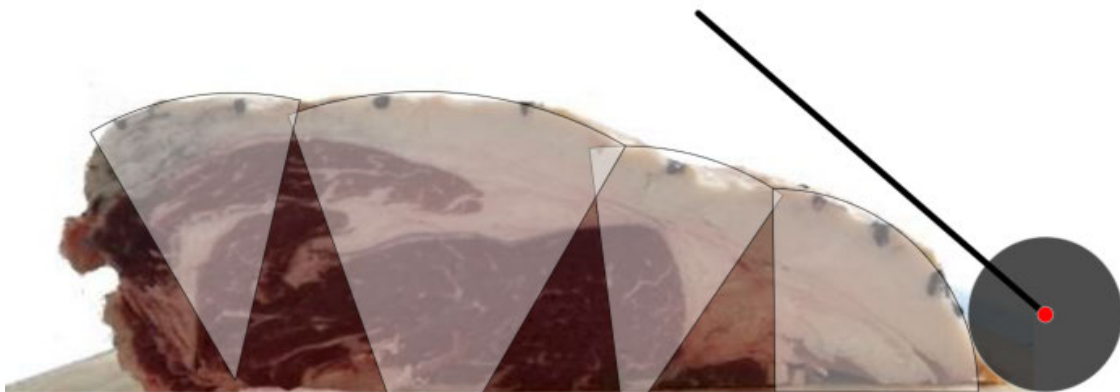


Figure 2.24: Circular Arch Surface Approximations for Force Modelling using the methods of Young & Budynas (2002)

The geometric modelling concept is further enhanced in Figure 2.25. The meat and roller interaction has been defined in more specific terms, representative of the stress and strain analysis methods developed by Young & Budynas (2002) for curved beams and arch geometries:



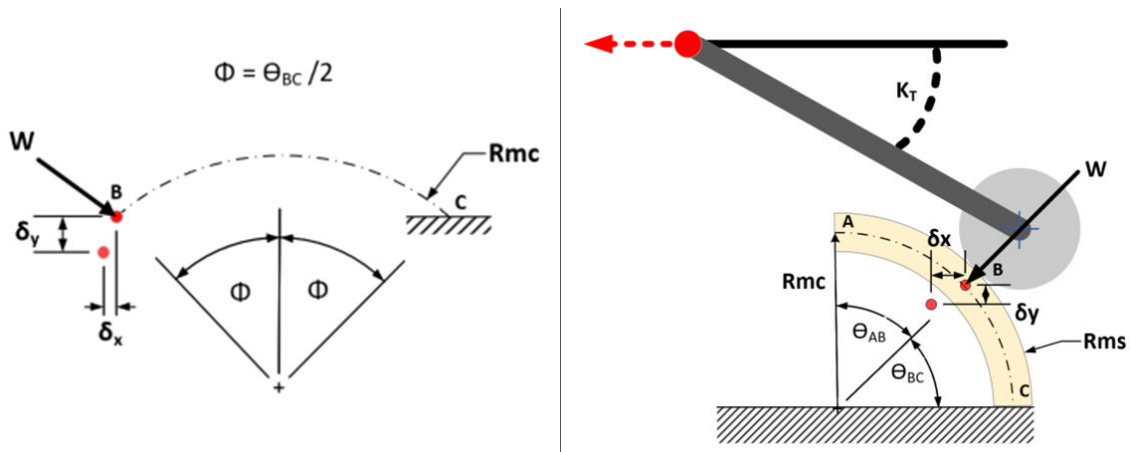


Figure 2.25: Roller-Arch Geometry and Interaction Model

1. Meat surface fat layer arch, radius  $Rms$  with a cross-section centroid curve  $Rmc$  representing the effective mid plane of a uniform thickness arch of homogenous fat tissue
2. The point  $B$  in Figure 2.25 at which the concentrated radial force  $W$  is applied, can be determined by tracking the position of the wheel axle within the x-y axes of the workspace and designating a datum point for the arch structure. Deformation at the arch centroid is shown as a red dot that transitions in the x and y axes by  $\delta x$  and  $\delta y$  respectively.

The application of Roark's formulas in analysis of a deforming arch under concentrated radial loading is outlined below, based on guidance provided by Young & Budynas (2002) and the geometry of the modelled workspace outlined earlier:

1. Material properties and the uniformity of the arch structure are based on approximations and assumptions. Engineering materials such as steel, concrete and wood are typically the subject of analysis in these formulas, and the introduction of a viscoelastic fat tissue structure will require careful considerations for material properties and the validity of results
2. Precision in calculations should be carried through the calculations, however no more than three significant figure precision should be expected in results
3. Checking results is critical, whether by judgement and common sense or through established principles such as superposition and reciprocal deflections (Young &

Budynas 2002).

4. Boundary conditions may introduce uncertainty, particularly in the case of a beef tissue sample, where the fixed end of the structure is not truly fixed to the work surface for example
5. Localised effects of stress and strain are not accounted for in the formulas
6. Young's modulus ( $E$ ) is an important component of Roark's equations. Comley & Fleck (2012) reported results and discussed related research approximating the elastic modulus of different varieties of adipose tissues. Results suggest approximately 1 - 5 kPa at low to medium strain rates, with variations up to  $\approx 1\text{MPa}$  at high strain rates ( $3000s^{-1}$ )

The most appropriate model is chosen from the tables in Chapter 9 of (Young & Budynas 2002):

- Table 9.3, "Reaction and deformation formulas for circular arches" (Young & Budynas 2002, p.333). Specifically, case 5c. for a concentrated radial load  $W$ :


<p>5c. Concentrated radial load</p> 	$LF_H = W \left[ \frac{k_1}{2} (\theta n + \phi n - scn - s^2 m) + k_2 (m - c) \right]$ $LF_V = W \left[ \frac{k_1}{2} (\theta m + \phi m + scm + c^2 n) + k_2 (s + n - 2scm - 2c^2 n) \right]$ $LF_M = W [k_2 (1 + sn - cm)]$
---	--

Figure 2.26: Roark's Formulas and Model for a Concentrated Radial Load on a Circular Arch (Young & Budynas 2002, p.341)

### 2.3.2 Surface Force Modelling

The free body diagram (FBD) (Figure 2.27) enables analysis of external forces associated with the tactile sensing mechanism, test rig and beef striploin sample under test:

1.  $F_{DB}$  is the spring force acting at angle  $\Theta_2$  to the trailing arm
2.  $F_x$  is the reaction force at the test rig support
3.  $F_m$  is the resolved weight vector for the instrument assembly
4.  $F_C$  is the reaction force acting tangentially to the arch surface under the wheel
5. The forces acting on the trailing arm and wheel will be relative to the angle  $\Theta_1, \Theta_2$  &  $\Theta_3$ .

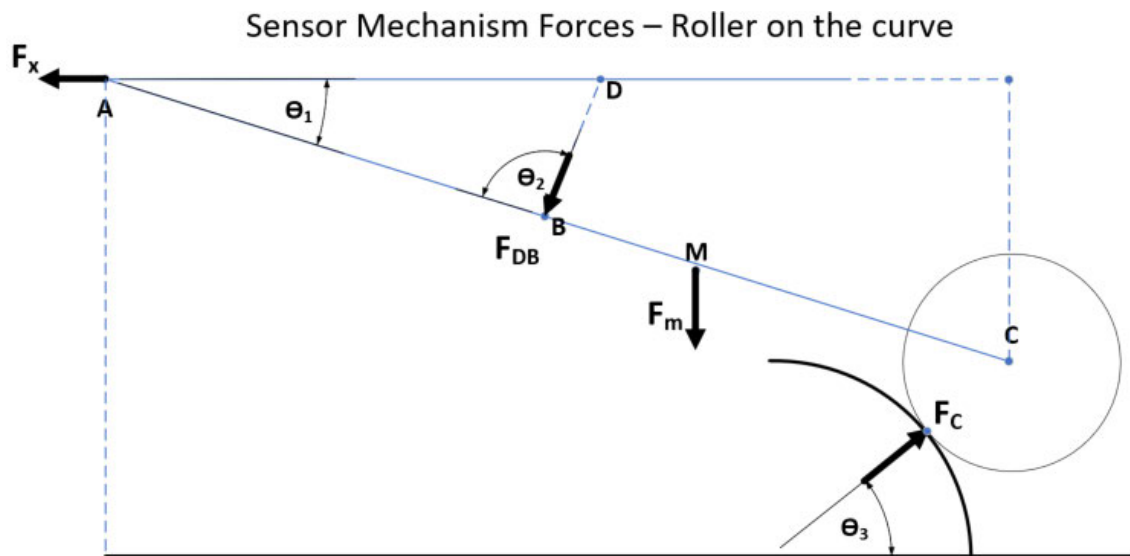


Figure 2.27: Free Body Diagram (FBD) Example - Wheel over Arch

### 2.3.3 Modelling the Wheel-Tissue Interactions

The dynamic performance of wheels being towed over deforming surfaces has been modelled by Wong & Reece (1967), where predictions of towing force in terms of soil properties and wheel dimensions is possible with through analysis of radial and tangential stresses at the soil-wheel interface. Rentschler, Dumpert, Platt, Lagnemma, Oleynikov & Farritor (2006) adapted the work of Wong & Reece (1967) to investigate wheel-tissue interactions between wheeled robots and liver-tissue during research into minimally invasive robotic

surgery techniques. Key aspects of this work are the wheel-tissue interaction models and experiments that incorporate the viscoelastic properties of soft tissue and the effects that these properties have on the dynamic interactions with a wheel moving over the surface.

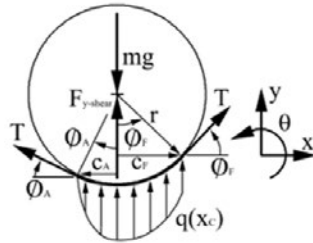


Fig. 8. Vertical forces acting on the wheel for the viscoelastic model. The pressure due to tissue deformation is shown, in addition to the vertical component of shear force, membrane tension, and robot weight.

a)

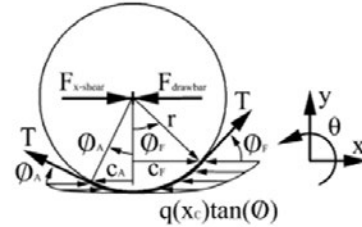


Fig. 9. Horizontal forces acting on the wheel for the viscoelastic model. The pressure due to tissue deformation is shown, in addition to the drawbar force: horizontal component of shear force, and membrane tension.

b)

Figure 2.28: Wheel-Tissue Interaction Models (Rentschler et al. 2006)

Figure 2.28 shows the pressure applied under the wheel due to deformation of the tissue, as well as tension forces applied at the surface of the deformed tissue. Rentschler et al. (2006) note the asymmetrical nature of the contact surface below the wheel, where the leading sector of the wheel  $\phi_F$  contacts a greater area of tissue surface than the trailing sector  $\phi_A$ . This observation supports their decision not to apply a purely elastic (symmetrical) tissue interaction model. The surface membrane is also reported to be a significant component of the reaction force under the wheel. Experimental testing of surface characteristics is required however, to determine the contribution of surface tension to reaction force under the wheel. Therefore, this component is not included in the preliminary design of the tactile sensing instrument.

The analysis and modelling of forces under the roller requires careful consideration of the time-varying nature of the behaviour of viscoelastic tissues under rolling indentation. The literature has indicated that a gradient of reaction forces can be expected, along a contact surface that extends further towards the forward sector of the roller. A piecewise approach may be appropriate, as applied by (Davis, Sackey, Andrews & Owusu-Ofori 2017) in their investigation of rolling friction gradients under a metal-forming roller assembly (Figure 2.29). The force modelling concept for the tactile sensor is limited to quasi-steady state modelling (Young & Budynas 2002), therefore the contribution towards overall reaction force from a number of segments under the roller at defined time-steps is appropriate, rather than the continuous functions applied in dynamic modelling by Rentschler et al. (2006).

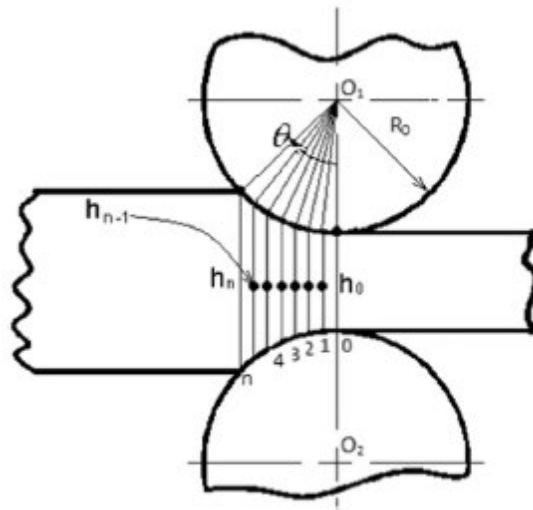


Fig. 2. Modified modeling technique showing "n" steps.

Figure 2.29: Piecewise Roller Deformation Analysis (Davis et al. 2017)

# Chapter 3

## Sensor Design

### 3.1 Operational Concept

#### 3.1.1 Document Overview

The design documentation introduces system-level concepts in terms of the purpose, architecture and intended use of the system. The design package is structured to support the manufacture of a prototype instrument, integration with a USQ-provided test rig and continuing experimental calibration and performance verification of the system.

Supporting documents are provided in Appendix B. The MATLAB code used in modelling is available in Appendix C.

This design package has been prepared with consideration for the guidance outlined in formal technical writing standards for Operational Concept Descriptions (OCD) (U.S Government 2000).

### 3.1.2 System Overview

This tactile sensing instrument is an open system, intended for use in experimental settings to investigate the tool-tissue interactions between the instrument wheel and a beef striploin workpiece. Figure 3.1 represents graphically, the system operating concept.

The instrument is designed to traverse a beef striploin workpiece (1), maintaining rolling contact (2) between a wheel (3) and the fat-tissue surface of the workpiece, with prescribed levels of wheel reaction force (4) generated by the trailing arm-spring mechanism (5). The workpiece is positioned on the USQ-provided test rig with the fat tissue exposed on the upper surface of the workpiece. The test rig interface (6) provides an instrument attachment point and the towing force required for user-controlled rolling contact over the workpiece.

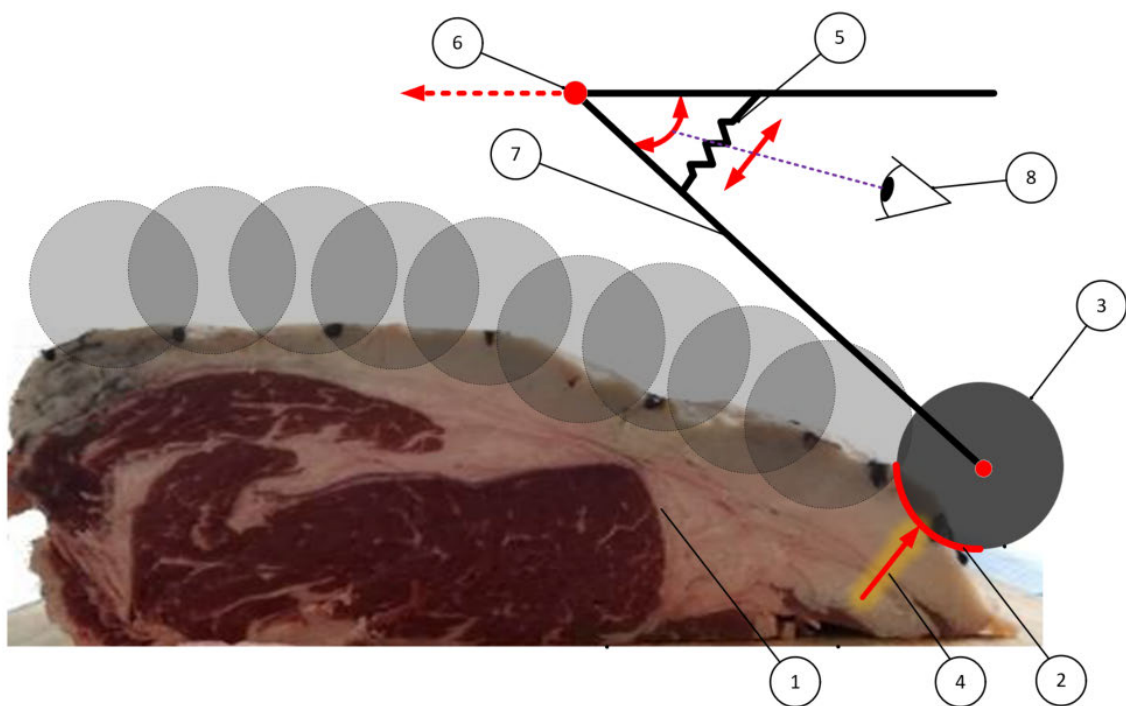


Figure 3.1: Operational Concept Diagram - Tactile Sensing Instrument & Beef Striploin

The tool-tissue interactions result in deflections of the trailing arm (7) around the pivot point (6). This mechanical energy in the form of angular or linear displacement of the trailing arm relative to the fixed instrument support, is detectable by a transducer (8) that converts this energy to an electrical form for processing.

The tactile sensing instrument is designed to complement the current and emerging research capabilities of the USQ Centre for Agricultural Engineering (CAE); particularly for researchers involved in the application of robotics and advanced process control in tasks such as beef cutting and trimming.

### 3.1.3 Limitations

1. The University of Southern Queensland (USQ) policies related to COVID-19 restrictions, result in limitations for the following activities in this engineering research project:
  - Manufacturing prototype hardware
  - Access to USQ laboratories
  - Access to the test rig required to mount the system and support the beef striploin workpieces
  - Integrating the mechanical, electrical and software subsystem components
  - Face-to face communication between student and supervisor
2. The system is designed for use with beef striploin workpieces within the range of geometric and compositional variations described by Khodabandehloo (2016). Specifically:
  - Width of striploin up to 150-300mm. Height of 60-150mm from the upper surface of the striploin to the working surface.
  - A variation in fat thickness over the surface of the striploin potentially up to 75mm, down to 2mm minimum. The gradient of fat thickness variations up to 50mm height over 25mm distance in a single specimen
  - 4-12mm +/- 2mm fat thickness over the striploin surface is the target specification for the final product.
3. The USQ-provided test rig is limited to beef striploin dimensions relative to the physical dimensions and clearance available within this equipment. This imposes further constraints on the dimensions recommended above and these constraints are subject to change during the ongoing design of the test rig (Cooney 2020) and are considered to be beyond the scope of this instrument design.



4. Modelling the behaviour of a highly variable, deforming medium such as meat is unlikely to produce modelled-system performance information that truly represents the behaviour of the prototype instrument interacting with a particular beef workpiece under any operating condition. Therefore, in the limited time available to design the instrument, the deforming medium characteristics considered within the scope of this report are also limited to:

- Static load deformations at equilibrium
- Quasi-static approximations of deformations occurring due to localised interactions between the applied load and a workpiece modelled as a viscoelastic deforming medium
- Viscoelastic modelling is limited to the Kelvin-Voigt spring-damper model

### 3.1.4 Assumptions

1. Material properties of hardware items:
  - Material for manufacture may include acrylic, polystyrene, nylon and/or carbon fibre
  - Density approximation in calculations/modelling =  $\rho_{design} = 1800kg/m^3$
2. Effects of bending and friction within the instrument mechanism are considered to be negligible during prototype design
3. Roark's formulas for stress and strain (Young & Budynas 2002):
  - (a) Material is isotropic, elastic and homogeneous
  - (b) Strain is proportional to stress
  - (c) Uniform arch cross section and symmetry about plane of curvature
4. Workpiece modulus of elasticity  $E$  can be estimated
5. The temperature of the workpiece and environment are controllable
6. The elasticity/stiffness and viscous damping characteristics can be approximated

### 3.1.5 Functional Requirements

1. Instrument design shall be compatible with striploin geometry variability:
  - (a) Width 150-300mm
  - (b) Height 60-150mm
  - (c) Fat layer variability from 75mm down to 2mm minimum. The gradient of fat thickness variations up to 50mm height over 25mm distance in a single specimen
  - (d) Industry target for uniform fat thickness of 4-12mm +/- 2mm over the striploin surface
2. The instrument response shall be compatible with line speeds of one striploin work-piece scan in 15s
3. The instrument shall mount to the USQ CAE test rig tool attachment fixture, at an elevation of 170 - 300mm above the work surface
4. The test rig shall provide up to 20N towing force to the instrument at rolling wheel velocities up to 30mm/s

### 3.1.6 Design Requirements

1. The prototype product baseline shall be derived from a minimum set of user-defined parameters:
  - (a) wheel radius  $R_w$
  - (b) wheel bore  $B_w$
  - (c) wheel hub width  $H_w$
  - (d) meat surface arch radius  $R_{ms}$
  - (e) tool-support elevation  $AZ$ .
2. The modelled workpiece shall be defined by preliminary mechanical parameters:
  - (a) The workpiece shall be modelled by an arched fat layer of variable thickness
  - (b) Fat layer elasticity  $E = 15\text{MPa}$
  - (c) Beef spring constant  $K = 200\text{ N/m}$

- (d) Beef damping constant  $B = 20 \text{ N.s/m}$
3. The spring constant of the instrument shall be matched to the workpiece spring constant determined through experimental calibration
  4. The wheel radius shall not exceed the representative modelled workpiece arch radius
  5. The derived trailing arm dimensions shall prevent contact between the instrument and workpiece at any point other than the wheel-tissue contact area, including initial contact and deformed surface scanning contact in Active Mode
  6. The instrument springs shall be commercial off the shelf (COTS) helical compression springs, with a mechanism that supports interchangeability of springs to vary spring constant during experimentation
  7. The transducer specification shall include  $\leq 0.1$  millimetre discrimination of linear displacements of plastic materials
  8. The transducer shall be compatible with a sampling rate of  $\geq 50 \text{ Hz}$

Functional and technical specifications shall be the focus of a review of results produced in the performance modelling phase. This review shall provide validation of parameter sizing in the preliminary design, and support conclusions to inform future work involving manufacture of and experimentation with a prototype instrument.

### 3.1.7 States and Modes

The system is described in terms of two modes, Initialisation and Sensing. Note that OFF is not a mode of operation nor system state, it is considered a pre/post condition of designated system modes. Modes are assumed to be user-selected via a user interface (UI).

Three logic-based system states, Preload, Sensing and Degraded are set by the system. The system states are described within each mode and individually, following the graphical representation in Figure 3.2:

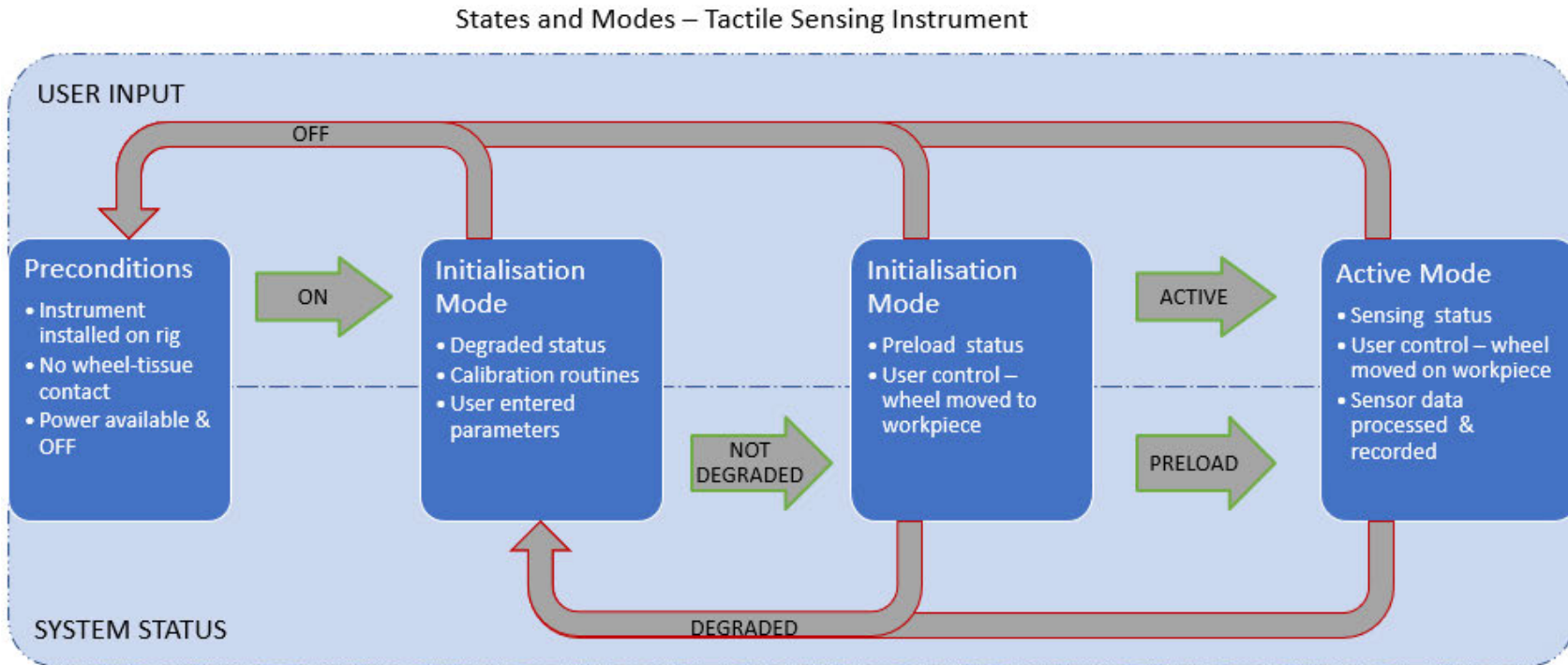


Figure 3.2: States and Modes - Tactile Sensing Instrument

## Initialisation Mode

### 1. Preconditions for Initialisation:

- Test rig tool attachment interface is positioned in elevation  $AZ$  above the work surface
- Instrument wheel is positioned on the work surface

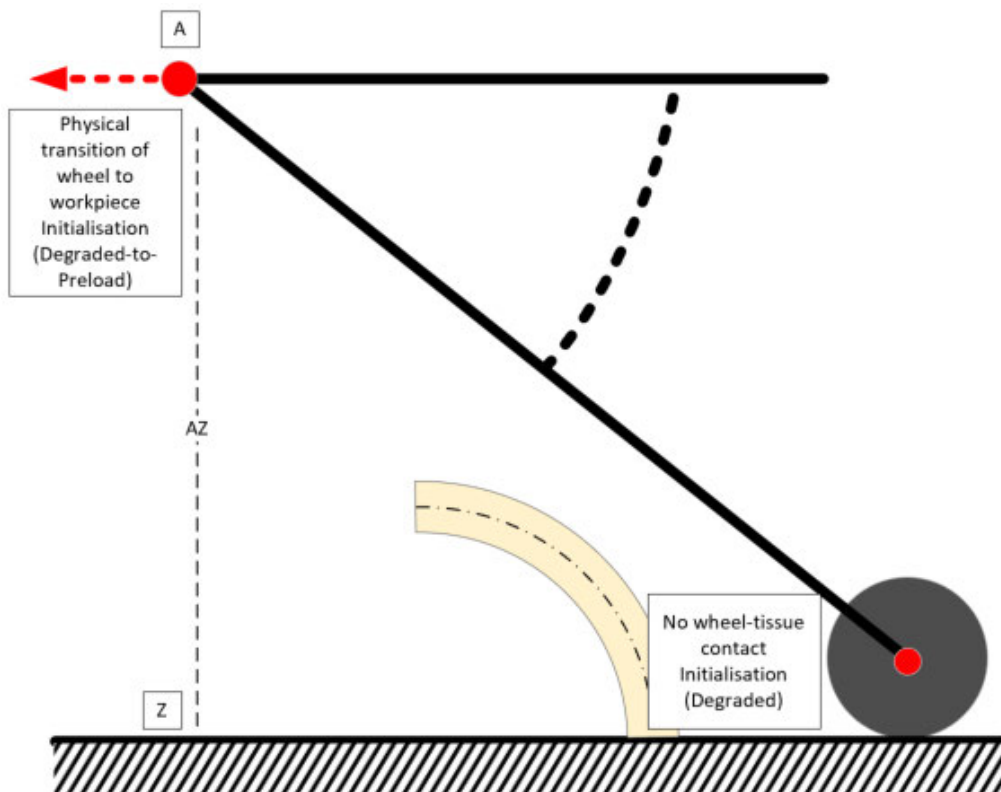


Figure 3.3: Initialisation Mode - Tactile Sensing Instrument

### Active Mode

1. The user selects Active mode once the instrument wheel has been placed on the workpiece and the system state is Preload

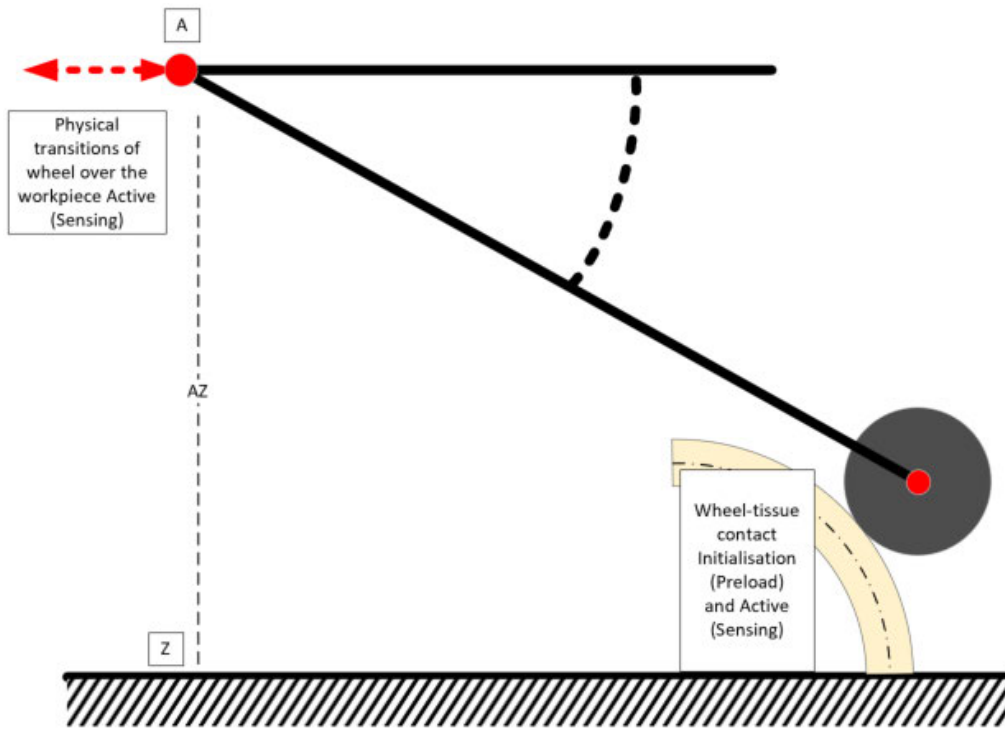


Figure 3.4: Active Mode - Tactile Sensing Instrument

2. System sensing data is processed and recorded

### 3.1.8 Operating Environment

The tactile sensing instrument shall be operated in a USQ CAE facility designed for temperature controlled operation of the test rig.

### 3.1.9 System and Subsystem Components

The tactile sensing instrument system comprises the following subsystem components:

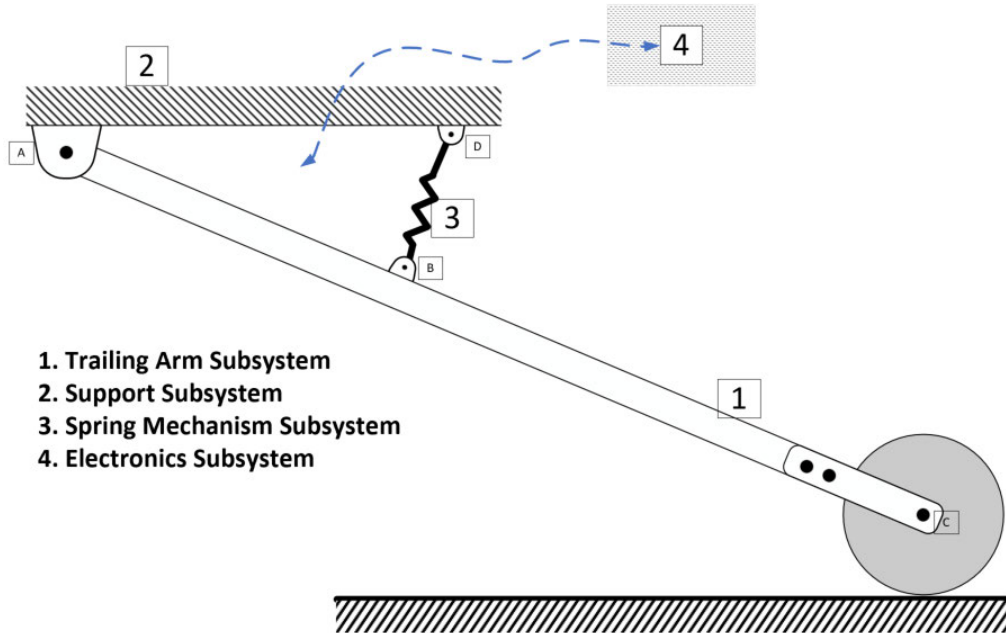


Figure 3.5: System-Subsystems Schematic Diagram - Tactile Sensing Instrument

The *Trailing Arm Subsystem* is a rigid mechanical linkage that connects the instrument wheel to the *Support Subsystem* and the test rig tool attachment interface. The *Spring Mechanism Subsystem* also attaches to the Support and Trailing Arm subsystems, providing a stiffness characteristic to the Trailing Arm hinging motion. A transducer will convert mechanical deflection of the Trailing Arm to electrical energy for processing in the *Electronics Subsystem*.

### Functional Block Diagram – Tactile Sensing Instrument

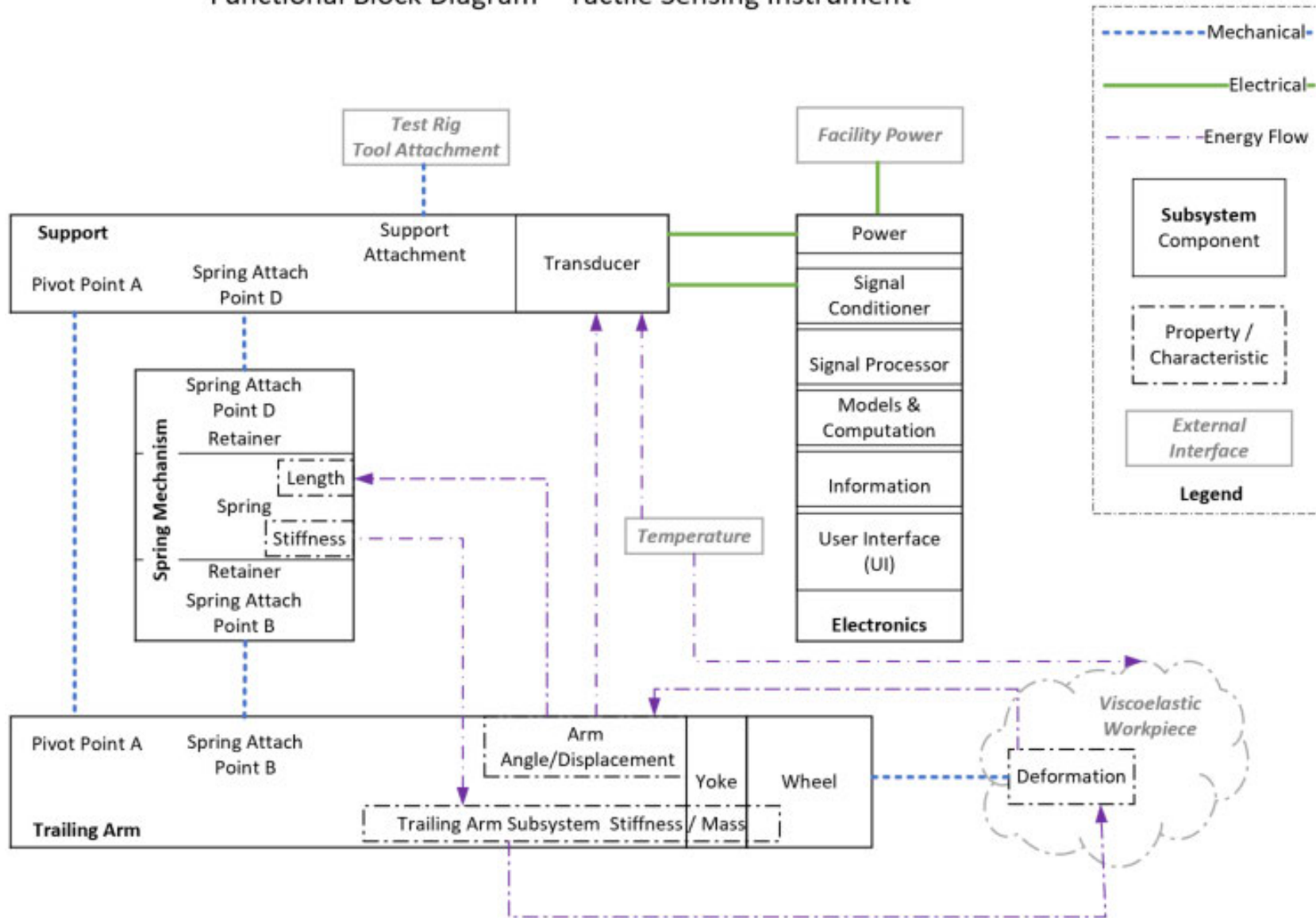


Figure 3.6: Functional Block Diagram - Tactile Sensing Instrument



The system is dependent on a number of external interfaces, as shown in Figure 3.6. Temperature of the workpiece and environment is included among these dependencies as this will have a significant effect on the workpiece physical characteristics and the energy flow through the entire instrumentation system. The temperature effects are shown relative to the workpiece and transducer, however the effect of temperature could reasonably be expected to influence many parts of the system both electronic and mechanical.

### 3.1.10 Safety/Risk Assessment

An assessment of hazards and risk for the project is provided in Appendix B. This document is reviewed and updated as hazards are identified through all phases of the project.

## 3.2 Mechanical Design

The detailed mechanical design is documented as follows:

1. Hardware architecture requirements and limitations for the instrument system/-subsystems and workpiece, based on test rig interface constraints and expected size variations for beef striploin workpieces . Equations are derived that relate the dimensions of the instrument/workpiece/rig for use in defining constraints and in system modelling; draft drawings for the system and subsystems including bill of materials with provisions for material properties and component mass in kg; interface management for the instrument-test rig
2. Applied force characteristics of the instrument over the system operating range
3. Predict the static deformation of a workpiece sample due to applied forces from the instrument
4. Develop a system model combining predictions for static instrument forces with a quasi-static viscoelastic model for soft-tissues
5. Prototype instrument bill of materials and component drawings

### 3.2.1 Hardware Architecture

#### Instrument/Workpiece Architecture

The hardware architecture design comprises all instrument and workpiece components in the workspace and the geometric reference points within the workspace itself:

1. Trailing Arm subsystem
  - Trailing arm
  - Yoke
  - Wheel
  - Attaching hardware
2. Spring Mechanism subsystem
  - Spring
  - Retainers
  - Attaching hardware
3. Support subsystem
  - Support
  - Transducer
  - Attaching hardware
4. Representative model of the beef striploin workpiece

#### Workspace Architecture

The view in Figure 3.7 is aligned with regular Cartesian coordinates and provides two quasi-static representations of the instrument, one with the wheel on the test rig work surface (x-axis) and another with the wheel on the upper/outer limit of the x-y plane for the workpiece representative geometry. An x-axis datum point  $X$  has been established, which enables modelled-wheel axle coordinate  $C_{x,y}$  tracking, relative to the workpiece. The arch geometry workpiece characteristic dimension is meat-surface radius  $Rms$ .

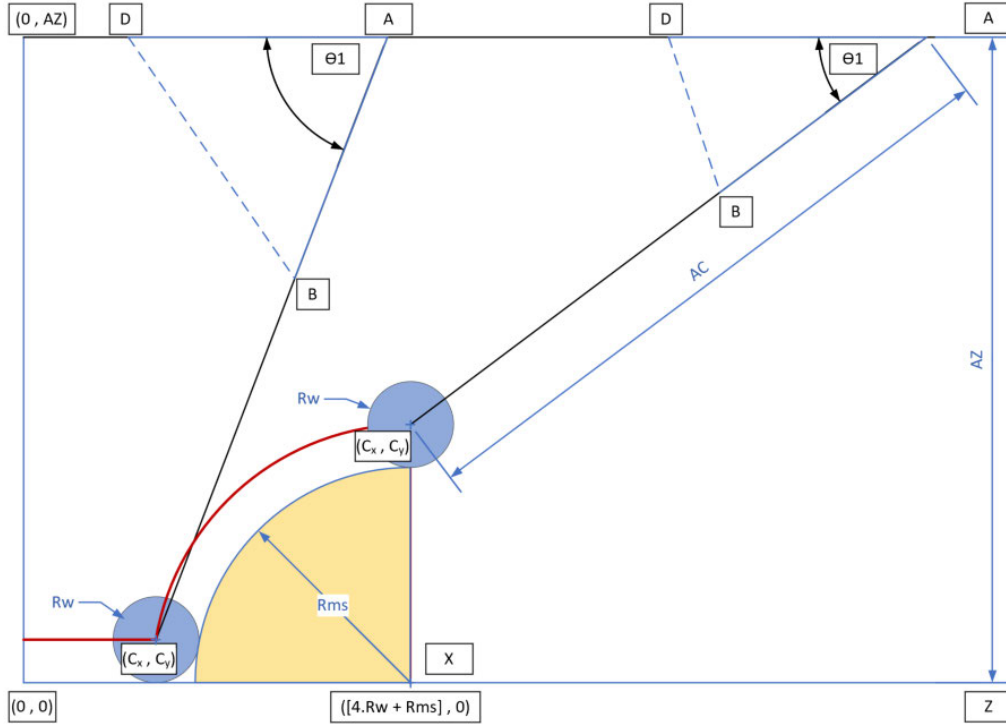


Figure 3.7: Workspace Reference Plane (x-y) Including Instrument, Workpiece and Test Rig Work Surface

The trailing arm assembly length  $AC$  is important in determining the potential 'measurement' angle  $\Theta_1$ . The modelled instrument tracks the wheel axle  $C$  coordinate  $C_{x,y}$  to determine angle  $\Theta_1$  and to resolve forces acting under the rigid, no-loss wheel.

The  $C_x$  coordinate is the x-axis of the model space. The  $C_y$  coordinate varies depending on the choice of wheel and arch dimensions:

$$C_y = \begin{cases} Rw, & \text{if } C_x < [X - \sqrt{(Rms + Rw)^2 - Rw^2}] \\ \sqrt{(Rms + Rw)^2 - (X - C_x)^2} & \text{if } [X - \sqrt{(Rms + Rw)^2 - Rw^2}] \leq C_x \leq X \end{cases} \quad (3.1)$$

### Trailing Arm Subsystem

**Simplifying Assumptions** The Trailing Arm subsystem design in this section follows a custom manufacture approach to producing these components. A number of available options for wheels and lightweight, rigid tubes and rods have been considered in deriving simplifying assumptions, with an aim of establishing a realistic product baseline for the instrument, within project time constraints.

Material properties are important in predicting the weight of the subsystem and also the stiffness achievable in the trailing arm component. Trailing Arm, Wheel and Spring Mechanism component mass (in kg) is based on a material thickness (in m) and density (in  $\frac{kg}{m^3}$ ) of:

$$\rho_{design} = 1800kg/m^3 \quad (3.2)$$

$$t_{material} = 0.003m \quad (3.3)$$

The Tactile Sensing Instrument system shall apply EN-1993 standards for hole spacing and edge distances as defined in Steelwork, ECCS - European Convention for Constructional (2017).

- Dimensions relative to the direction of applied force, outlined in Figure 3.8 shall be defined as:

- Edge distance:  $e_1$  and  $e_2$

$$e_1 = e_2 = 1.2Bw \quad (3.4)$$

- Hole spacing:  $p_2$

$$p_2 = 2.4Bw \quad (3.5)$$

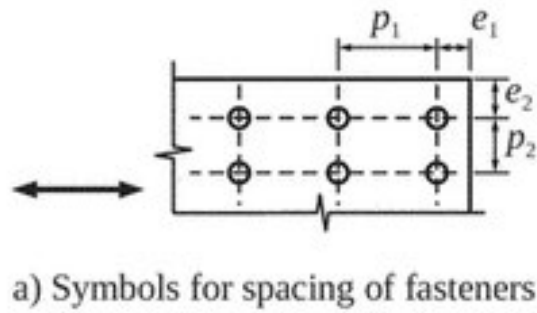
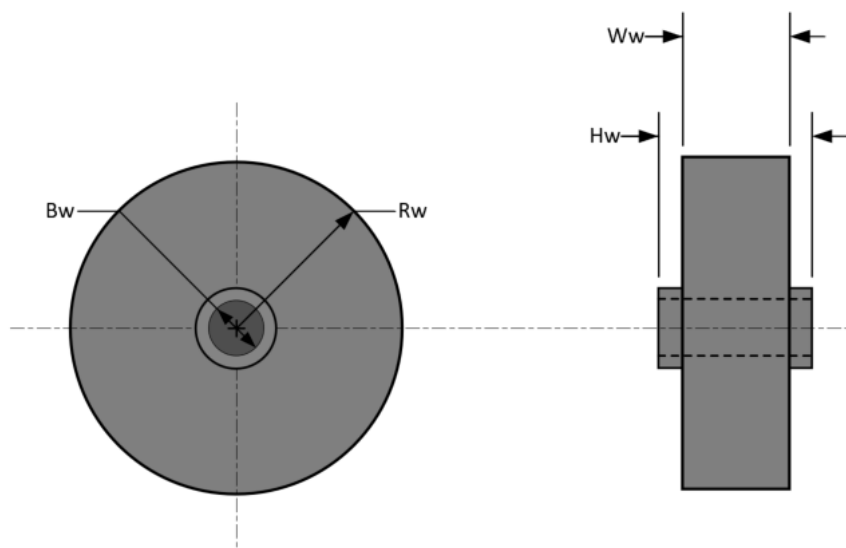


Figure 3.8: Minimum Edge Distance and Spacing for Holes in accordance with EN-1993 (Steelwork, ECCS - European Convention for Constructional 2017)

## Wheel

The wheel dimensions forming the important design parameters for much of the system are:

1. Wheel (w) radius  $R_w$
2. Wheel width  $W_w$
3. Hub width  $H_w$
4. Bore (axle diameter)  $B_w$



Wheel Geometry

Figure 3.9: Key Wheel Dimensions for System Design

The design of the wheel structure is outlined in Figure 3.10, 3D-printing is assumed to be a feasible method of manufacture:

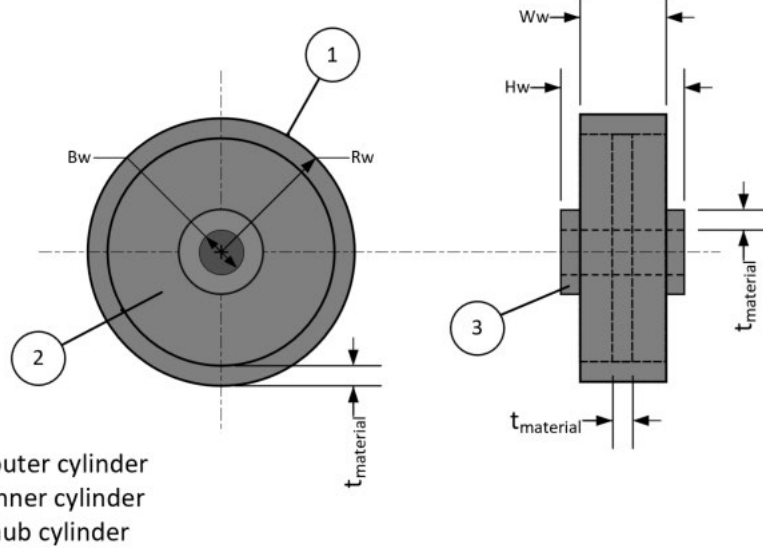


Figure 3.10: Wheel Details Including Material Thickness and Geometric Simplifications

The approximate weight of each part in the Trailing Arm subsystem is key to accurate performance modelling and detailed design of the instrument. The volume ( $m^3$ ) of the wheel material is required, with reference to Figure 3.10 where wheel volume  $V_w = V_{1_{wheel}} + V_{2_{wheel}} + V_{3_{wheel}}$ .

The outer cylinder (1) is the rolling/bearing surface, with a thickness of  $t_{material}$

$$V_{1_{wheel}} = \pi R_w^2 \cdot W_w - \pi (R_w - t_{material})^2 \cdot W_w \quad (3.6)$$

The inner cylinder (2) is a 3mm cylindrical plate, between the outer cylinder (1) and hub cylinder (3)

$$V_{2_{wheel}} = \pi (R_w - t_{material})^2 \cdot t_{material} - \pi (B_w + t_{material})^2 \cdot t_{material} \quad (3.7)$$

The hub cylinder (3), for the purpose of volume and weight calculations, assumes the bore is filled with an axle of the same material properties as the wheel

$$V_{3_{wheel}} = \pi (B_w + t_{material})^2 \cdot H_w \quad (3.8)$$

The mass of the wheel in kg can be determined, using the design approximation for material density:

$$M_{wheel} = \rho_{design} (V_{1_{wheel}} + V_{2_{wheel}} + V_{3_{wheel}}) \quad (3.9)$$

The centre of mass of the wheel relative to pivot point  $A$  in the  $AC$  axis:

$$CoM_{wheel} = ACmm \quad \text{from point } A \quad (3.10)$$

The dimension  $AC$  is dependent on the yoke and trailing arm design that follows.

### Yoke

The partially-assembled views in Figure 3.11 represent the trailing arm-yoke-wheel combination. Detailed assembly drawings and instructions for the prototype are not included here.

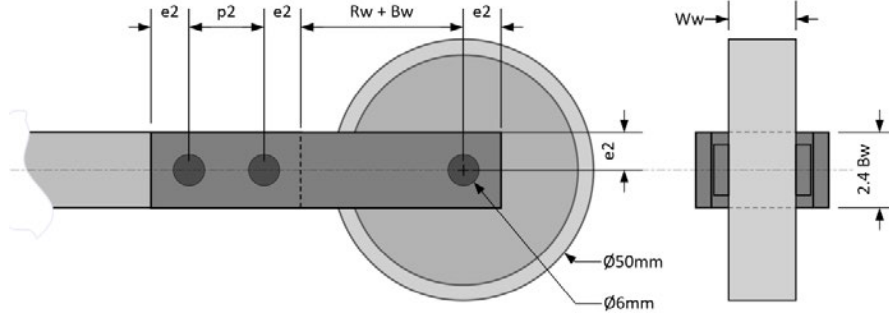


Figure 3.11: Wheel-Yoke-Arm Detail Drawing - 25mm Radius Wheel - 6mm Diameter Wheel Bore

The volume ( $m^3$ ) of the yoke material for non-drilled plates and referring to the length of each plate left-to-right in Figure 3.11:

$$V_{plate} = 2.4Bw(e_2 + p_2 + e_2 + Bw + Rw + e_2)t_{material} \quad (3.11)$$

Yoke volume  $V_{yoke}$ :

$$V_{yoke} = 2.V_{plate} = 2[2.4Bw(e_2 + p_2 + e_2 + Bw + Rw + e_2)t_{material}] \quad (3.12)$$

The mass of the yoke in kg can be determined, using the design approximation for material density:

$$M_{yoke} = \rho_{design}V_{yoke} \quad (3.13)$$

The centre of mass of the yoke relative to pivot point  $A$  in the  $AC$  axis:

$$CoM_{yoke} = \left[ (AC + e_2) - \left( \frac{3.e_2 + p_2 + Rw + Bw}{2} \right) \right] mm \quad \text{from point } A \quad (3.14)$$

### Trailing Arm Design

The trailing arm is shown in Figure 3.12 with the yoke plates removed for clarity. The standards for edge distance and hole spacing have been applied. The pivot point  $A$  shall be designed with an equivalent bore diameter to that used for the wheel ( $Bw$ ).

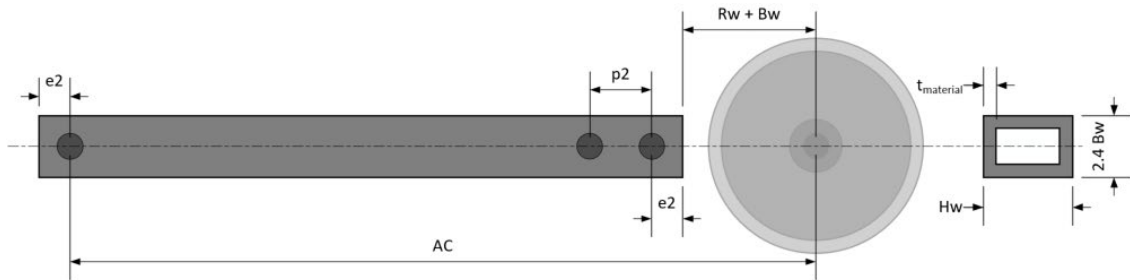


Figure 3.12: Trailing Arm Component Dimensions and Profile

The trailing arm is a simple component, however the derivation of length  $l_{arm}$  and  $AC$  is relatively complex in comparison. The process of deriving  $AC$  with reference to a geometric model of the workspace, is shown in Figure 3.13. The model depicts the wheel positioned at the point on the work surface where the wheel-tissue interaction commences. The arm must be fixed at point  $A$  a suitable distance and angle from the wheel axle point  $C$  to achieve maximum clearance between the arm and the workpiece.

Determination of design dimension  $AC$  involves the following parameters and conditions:

1. Pivot point  $A$  elevation  $AZ$  (user-defined parameter)
2. Workpiece surface elevation  $Rms$  (user-defined parameter)
3. Wheel radius  $Rw$  (user-defined parameter)
4. The height of the trailing arm  $h_{arm} = 2.4Bw$ , minimised for hole edge clearance in the yoke/arm assemblies, based on wheel bore  $Bw$



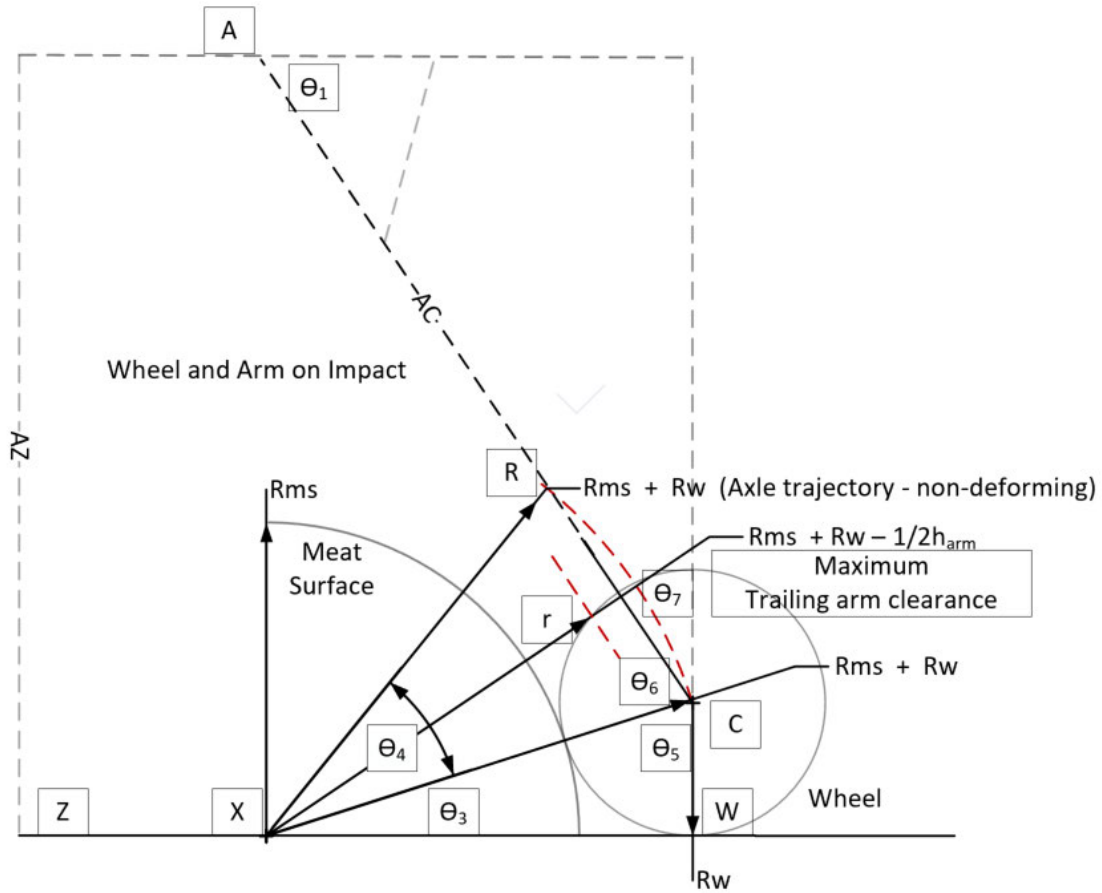


Figure 3.13: Trailing Arm and Roller Dimensions and Clearances

$AC$  calculations begin with determining  $\Theta_3$  at the point of impact between the wheel and workpiece.  $XC$  is the radial distance between wheel and workpiece centres, with  $R_w$  being the vertical height of the wheel centre  $C$ :

$$\Theta_3 = \sin^{-1} \frac{R_w}{R_{ms} + R_w} \quad (3.15)$$

$\Theta_4$  is determined using the formula for finding the angle  $\Theta$  inside a circle segment, when the radius  $R$  and the central distance  $r$  to the chord  $a$  has been defined (Weisstein 2020). Refer to the following schematic (Figure 3.14) detailing the mathematics, where the trailing arm alignment has been set using  $XC$  as distance  $R$  and the maximum central distance  $Xr$  is the workpiece radius plus the distance to the lower surface of the trailing arm:

## Circular Segment

DOWNLOAD  
Wolfram Notebook

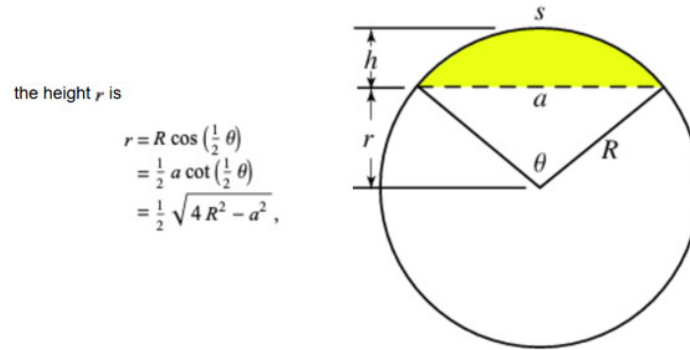


Figure 3.14: Circle Segment Definition and Mathematics (Weisstein 2020)

Therefore, to find the angle  $\Theta_4$  when the wheel follows a non-deforming workpiece trajectory and the central-distance to the chord  $CR$  accounts for trailing arm height:

$$\Theta_4 = 2\cos^{-1} \frac{R_{ms} + R_w - 1.2Bw}{R_{ms} + R_w} \quad (3.16)$$

$\Theta_5$  is the unknown angle  $\angle XCW$  in a right-triangle:

$$\Theta_5 = \frac{\pi}{2} - \Theta_3 \quad (3.17)$$

$\Theta_6$  is the unknown angle  $\angle XCR$  in the isosceles triangle:

$$\Theta_6 = \frac{\pi - \Theta_4}{2} \quad (3.18)$$

$\Theta_7$  is the unknown angle along the line segment extending vertically from  $WC$ :

$$\Theta_7 = \pi - \Theta_5 - \Theta_6 \quad (3.19)$$

Finally, the  $AC$  dimension is determined based on pivot point elevation  $AZ$  and  $\Theta_7$ :

$$AC = \frac{AZ - R_w}{\cos(\Theta_7)} \quad (3.20)$$

The design-length of the trailing arm  $l_{arm}$  is calculated using  $AC$ :

Trailing arm length in m:

$$l_{arm} = AC + 2.4Bw \quad (3.21)$$

Trailing arm height in m:

$$h_{arm} = 2.4Bw \quad (3.22)$$

Trailing arm width in m:

$$w_{arm} = Hw \quad (3.23)$$

Wheel geometry largely influences the limitations around mechanism design and the ability to maintain trailing arm clearance  $gap$  from the workpiece when surface deformation is occurring (Figure 3.15).

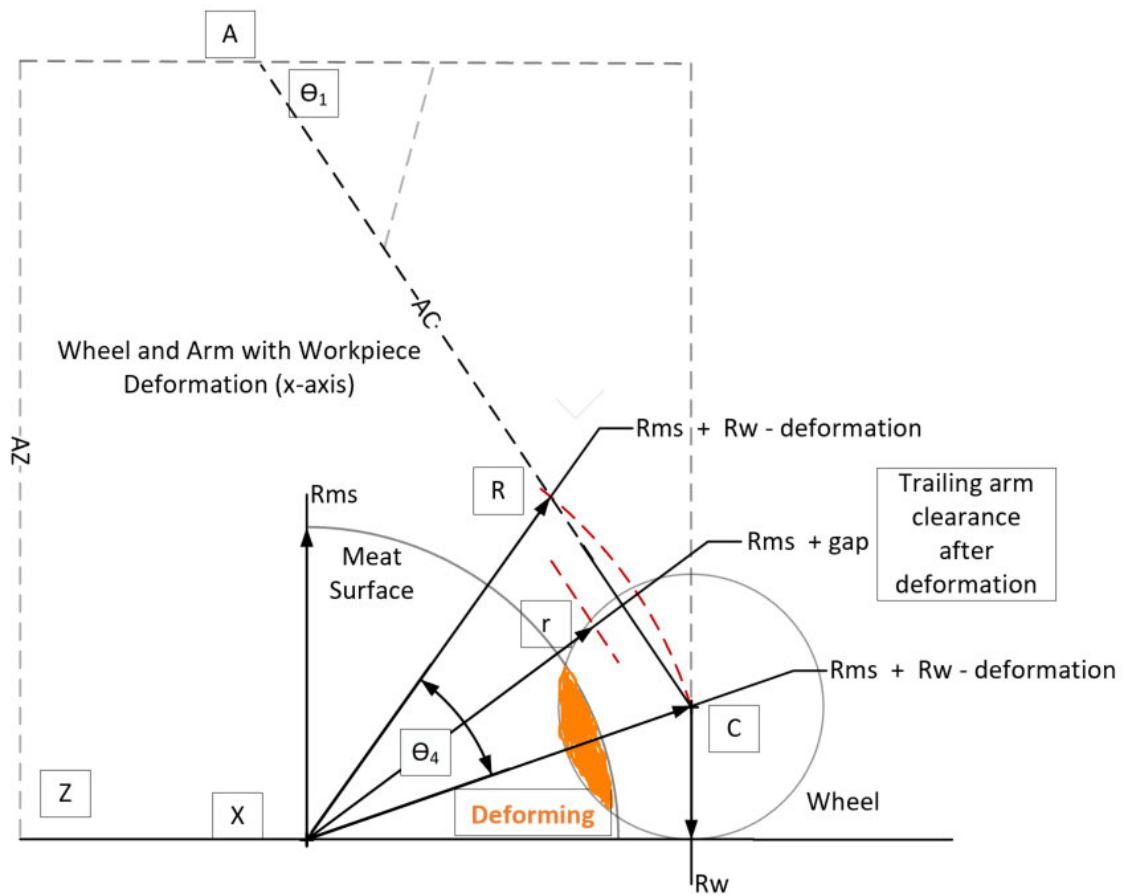


Figure 3.15: Wheel-tissue Interactions with Modelled Trailing arm and Wheel Mechanism for Deforming Workpiece

The volume ( $m^3$ ) of the trailing arm material is required, with reference to Figure 3.12.

Assuming the case for a non-drilled arm:

$$V_{arm} = (AC + 2e_2)(4.8Bw + 2Hw)t_{material} \quad (3.24)$$

The mass of the trailing arm in kg can be determined:

$$M_{arm} = \rho_{design} V_{arm} \quad (3.25)$$

The centre of mass of the trailing arm relative to pivot point  $A$  in the  $AC$  axis:

$$CoM_{arm} = \left( \frac{AC + e_2 - Rw - Bw}{2} \right) \text{ mm from point } A \quad (3.26)$$

### Spring Mechanism Subsystem

**Simplifying Assumptions** The Spring Mechanism subsystem comprises the active mechanical component of the instrument system and a retainer assembly providing mechanical attachment functions over the dynamic range of spring and mechanism travel. Spring design is an iterative process, initially focussed on the spring constant, the amount of spring force applied at Initialisation Mode (Preload force) and the range of spring force applied as the instrument wheel traverses the workpiece.

A design decision has been made to approach the problem of spring design with a modular spring mechanism that mounts at point  $B$  on the trailing arm and point  $D$  on the support. Custom manufacture (3D printing) will be necessary for manufacture of spring retainers that integrate a compression spring/s with the trailing arm/support mechanism. Springs are available (Misumi Corporation 2020) across the expected range of stiffness characteristics reported in the literature review (Section 2.2). The instrument should ideally exhibit stiffness characteristics similar to the workpiece, while also deforming the surface.

### Spring

The prototype spring/s design concept is provided in Figure 3.17. The design allows for different length springs to be installed for experimentation and modelling of different combinations of instrument and workpiece stiffness. The data sheets for recommended springs are available in Appendix B.

The critical dimensions and properties of the spring:

1. Free length ( $l_{free}$ ) - Uncompressed length of the spring. This length is constrained

by the availability of a suitable position on the trailing arm to mount hardware to establish  $l_{preload}$  between the bearing surfaces of the retainers at point  $B$  on the arm and  $D$  on the upper support

2. Solid length - The fully compressed length of the spring. The instrument must not cause the spring to reach this dimension at maximum elevation over the workpiece
3. Compression ratio - The maximum length of compression recommended by the manufacturer, maintaining a margin from reaching solid length
4. Spring diameters (inner  $I.D_{spring}$  and outer  $O.D_{spring}$ ) increase during compression. The design mounts the spring/s on a rod to prevent restriction of the spring coil expansion and reduce friction/binding during compression (Associated Spring, Barnes Group Inc. 2005).
5. Slenderness ratio and buckling - The slenderness ratio of free length:mean diameter (M.D) ( $M.D = \frac{I.D_{spring} + O.D_{spring}}{2}$ ) is a useful indicator of spring buckling tendency, which is represented in Figure 3.16 .

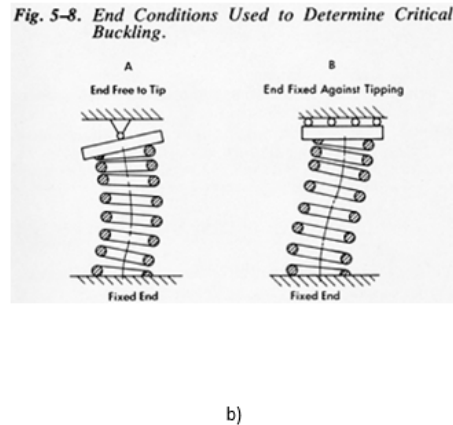
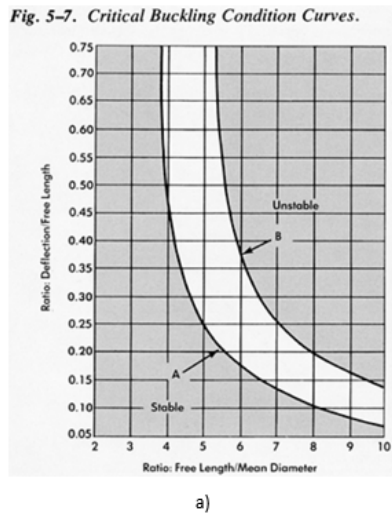


Figure 3.16: Spring Buckling, Slenderness Ratio, Compression ratio, End Fixture (Associated Spring, Barnes Group Inc. 2005)

6. The modelled instrument design utilises springs from the Misumi Corporation (2020) that includes a range of springs with 75% compression:free-length ratios. The design fixes the spring-ends between parallel plates through mechanical rod interfaces. Therefore, curve B in Figure 3.16a) provides guidance on the potential slenderness ratio, which is  $\lesssim 5.3$ .

**Retainer**

The hinging motion of the spring retainers, represented graphically in the design-concept diagrams Figure 3.17, is necessary to allow the retainers to maintain parallel-plate supports for the spring as the trailing arm angle changes. The rods prevent spring buckling under compression, and the friction is assumed to be negligible.

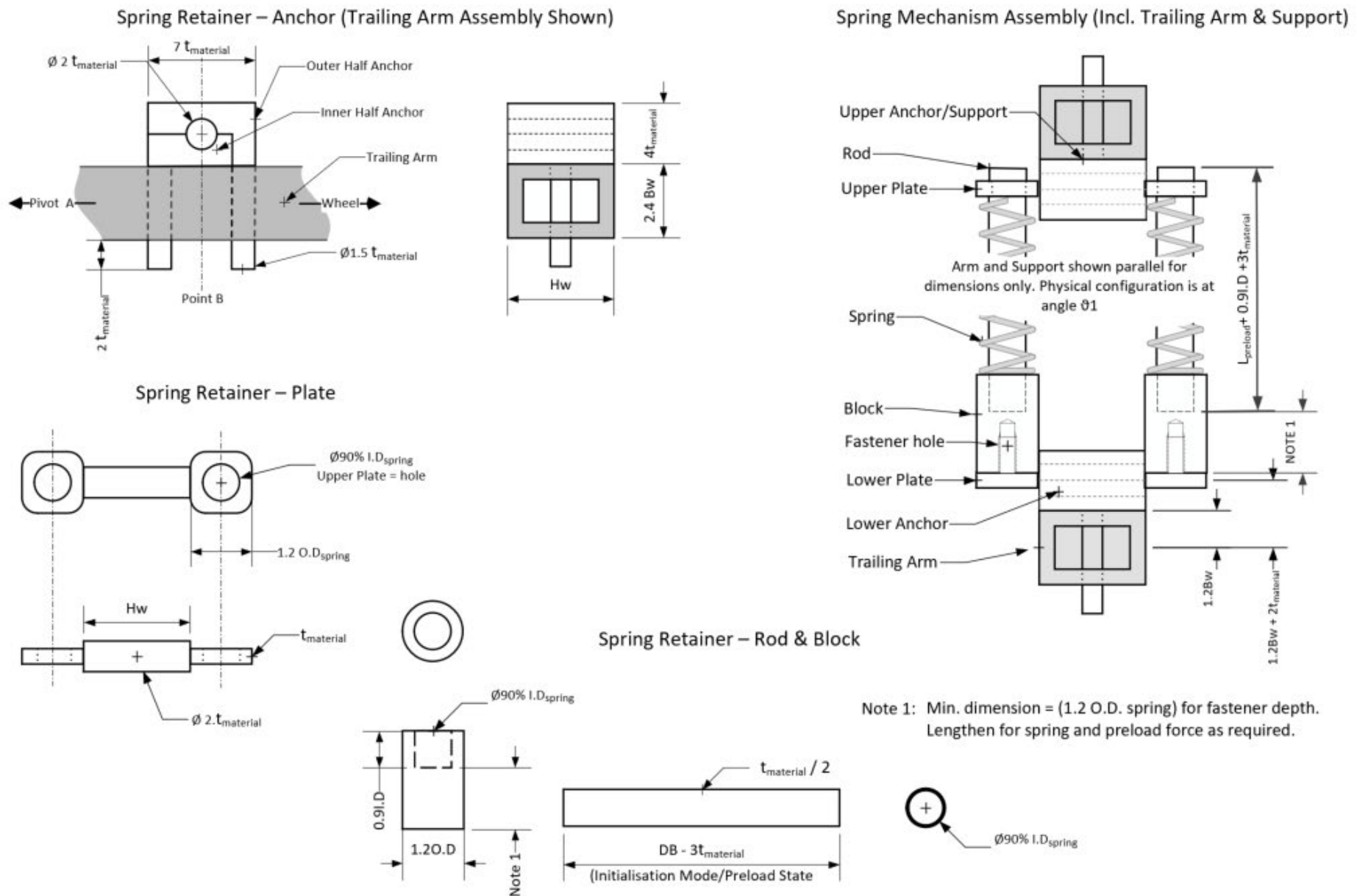


Figure 3.17: Spring Mechanism - Parts and Assembly Drawings

### Spring Mechanism Assembly

The volume ( $m^3$ ) of the spring mechanism parts material is required, with reference to Figure 3.17. Assuming the case for non-drilled components:

#### Spring Retainer - Plates

$$V_{plates} = 2[2(1.2O.D_{spring})^2 t_{material} + \pi(t_{material})^2 Hw] \quad (3.27)$$

Note, the Spring Mechanism contains 2 plates (upper and lower). Eq.3.27 combines both plates.

#### Spring Retainer - Anchors

$$V_{anchors} = 2[4t_{material}6t_{material}Hw - \pi(t_{material})^2 Hw + 2\pi(0.75t_{material})^2(2.4Bw + 2t_{material})] \quad (3.28)$$

Note, the anchor volume is approximated as a rectangular block with a cylindrical hole, and two attachment cylinders. Eq.3.28 combines inner and outer anchors. This volume Eq.3.28 accounts for both anchor assemblies.

#### Spring Retainer - Rods and Blocks

$$V_{rods} = 2[\pi 0.9I.D_{spring}(l_{preload} + 0.9I.D_{spring} + 3(t_{material}))\frac{t_{material}}{2}] \quad (3.29)$$

Note, the rod volume is approximated as a pair of hollow cylinders. Eq.3.29 combines both rods.

$$V_{blocks} = 2[\pi(0.6O.D_{spring})^2 l_{block} - \pi(0.45I.D_{spring})^2 0.9I.D_{spring}] \quad (3.30)$$

Note, the block volume is approximated as a pair of solid cylinders with bores to accommodate the rods. Eq.3.30 combines both blocks.

### Springs

$$V_{springs} = \pi O.D_{spring1} l_{solid1} \frac{O.D - I.D_{spring1}}{2} + \pi O.D_{spring2} l_{solid2} \frac{O.D - I.D_{spring2}}{2} \quad (3.31)$$

Note, the volume of a spring is approximated as a hollow cylinder of solid-length, wire-thickness and outer-diameter. Eq. 3.31 accounts for both springs, including where different length springs are implemented.



The mass of the spring mechanism retainer in kg can be determined, using the design approximation for material density  $\rho_{design} = 1800kg/m^3$  and spring-steel density in ASTM 228 spring steel  $\rho_{spring} = 7800kg/m^3$  (MatWeb 2020), (Misumi Corporation 2020):

$$M_{springMech} = \rho_{design}V_{plates} + V_{anchors} + V_{rods} + V_{blocks} + \rho_{spring}V_{springs} \quad (3.32)$$

The centre of mass of the spring mechanism relative to pivot point  $A$  in the  $AC$  axis:

$$CoM_{spring} = AB \quad \text{mm from point } AC \quad (3.33)$$

### Support Subsystem

Due to restrictions on access to USQ laboratories and the decision to focus on design modelling over manufacture, the tool-support interface and Support subsystem design has not been developed.

### Model Beef Workpiece

Workpiece simplifying assumptions have been made to define the structure of the beef striploin and support the modelling and design approach of the project. Following discussion with the project supervisor Peter Brett, the following simplifying assumptions have been made:

1. The representative feature is a flexible arch structure of given radius and stiffness, cantilevered from the horizontal table on which the roller initially rolls
2. The meat stiffness is represented by the selected structure geometry in bending
3. The arch structure reflects the chilled fat layer that is a stiff component of the structure
4. Small beam theory applies
5. The meat does not slip on the surface.

### 3.2.2 Prototype Instrument Product Baseline

Applying the functional and system specifications to the design software tools in the BOM Model (App.C) produced a prototype instrument and workpiece baseline, presented as a scale drawing in Figure 3.18 below:

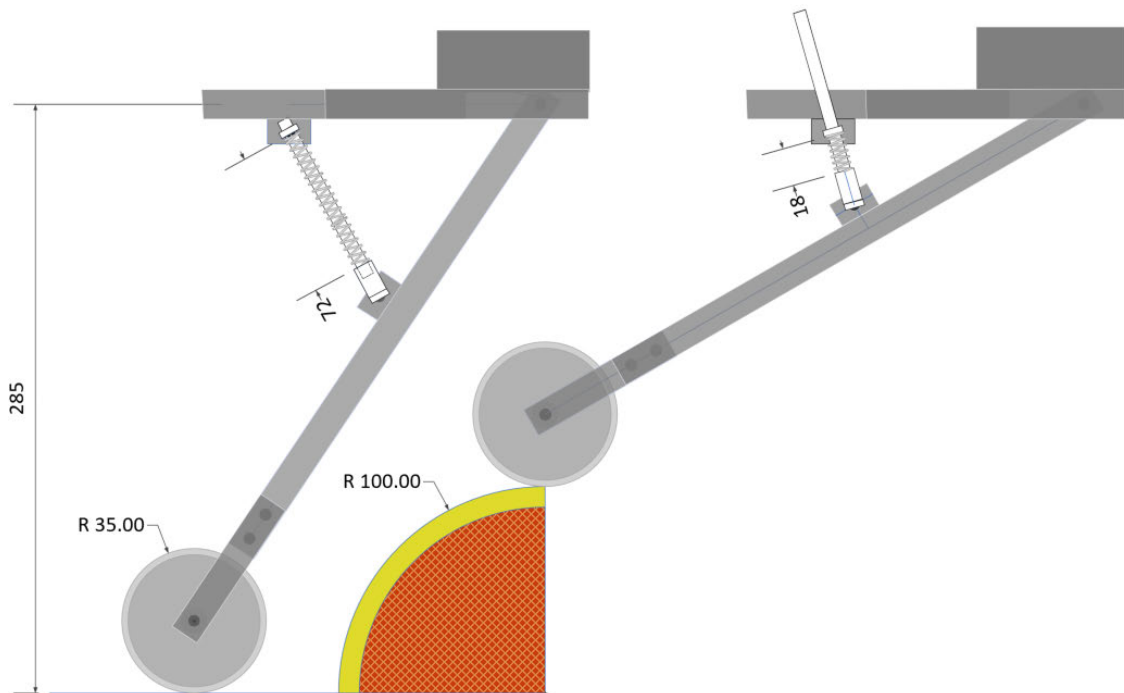


Figure 3.18: Prototype Instrument and Workpiece Scale Drawing

The component BOM and extracts from the associated piece-part drawings are provided below. The components require custom manufacture using 3-D printing technology. Appropriate drawing files (e.g. .stl files) are not provided in this report.

Wheel

Wheel	Mass	Rw	Ww	Bw	Hw
TSI-35/10-6/15-100-1.8/100	0.034	0.035	0.01	0.006	0.015
	kg	m	m	m	m

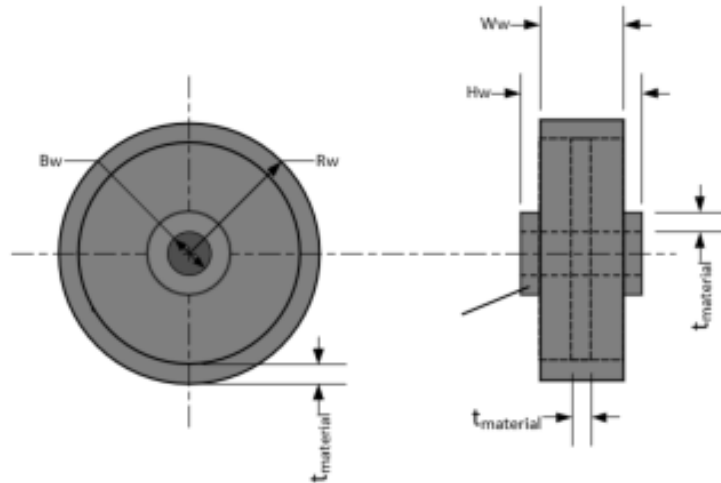


Figure 3.19: Wheel BOM and Piece-part Drawing

Trailing Arm

Trailing Arm	Mass	$l_{arm}$	$h_{arm}$	$w_{arm}$
TSI-35/10-6/15-100-1.8/100	0.100	0.2671	0.0144	0.015
	kg	m	m	m

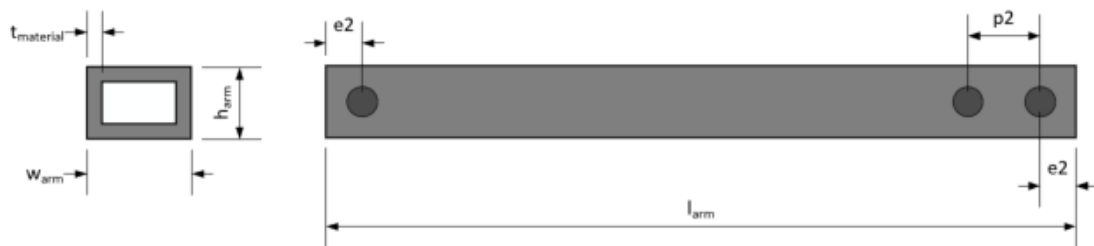


Figure 3.20: Trailing arm BOM and Piece-part Drawing

Yoke

Yoke	Mass	$l_{yoke}$	$h_{yoke}$	$w_{yoke}$
TSI-35/10-6/15-100-1.8/100	0.012	0.077	0.014	0.003
	kg	m	m	m

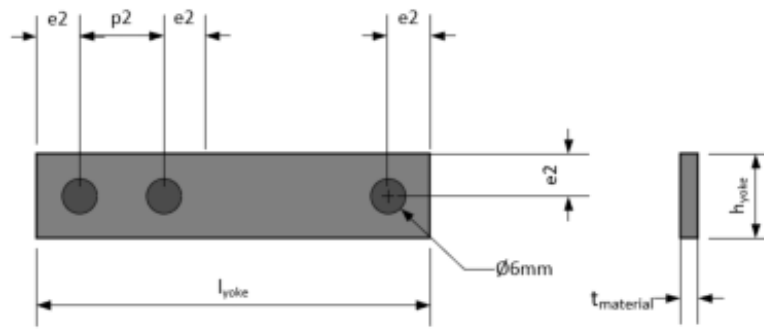


Figure 3.21: Yoke BOM and Piece-part Drawing

Spring Mechanism

Spring Mechanism	Mass								
TSI-35/10-6/15-100-1.8/100	0.032								
	kg								
Spring 1	Mass	$l_{free}$	$l_{solid}$	O.D	I.D	$d_{wire1}$	k1	CR1	
WY series (75% CR)	0.002	0.070	0.0126	0.008	0.0066	0.0007	100	0.75	
p/n: WY8-70	kg	m	m	m	m	m	m	m	
Spring 2	Mass	$l_{free}$	$l_{solid}$	O.D	I.D	$d_{wire2}$	k2	CR2	
WY series (75% CR)	0.002	0.07	0.0126	0.008	0.0066	0.0007	100	0.75	
p/n: WY8-70	kg	m	m	m	m	m	m	m	
Anchor (inner)	Mass*	l	h	w					
TSI-35/10-6/15-100-1.8/100	0.003	0.017	0.026	0.015					
QTY 2 *Mass=1/4 total	kg	m	m	m					
Anchor (outer)	Mass*	l	h	w					
TSI-35/10-6/15-100-1.8/100	0.003	0.021	0.032	0.015					
QTY 2 *Mass=1/4 total	kg	m	m	m					
Plate	Mass*	l	h	w					
TSI-35/10-6/15-100-1.8/100	0.002	0.034	0.006	0.010					
QTY 2 *Mass = 1/2 total	kg	m	m	m					
Rod & Block	Mass	$l_{rod}$	O.Drod	I.Drod	$l_{block}$	$\Delta l_{block}$			
TSI-35/10-6/15-100-1.8/100	0.006	0.086	0.006	0.003	0.016	0.000			
QTY 2 *Mass = 1/2 total	kg	m	m	m	m	m			

Figure 3.22: Spring Mechanism BOM

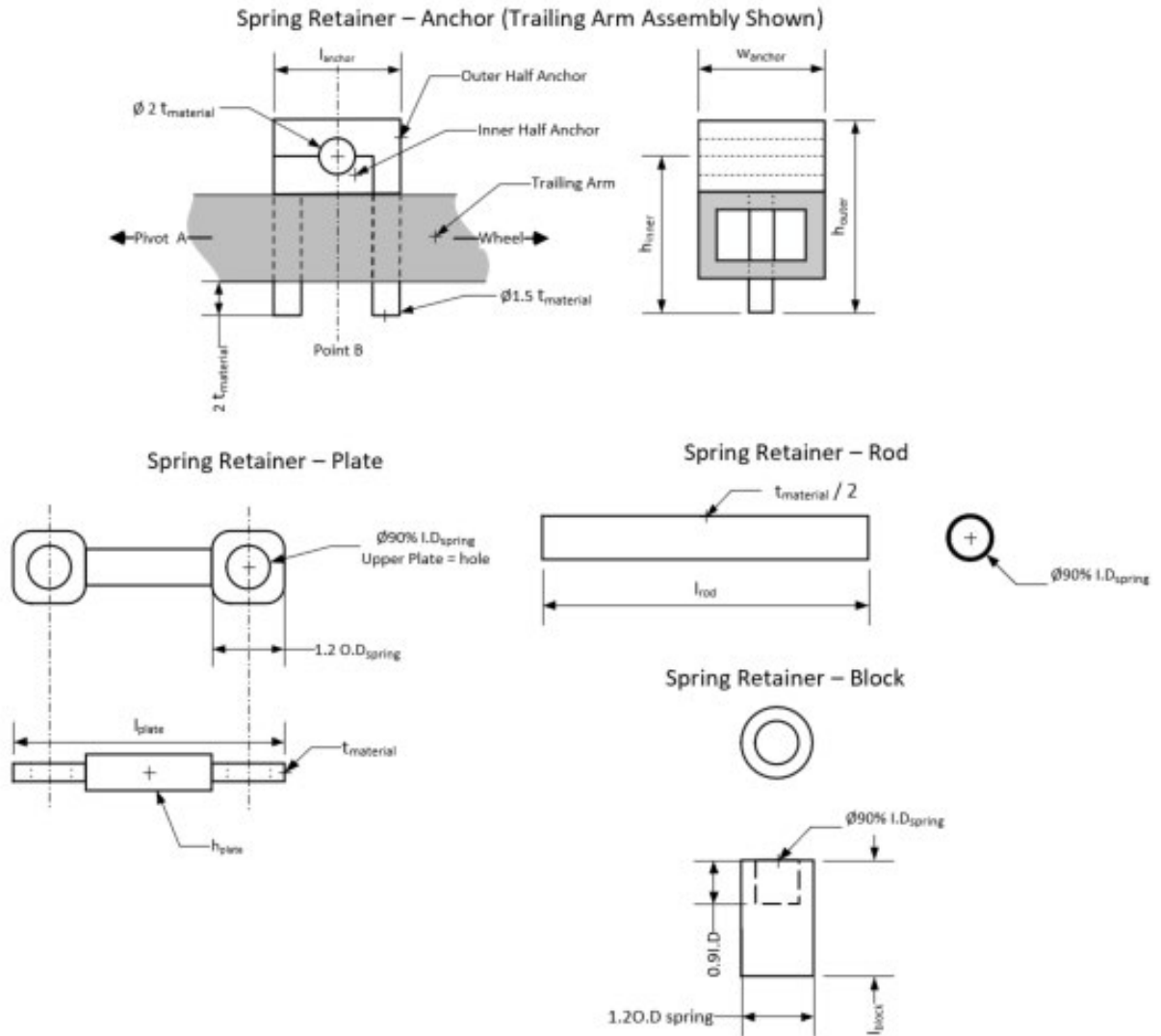


Figure 3.23: Spring Mechanism Piece-part Drawing

### 3.3 Design Outcomes

The formal design process has produced a product baseline/bill of materials, derived from a relatively simple set of user-defined parameters for the wheel and workpiece. The prototype instrument meets the interface requirements for the test rig and the expectations for the range of workpiece dimensions given in the literature and from researchers at USQ CAE.

The kinematics of the assembly have been defined, with inverse kinematics available to track the wheel deflections as the modelled workpiece deforms. Spring mechanism characteristics apply in the force models in the next chapter, establishing the maximum

contact force available at the workpiece surface.

The wheel reaction forces are considered to be a concentrated load in Roark's formulas for stress and strain (Young & Budynas 2002). Therefore the radius of the wheel is not directly applied in calculations. Performance model results are required before the choice of wheel radius can be assessed in terms of the local deformation stress under the wheel. The estimates of spring and damper constants were taken from results in the literature (Moreira et al. 2012), and the comparison of experimental parameters from the research with predicted instrument/workpiece interactions and responses are required to evaluate the validity of initial design parameter sizing.

The output of the instrument is essentially the angle of deflection of the trailing arm, from the preload state through the range of the sensing state. This angle is known relative to the wheel trajectory, therefore preliminary instrument specifications such as sensitivity and discrimination could be predicted in advance of future experimentation with the prototype. For the prototype instrument, an angular deflection of only  $0.34^\circ$  for one millimetre y-axis wheel deflection from the work surface, to  $2.2^\circ$  at the top of the arch.

A suitable transducer is the final hardware and electronic/software design element. The selection of a suitable product for this role will require analysis of performance models in the following chapter.

# Chapter 4

## Performance Modelling

### 4.1 Force Characteristics - Prototype Instrument

The static force characteristics of the prototype instrument are modelled in this chapter, beginning with a free-body diagram of the instrument to establish the key external force components. These forces comprise instrument weight  $F_M$ , spring force  $F_{DB}$ , the wheel reaction force  $F_C$ , and test-rig towing force  $F_x$ , derived from dimensions of the prototype instrument and sample workpiece. These parameters are applied to a series of static (Roark's) and quasi-static (System) force models, generating 1mm step-wise approximations of applied forces and workpiece surface deformations.

#### 4.1.1 Instrument Weight and Balance

External force balancing for the instrument is determined for the two operating states:

1. Preload - The instrument is attached to the test rig, the tool attachment is adjusted in elevation to position the trailing arm pivot at dimension  $AZ = 285mm$  and the wheel is on the work surface of the rig (see Figure 4.1). The prototype has been designed with 70mm springs that fit uncompressed at the preload state. The preload force  $F_C$  therefore is the weight of the instrument.

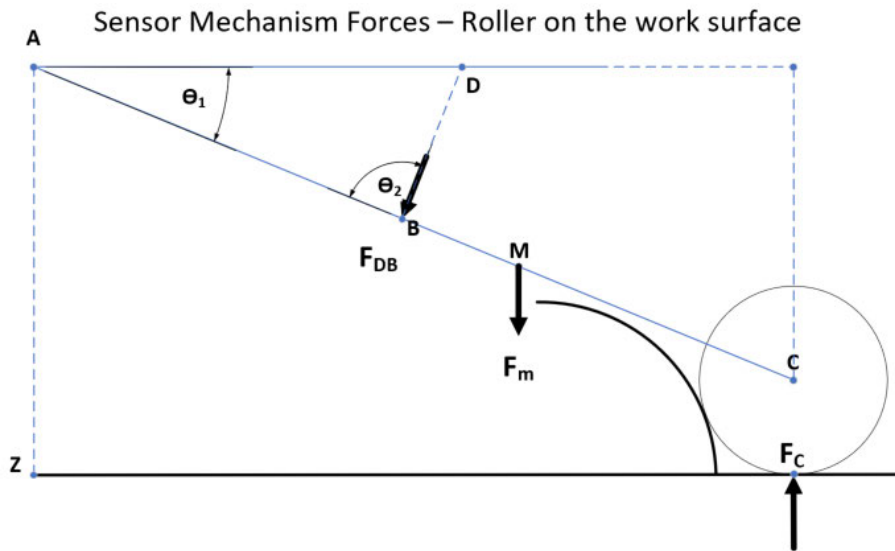


Figure 4.1: Preloaded Instrument FBD

2. Sensing - The instrument has been moved in the x-axis by test-rig force  $F_x$ , positioning the wheel in full contact with the workpiece. Wheel reaction force  $F_C$  is radial to the model workpiece arch and wheel (see Figure 4.2). The springs compress once the wheel leaves the work surface, applying spring force  $F_{DB}$  in combination with weight  $F_M$  to establish the wheel reaction force  $F_C$ .

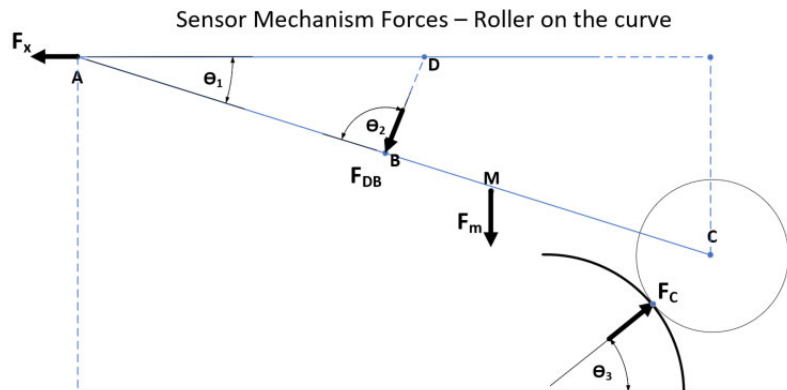


Figure 4.2: Instrument in Sensing State FBD

The weight  $F_M$  is calculated through summation of the forces and arms of the major components of the system: See Figure 4.3



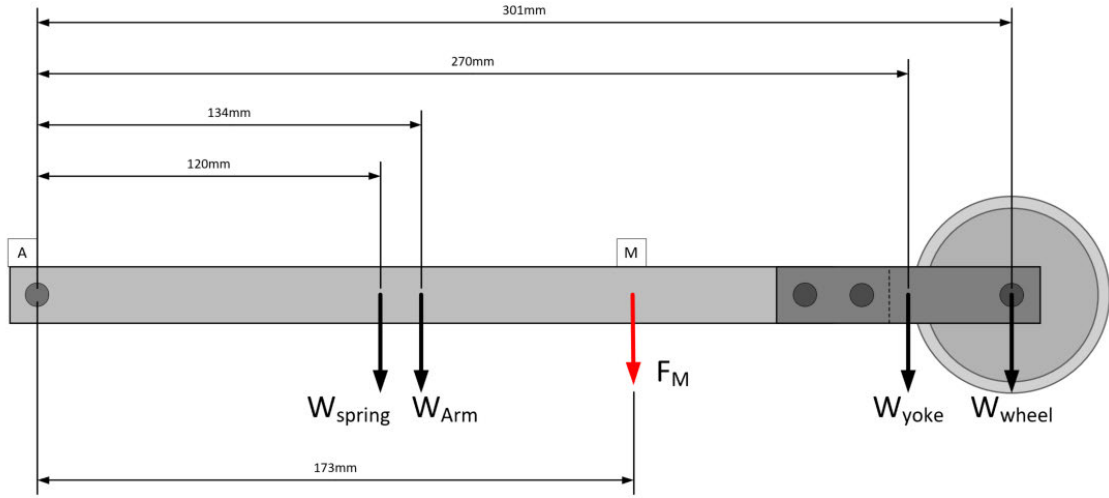


Figure 4.3: Centre of Gravity - Trailing arm and wheel Assembly (NTS)

The system/subsystem mass and balance characteristics were calculated in the prototype instrument design tools used to establish the bill of materials in Section 3.2.2. Weight  $F_M$  is then determined using the following calculations from Hibbeler (2010):

1. Total weight force  $F_M$  is the sum of all component weights  $W_{component}$ , where  $W_{component} = M.g$  ( $M$  = mass and gravity constant  $g = 9.81m.s^{-1}$ ):

$$F_M = W_{arm} + W_{wheel} + W_{yoke} + W_{spring} \quad (4.1)$$

2. The weight of each component acts through the centroid of the component, with a moment arm in the x-axis relative to pivot point  $A$ . The arm longitudinal centroid distance ( $dist_{component}$ ) for each component is provided in Figure 4.3:
3. The distance along the arm where effective instrument weight  $F_M$  acts (Point  $M$ ), relative to the pivot point  $A$ , is calculated using the following equation:

$$AM = \frac{(W_{arm} * dist_{arm} + W_{wheel} * dist_{wheel} + W_{yoke} * dist_{yoke} + W_{spring} * dist_{spring})}{F_M} \quad (4.2)$$

4. The prototype instrument position of the centre of gravity Point  $M$  relative to pivot point  $A$  is therefore:

$$AM = 173mm \quad (4.3)$$

4.1.2 Spring Force

The forces applied by the instrument over the workpiece are approximated to establish a maximum force profile, resulting from wheel-travel over a non-deforming arch. Figure 4.4 is a simplification of force vectors and the trigonometric relationships between them. Wheel reaction force  $F_C$  is also shown acting at the wheel centre, which is assumed to be the same force at the wheel-arch interface given a rigid wheel.

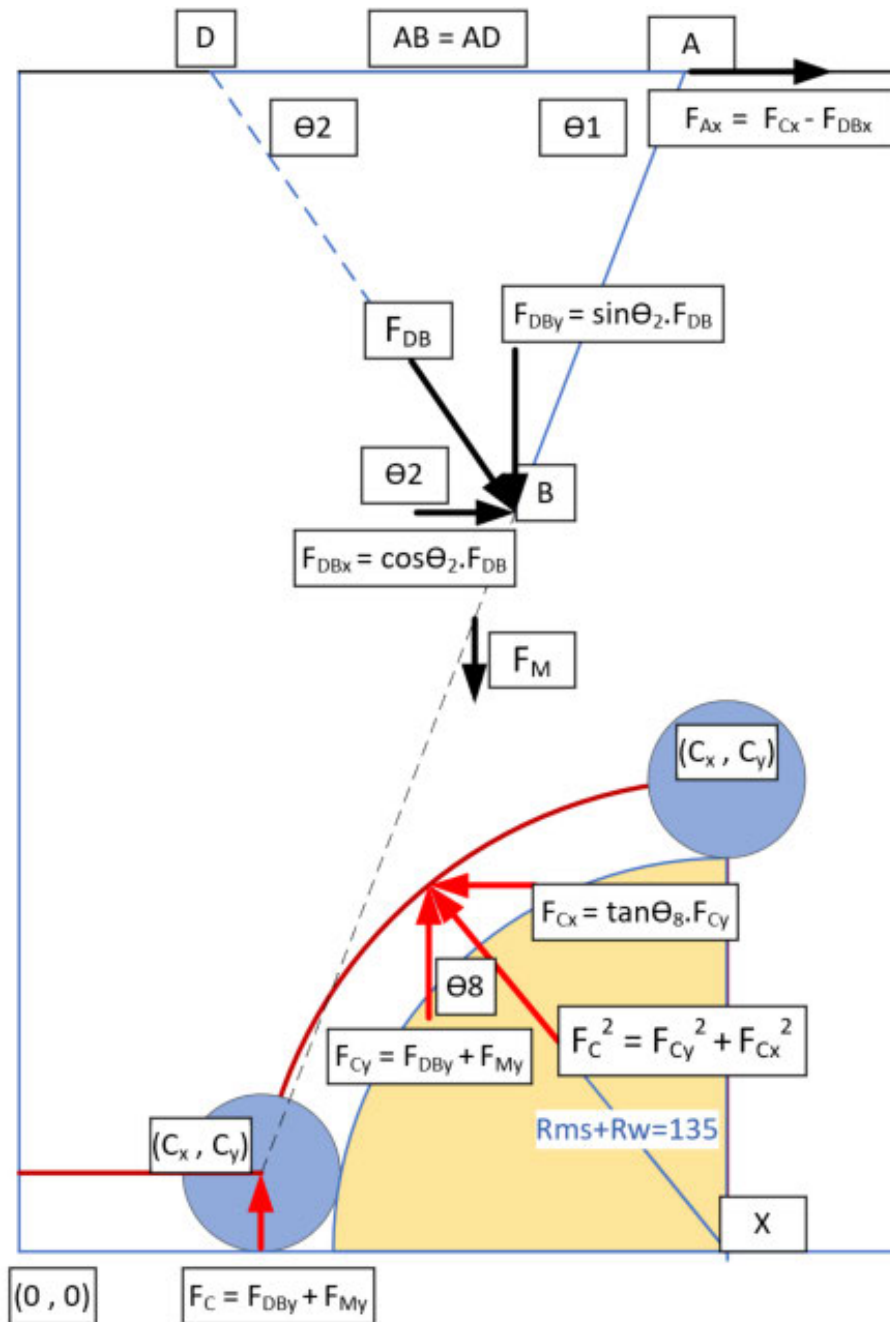


Figure 4.4: Static Force Balance in the Work Space (NTS)

Tracking the wheel axle centre  $C$  through a trajectory  $(C_x, C_y)$  (shown in red) over the workpiece is the basis for determining the wheel reaction force profile over the workpiece. The wheel centre position in the workspace is known throughout the modelling process, and the salient design parameters can also be determined from these coordinates. An important design angle,  $\theta_1$  provides both a reference point to understand the configuration of the instrument, and an output parameter sensitive to interactions at the wheel-tissue interface. As  $C_y$  is known in the model-space:

$$\Theta_1 = \sin^{-1} \frac{(AZ - C_y)}{AC} \quad (4.4)$$

Spring design is based on the deflection of the spring element shown in Figure 4.4 as segment  $DB$ . This approximation also refers to the angle  $\theta_2$ , at which the spring force  $F_{DB}$  is assumed to be acting on the arm at any given time. The prototype baseline includes a spring mechanism anchored at points  $B$  and  $D$ , where  $AB = AD$ , therefore  $\theta_2$  is one of two equal angle in the isosceles triangle  $ABD$ :

$$\Theta_2 = \frac{\pi - \Theta_1}{2} \quad (4.5)$$

The prototype instrument spring mechanism configuration is more complex than the distance  $DB$  however, and the length of the spring  $l_{spring}$ , (see Figure 4.5) and calculations of applied spring force  $F_{DB}$  are determined as follows:

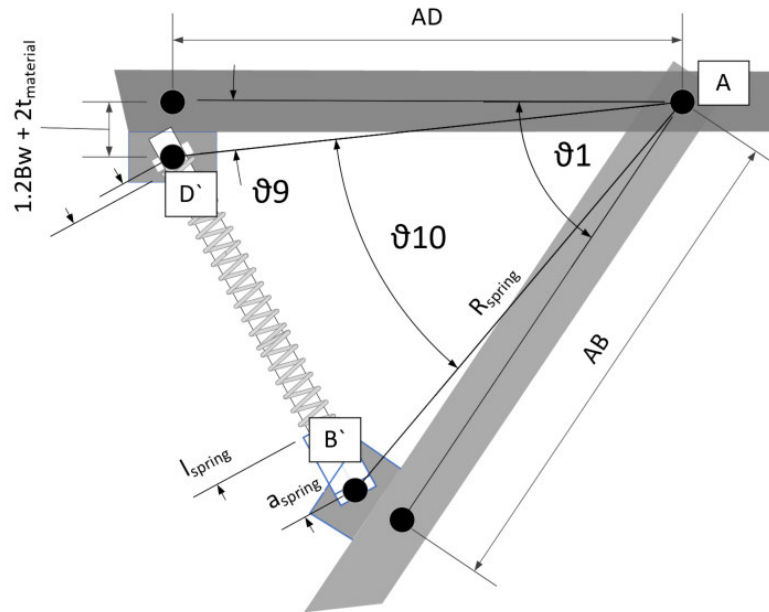


Figure 4.5: Spring Mechanism Detailed View - Spring Length and Angles

Material specifications for the spring anchors and retainers have established two new pivot points for the springs,  $B'$  and  $D'$ , perpendicularly equidistant from the trailing arm and support points  $B$  and  $D$  respectively. This configuration requires another application of the circular segment formula (Weisstein 2020), determining the straight-line (chord) distance  $a$  across the segment  $D'AB'$  of radius  $R_{spring}$ . The applicable formula is provided in Figure 4.6:

### Circular Segment



The length of the chord is

$$\begin{aligned}
 a &= 2R \sin\left(\frac{1}{2}\theta\right) \\
 &= 2r \tan\left(\frac{1}{2}\theta\right) \\
 &= 2\sqrt{R^2 - r^2} \\
 &= 2\sqrt{h(2R - h)}.
 \end{aligned}$$

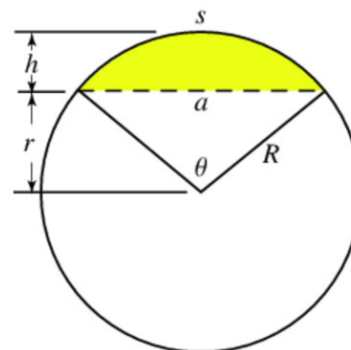


Figure 4.6: Circular Segment Formulas for Spring Motion (Weisstein 2020)

The spring mechanism anchor assembly sets up a right angled triangle  $ADD'$  at the Support mount and a geometrically equivalent triangle  $ABB'$  at the Trailing Arm. As the distances  $AD = AB$  and mounting pivot offset  $DD' = BB'$  are known,  $R_{spring}$  is

determined:

$$R_{spring} = \sqrt{AD^2 + DD'^2} \quad (4.6)$$

The angle  $\theta_9$  is then determined:

$$\theta_9 = \tan\left(\frac{DD'}{AD}\right) \quad (4.7)$$

Angle  $\theta_{10}$  is then the difference between  $\theta_1$  and twice  $\theta_9$ :

$$\theta_{10} = \theta_1 - 2\theta_9 \quad (4.8)$$

Length  $a_{spring}$  is found using the circular segment formula (Weisstein 2020):

$$a_{spring} = 2.R_{spring} \cdot \sin\left(\frac{\theta_{10}}{2}\right) \quad (4.9)$$

The spring force  $F_{DB}$  applied perpendicular to the Trailing Arm is calculated using the step-wise variations in length  $a_{spring}$  as the wheel travels over the workpiece in 1mm steps in the x-axis:

$$F_{DB} = \Delta a_{spring} \cdot k_{spring} \quad (4.10)$$

where  $k_{spring}$  is the nominal spring constant provided by the spring manufacturer. For the prototype, QTY 2 100N/m springs are installed, providing  $k_{spring} = 200N/m$ .

The applied spring force  $F_{DB}$  components in the x-axis and y-axis, as shown in Figure 4.4 , are calculated:

$$F_{DB_y} = \sin\left(\frac{\pi - \Theta_2}{2}\right) \cdot F_{DB} \quad (4.11)$$

$$F_{DB_x} = \cos\left(\frac{\pi - \Theta_2}{2}\right) \cdot F_{DB} \quad (4.12)$$

### 4.1.3 Wheel Reaction Force

The wheel reaction force  $F_C$  is key to proceeding with deformation modelling and predicting the performance of the prototype instrument over a representative workpiece sample.

Another angle is required,  $\theta_8$ , which is used to compose the force vector from the x and y-axis components of force acting at the wheel due to weight and spring forces. As Figure 4.4 shows:

$$F_{Cx} = \tan(\theta_8).F_{Cy} \quad (4.13)$$

Equating  $\tan\theta_8$  to  $C_x$  and  $C_y$ , for  $F_{Cx} = \tan\theta_8.F_{Cy}$  when the wheel is over the workpiece:

$$F_{Cx} = \frac{X - C_x}{C_y}.F_{Cy} \quad (4.14)$$

Where  $F_{Cy}$  is the sum of y-axis components of force applied by the instrument:

$$F_{Cy} = F_{DBy} + F_{My} \quad (4.15)$$

$\theta_8$  is found in a piecewise manner, either before the wheel contacts the arch or post wheel-tissue contact:

$$\theta_8 = \begin{cases} 0, & \text{if } C_x < [X - \sqrt{(Rms + Rw)^2 - Rw^2}] \\ \tan^{-1} \frac{X - C_x}{C_y} & \text{if } [X - \sqrt{(Rms + Rw)^2 - Rw^2}] \leq C_x \leq X \end{cases} \quad (4.16)$$

Finally, the wheel-tissue reaction force at any point before or after wheel-tissue contact is found:

$$F_C = \begin{cases} F_{DBy} + F_{My}, & \text{if } C_x < [X - \sqrt{(Rms + Rw)^2 - Rw^2}] \\ \sqrt{F_{Cy}^2 + F_{Cx}^2}, & \text{if } [X - \sqrt{(Rms + Rw)^2 - Rw^2}] \leq C_x \leq X \end{cases} \quad (4.17)$$

#### 4.1.4 Test Rig Towing Force

The force required to hold the wheel in the sensing state over the arch,  $F_{Ax}$ , is determined:

$$F_{Ax} = F_{C_x} - F_{DB_x} \quad (4.18)$$

This force is only an estimate of the force required to hold the wheel at any point on the non-deforming workpiece model. Additional margin for friction and bogging-down of the wheel at the tissue contact area will need to be considered. Discussions with the test rig designer indicate that 20N of towing force is available (Cooney 2020).

## 4.2 Static Workpiece Deformation Model

The structural model of an arched fat layer over the workpiece is the next step in building the system model. A maximum force  $F_C$  is assumed to be available at the instantaneous contact between the wheel and workpiece before deformation. Roark's formulas for stress and strain (Young & Budynas 2002) are applied to an arch structure with the applied force at one end and the lower end fixed.

Deformation results from the static model are based on an equilibrium condition after a static force remains in place. This is considered to be the maximum expected deformation, which feeds into the system model in the next section. The system model applies second-order time-based characteristics to the response, based on the viscoelastic meat layer underneath the relatively stiff, elastic fat layer on top.

### 4.2.1 Design parameters into the Static Force Model

The selection of models from Table 9.3 (Young & Budynas 2002) and case 5.c shall be used to determine the vertical and horizontal load terms with one end of the arch fixed to the work surface. The deflections are determined with general case 5 expressions provided in Table 9.3; case 5c defines the specific radial loading terms  $L_F$  (Young & Budynas 2002).

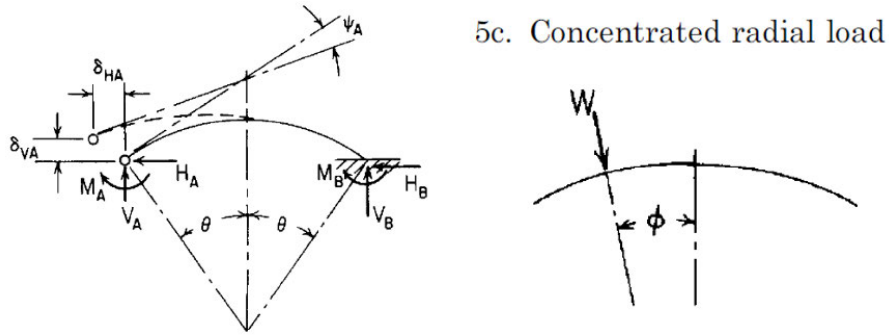


Figure 4.7: Equivalent Arch - Modelled Workspace and Roark's Formulas (Young & Budynas 2002)

ons for cases 5–14, right end fixed in all 10 cases.

Deformation equations:

$$\text{Horizontal deflection at } A = \delta_{HA} = \frac{R^3}{EI} \left( B_{HH}H_A + B_{HV}V_A + B_{HM} \frac{M_A}{R} - LF_H \right)$$

$$\text{Vertical deflection at } A = \delta_{VA} = \frac{R^3}{EI} \left( B_{VH}H_A + B_{VV}V_A + B_{VM} \frac{M_A}{R} - LF_V \right)$$

$$\text{Angular rotation at } A = \psi_A = \frac{R^2}{EI} \left( B_{MH}H_A + B_{MV}V_A + B_{MM} \frac{M_A}{R} - LF_M \right)$$

where  $B_{HH} = 20c^2 + k_1(\theta - sc) - k_2 2sc$   
 $B_{HV} = B_{VH} = -2\theta sc + k_2 2s^2$   
 $B_{HM} = B_{MH} = -2\theta c + k_2 2s$   
 $B_{VV} = 2\theta s^2 + k_1(\theta + sc) - k_2 2sc$   
 $B_{VM} = B_{MV} = 2\theta s$   
 $B_{MM} = 2\theta$

and where  $LF_H$ ,  $LF_V$ , and  $LF_M$  are loading terms given below for several types of load

$$LF_H = W \left[ \frac{k_1}{2} (\theta n + \phi n - scn - s^2 m) + k_2 (m - c) \right]$$

$$LF_V = W \left[ \frac{k_1}{2} (\theta m + \phi m + scm + c^2 n) + k_2 (s + n - 2scm - 2c^2 n) \right]$$

$$LF_M = W [k_2 (1 + sn - cm)]$$

Figure 4.8: Roark's Formulas for a Concentrated Radial Load with Right End Fixed (Young & Budynas 2002)

The equivalent arch is further refined in Figure 4.9 to include relevant parameters from the modelled instrument and workpiece. Note the angle  $\phi$  of the impact point from the centre of the arch, which is required for case 5c with a radial load. In this case, the quasi-static impact point is always at the end of the arch, therefore  $\phi$  and  $\theta_R$  are equal.  $\theta_R$  is the parameter used for half the angle subtended by the arch, which is  $\theta$  in Roark's formulas (Young & Budynas 2002):



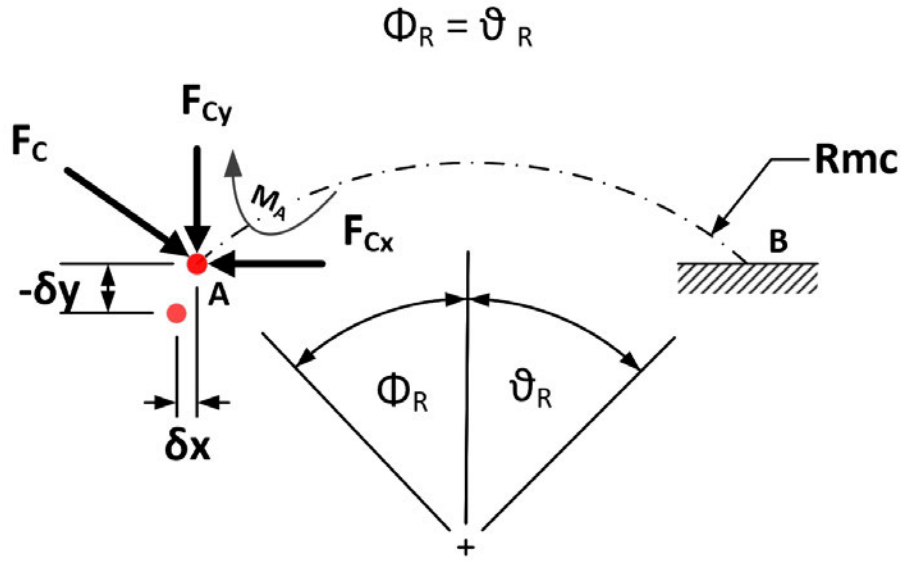


Figure 4.9: Roark's Equivalent Arch Refined in Terms of Instrument and Workpiece Parameters (Young & Budynas 2002)

Following on from the modelling of static forces over a non-deforming arch, the wheel reaction force components  $F_{C_x}$  and  $F_{C_y}$  will be used in Roark's formulas to derive horizontal and vertical load components of  $W$  and the approximated bending moment at  $A$  relative to  $B$  (positive clockwise (Young & Budynas 2002)),  $M_A$ . Therefore, with respect to Figure 4.10:

$$W = F_C \quad (4.19)$$

$$M_A = F_{C_x} A_y + F_{C_y} A_x \quad (4.20)$$

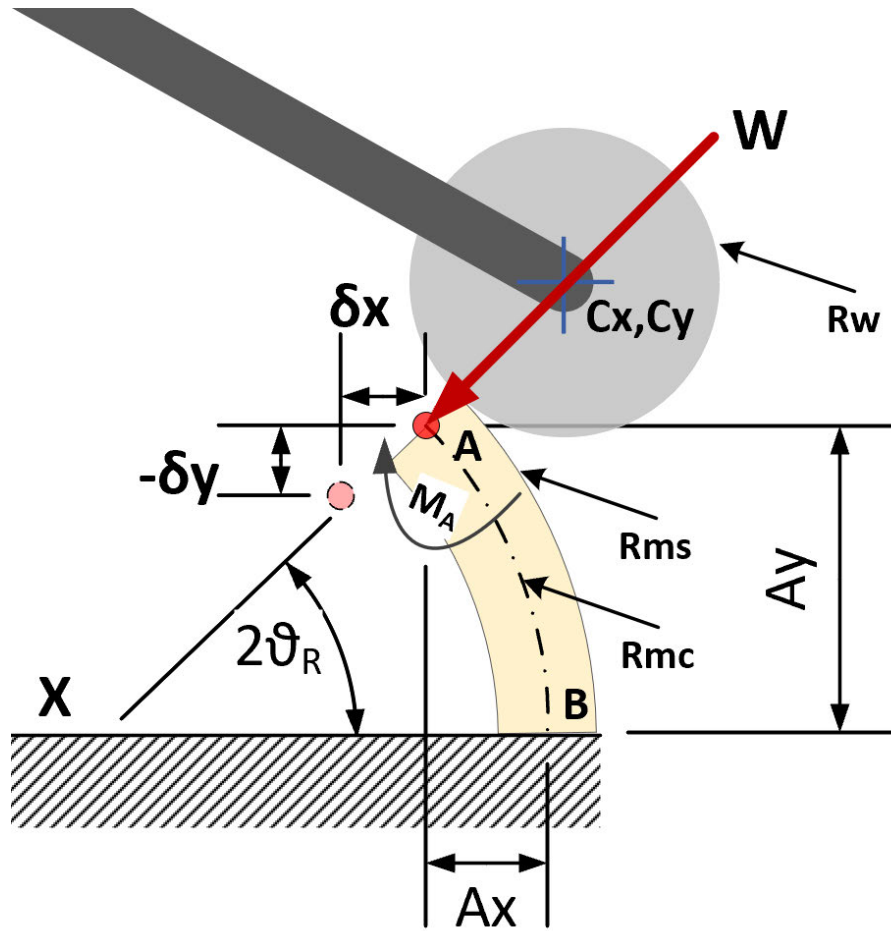


Figure 4.10: Equivalent Arch and Wheel in the Workspace

The arch is positioned with its circular centre at datum point  $X$ . The layer of fat over a beef striploin varies in thickness  $t_{fat}$  and for the purpose of this modelling the range of thicknesses specified in Khodabandehloo (2016) represent the target range for fat trimming processes to meet the expected customer requirements for high-value value beef striploin primals .

For a uniform arch, the neutral horizontal central axis radius  $Rmc$  is related to the meat surface radius  $Rms$ :

$$Rmc = Rms - \frac{t_{fat}}{2} \quad (4.21)$$

The modelled wheel axle position is known through coordinates  $C_x, C_y$ . The angle  $2\theta_R$  is

the angle defining the load point:

$$2\theta_R = \sin^{-1} \frac{C_y}{Rms + Rw} \quad (4.22)$$

The angles  $\theta$  and  $\phi$  used in Roark's formulas are:

$$\theta = \phi = \frac{2\theta_R}{2} \quad (4.23)$$

Continuing with calculating the bending moment  $M_A$  when  $\theta_R$  is known, the distances  $A_x$  and  $A_y$  are determined:

$$A_x = Rmc(1 - \cos(2\theta_R)) \quad (4.24)$$

$$A_y = \sin(2\theta_R)Rmc \quad (4.25)$$

If variables  $k_1$  and  $k_2$  are assumed to be unity, as shear and hoop-stress are not being considered, the remaining parameters required before load terms and deformation can be calculated are:

$$s = n = \sin(\theta) \text{ where } \theta = \phi \quad (4.26)$$

$$c = m = \cos(\theta) \text{ where } \theta = \phi \quad (4.27)$$

The deformation model requires loading terms  $LF_H$ ,  $LF_V$  in accordance with case 5c (Young & Budynas 2002):

$$LF_H = W \left[ \frac{k_1}{2}(\theta n + \phi n - scn - s^2 m) + k_2(m - c) \right] \quad (4.28)$$

$$LF_V = W \left[ \frac{k_1}{2}(\theta m + \phi m + scm + c^2 n) + k_2(s + n - 2scm - 2c^2 n) \right] \quad (4.29)$$

Then the equations for end  $B$  are required:

$$B_{HH} = 2\theta c^2 + K_1(\theta - sc) - k_2 2sc \quad (4.30)$$

$$B_{HV} = B_{VH} = -2\theta sc + k_2 2s^2 \quad (4.31)$$

$$B_{HM} = B_{MH} = -2\theta c + k_2 2sc \quad (4.32)$$

$$B_{VV} = 2\theta s^2 + k_1(\theta + sc) - k_2 2sc \quad (4.33)$$

$$B_{VM} = B_{MV} = 2\theta s \quad (4.34)$$

The horizontal  $H_A$  and vertical  $V_A$  load components at the wheel contact point have been established, in a horizontal direction away from point  $B$  in the positive x-axis, and a negative vertical direction in the y-axis. These forces have already been resolved for wheel contact force  $FC$ :

$$H_A = FC_x \quad (4.35)$$

$$V_A = FC_y \quad (4.36)$$

The horizontal deflection  $\delta_{HA}$  and vertical deflection  $\delta_{VA}$  can be estimated for end  $A$ :

$$\left[ B_{HH}H_A + B_{HV}V_A + B_{HM}\frac{M_A}{R} - LF_H \right] \quad (4.37)$$

$$\left[ B_{VH}H_A + B_{VV}V_A + B_{VM}\frac{M_A}{R} - LF_V \right] \quad (4.38)$$

The deflection equations 4.37 and 4.38 require constants to be defined for elasticity modulus  $E$  of a chilled beef fat tissue, and moment area of inertia  $I$ :

$$E = \text{Young's Modulus} \approx 15\text{MPa} \quad (4.39)$$

$$I = \frac{\text{Width}_{\text{wheel}} \cdot t_{\text{fat}}^3}{12} \quad (4.40)$$

where the width of the wheel is assumed to be the width of the arch.

The static, elastic deformation of the circular- arch (Roark's) modelling is a simplification of the expected deformation characteristics for a beef workpiece. However, the fat layer is expected to be significantly stiffer than the meat underneath and the evidence suggests that isotropic, cellular structure of the fat tissue could potentially deform in a predictable way under the force of the wheel. A value of 15MPa for fat tissue elastic modulus has been applied in the model. Compression tests (Comley & Fleck 2012) on fresh fat tissue from pigs produced results that indicate this value is higher than moduli results recorded ( $\approx 1\text{MPa}$ ). This value was measured when the fat tissue samples were compressed at a high strain rate, where fat tissue exhibits a 'lock-up' condition and the maximum stiffness. Discussions with USQ CAE researchers confirm that beef striploin fat layers are stiffer than the meat underneath however testing has not been possible within the scope of this project. Therefore, for the purpose of initialising a system model, the value of 15MPa is considered a reasonable value for high-stiffness fat tissue. This value produces results that are reasonable expected deformations, where the thinnest 4mm theoretical fat layer is deformed to the elevation approximately equal to the point where the wheel addresses the workpiece, see Figure 4.11:

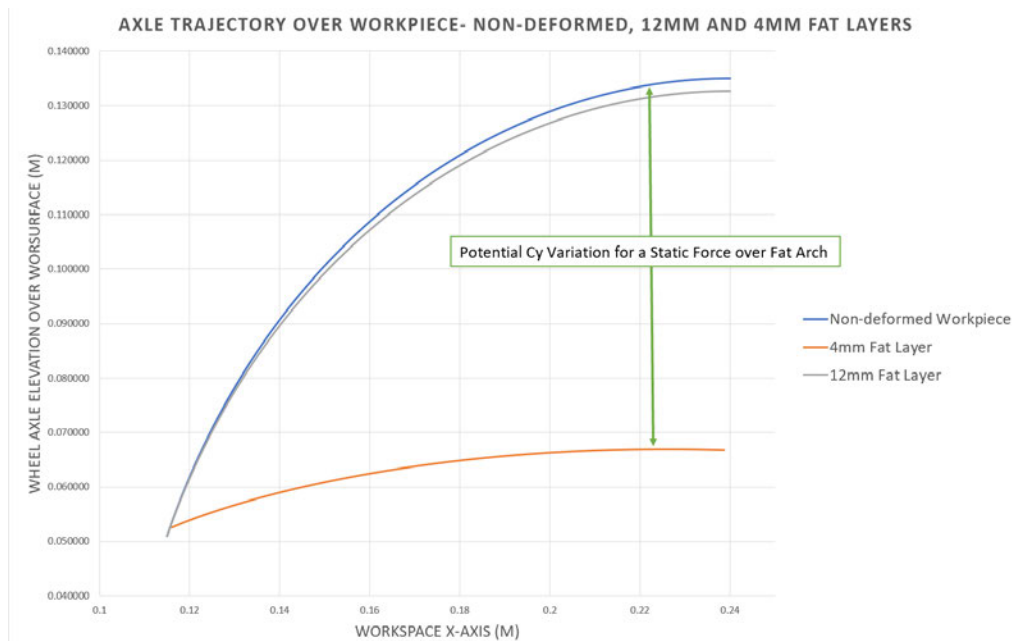


Figure 4.11: Static Deformation Results - Wheel Elevation  $C_y$  for Non-Deforming Surface, 12mm and 4mm Thick Fat Layers

Roark's formulas are not suitable for dynamic load analysis (Young & Budynas 2002), however the modelled deflection for a static load is considered to be the potential for deformation of the fat layer at any point on the surface; relative to the initial spring compression force being applied at that point.

The instrument constrains the amount of x-axis and y-axis deformation possible, as the trailing arm pivots around point A. The static deformation modelling assumes that all x and y deformation components are possible. The prototype instrument kinematics would not allow the wheel follow the modelled deformation vector trajectory unless the position and speed of the wheel was governed by the surface-layer deformation characteristics (among other simplifying assumptions).

The magnitude of deformation is likely to be influenced by the viscoelastic characteristics of the meat underneath and the velocity of the wheel over the surface. The meat sub-layer should yield as the fat layer deforms, and the spring-damper effects of the viscoelastic muscle tissue should modulate the potential static deformation, relative to the rate of deformation. The system model is explained further in the following section, where these viscoelastic effects and the operation of the instrument itself are characterised in a quasi-static adaptation of the static deformation model.

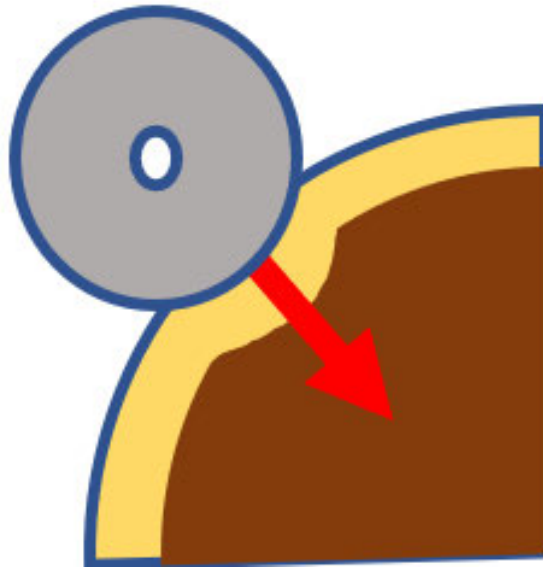


Figure 4.12: Simplified Static Elastic Deformation of the fat Layer

As the static deformation prediction is also elastic, the contact-surface area under the wheel can be determined and an approximation of deformation stress can be calculated from the system model results.

The system model is based on viscoelastic spring-damper constants from the research (Moreira et al. 2014), produced with a 6mm diameter indenter for a series of 10mm indentations. The area under the 6mm indenter is  $2.83e^{-5}m^2$ , therefore for a reported average peak force of 2.75Nm the deformation stress is approximated to 97kPa.

The final application of the circular segment formulas (Weisstein 2020) is the approximation of elastic deformation stress under the wheel, using results of the system model. This will provide a check on the validity of the wheel radius chosen for the prototype instrument. The static force (Roark's) model and the system model are not sensitive to the wheel radius parameter, as the forces are approximated as a point source. Only the wheel width is used, for the cross sectional area of the fat layer under the wheel, which changes the bending moment quite considerably for a fixed value of Young's modulus over the range of fat thicknesses used.

### 4.3 System Model

The system model in Figure 4.13 is a quasi-static characterisation of the modelled fat-layer deformation coupled with a compressing meat layer exhibiting time-varying deformation in accordance with a Kelvin-Voigt viscoelastic model (Figure 4.14). The second-order approximation of a spring-damper system gives an approximated time-response of the fat-layer deformation from the static model.

The feedback loop is also important, as the operation of the instrument influences the amount of force applied at the surface. The basic concept of the feedback loop is a time-stepped relaxation of the spring force proportional to the change in surface-deformation/wheel elevation.

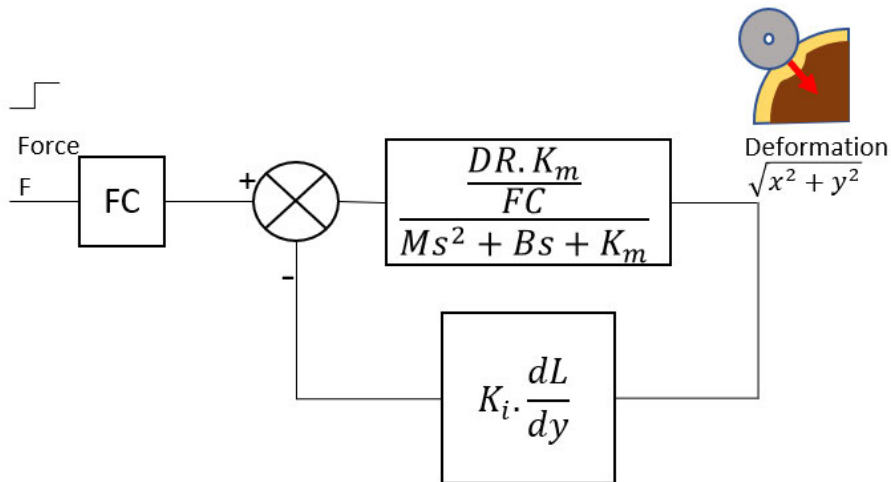


Figure 4.13: System Model - Tactile Sensing Instrument and Beef Striploin Workpiece

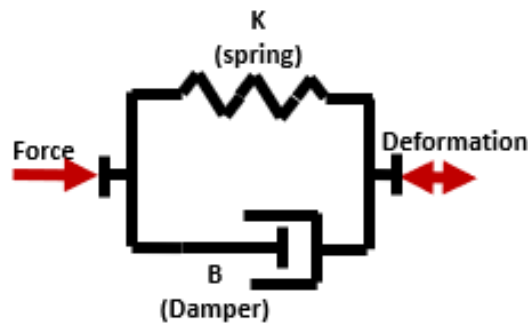


Figure 4.14: Kelvin-Voigt Viscoelastic Model

The unit-step input is multiplied by the surface force  $F_C$ , determined at each point of



the surface of the non-deforming arch in Section 4.1.3. This step input is cascaded with an approximated second-order viscoelastic model for wheel in contact with beef striploin. The basic viscoelastic model in the 's' domain is:

$$Deformation = \frac{1}{Ms^2 + Bs + K_m} \quad (4.41)$$

where  $M$  is the instrument mass,  $B$  is the viscosity constant for beef, in this case 14.7, as reported by Moreira et al. (2014) in their Kelvin-Voigt viscoelastic modelling experimentation with beef samples, and  $K_m$  is the spring constant for meat, again reported by Moreira et al. (2014) with a value of 192.7.

A gain factor of  $\frac{DR.K_m}{F_C}$  has been applied, based on the assumption that if the open loop system continued over time with a constant force  $F_C$ , the resulting deformation would equal  $DR$  which is the static (Roark's) model deformation at each 1mm point over the arch.

Finally the feedback loop, which applies negative feedback to the applied force proportional to the amount of y-axis deflection experienced at the wheel  $dy$ . The variation in spring length  $dL$  multiplied by instrument spring constant  $K_i$  reduces the applied force over the time period that the deflection is occurring.

For a closed-loop system comprising an open-loop transfer function of  $G(s)$  with negative feedback  $H(s)$ , the closed-loop transfer function  $T(s)$  is (Nise 2008):

$$T(s) = \frac{G(s)}{1 + G(s).H(s)} \quad (4.42)$$

Following algebraic simplification, the natural frequency  $\omega_n$  and the damping factor  $\zeta$  have been calculated, to determine whether the time-response at each time step is under-/over/critically damped and the appropriate second-order time response function applied to the model output (Nise 2008). The MATLAB code for the models and time-domain functions is provided in Appendix C.

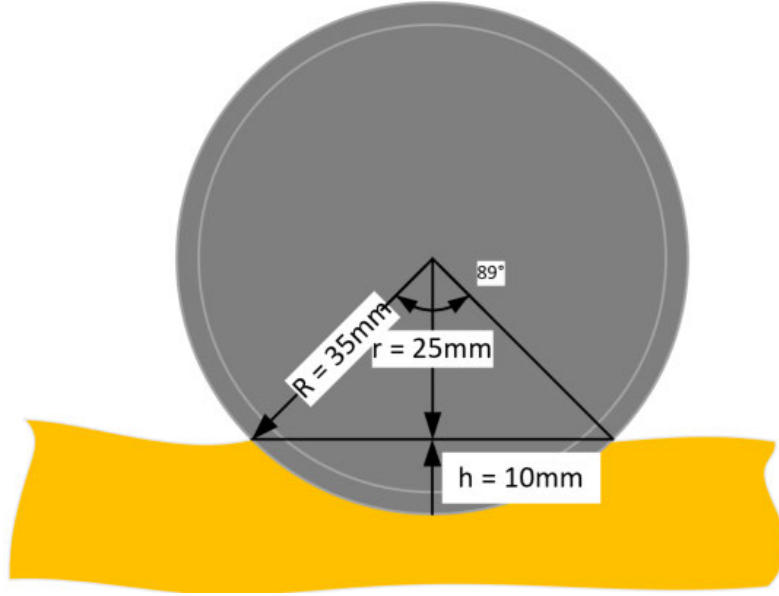


Figure 4.15: 35mm Wheel Deforming the Surface 10mm

When the results of the prototype instrument system model are available, the deformation stress under the 35mm wheel at 10mm deformation can be approximated. Using the formulas for a circular segment (Weisstein 2020), the angle  $\theta$  in Figure for a 35mm wheel deforming the surface by 10mm is:

$$\theta = 2(\cos^{-1} \frac{r}{R}) = 2(\cos^{-1} \frac{0.25}{0.35}) = 1.55\text{rad} \quad (4.43)$$

The contact surface area  $SA$  of the wheel of width  $Ww$  is:

$$SA_{wheel35} = \pi D.Ww = \pi.0.07.0.01 = 2.20e^{-3}m^2 \quad (4.44)$$

The area under deformation is approximately one-quarter of the total surface area, given the angle of the segment is  $\approx 90^\circ$

$$SA_{contact} = 0.25(2.2e^{-3}) = 5.5e^{-4}m^2 \quad (4.45)$$

Therefore, once the force applied for 10mm deformation is determined from the results, the deformation stress produced by the prototype wheel of 35mm radius can be estimated and the decision to use the 35mm radius wheel assessed for reasonableness.

# Chapter 5

## Results

### 5.1 Prototype Instrument Modelling

The physical build of the instrument was modelled in a computer drawing package, to verify the application of the system design specifications in the Bill of Materials (BOM) software tools. The instrument dimensions originate from the decision to use a certain wheel radius, axle bore and a maximum radius of representative striploin arch structure. The tool-support elevation of the test rig is also a design decision, setting the instrument pre-load state to ensure the sensing-mode spring compression requirements are within spring manufacturer's specifications. The most difficult part of the design to achieve was the allocation of a position along the trailing arm to mount the spring mechanism. Figure 5.1 shows how the compression ratio estimates for a particular wheel radius, tool-support elevation and meat-arch radius vary from 100 % compression to around 58% at regions towards the wheel-end of the arm. The verification is provided in Figure 5.2, which is a scale drawing of the prototype instrument with the computer drawing package dimensioning tool indicating an approximation of the preload and maximum elevation sensing state spring lengths, which comply with the manufacturer's specifications of 70mm free length and a 75% compression ratio.

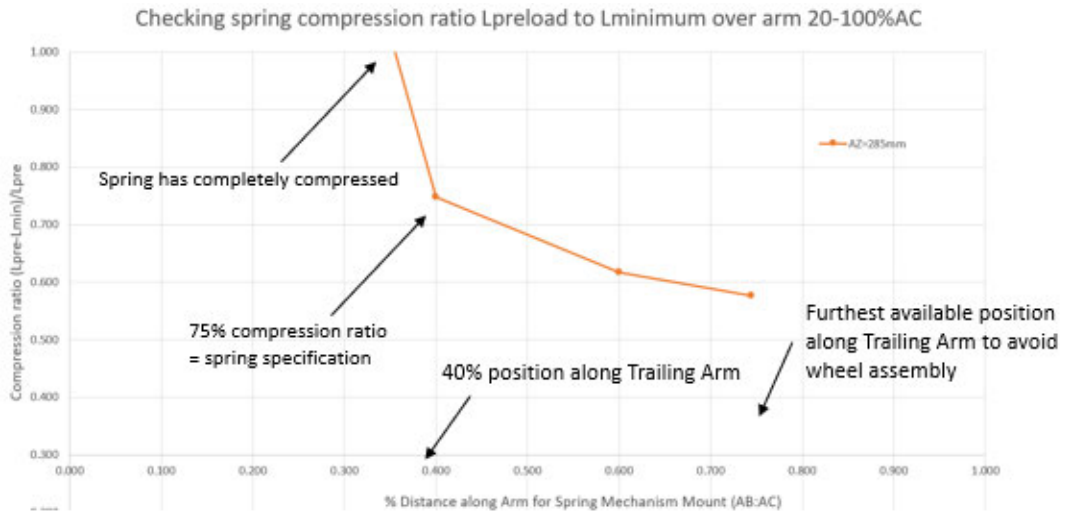


Figure 5.1: Spring Compression Ratio over the Length of the Trailing Arm

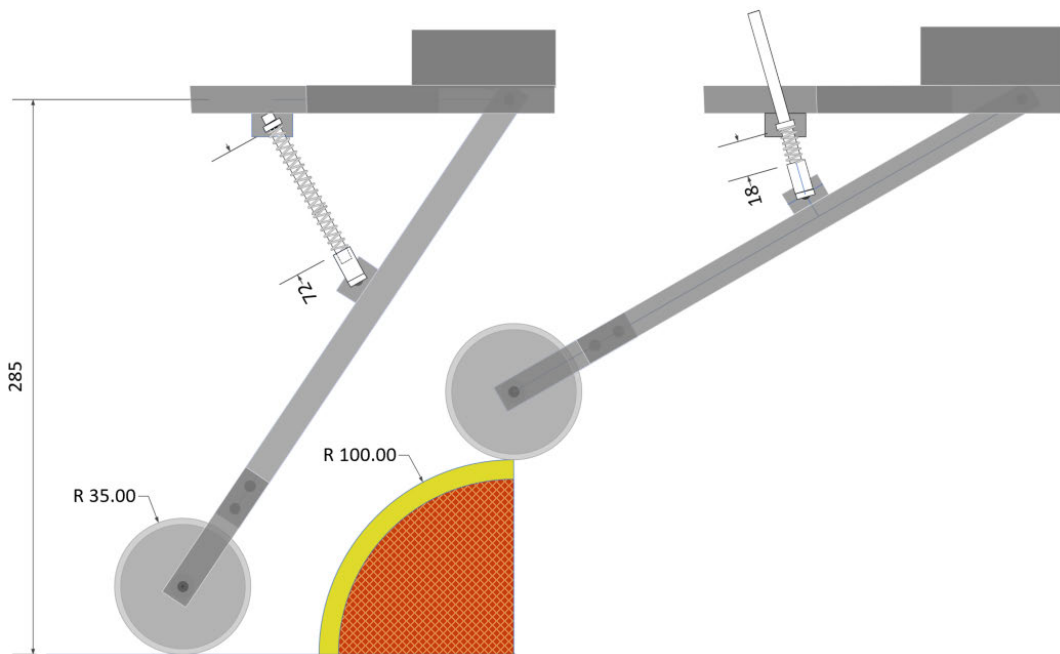


Figure 5.2: Drawing Package Dimensions to Verify Spring Compression Range

## 5.2 Static Force Modelling

Deformation modelling is based on a wheel reaction force profile modelled over a non-deforming arch. Figure 5.3 shows the forces assumed to be the maximum wheel reaction force available at 1mm intervals over the workspace.

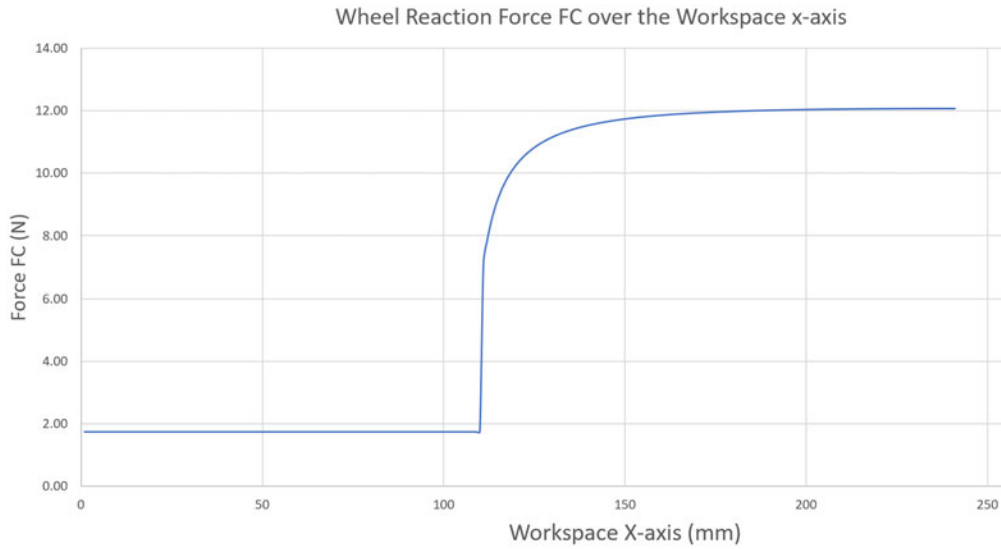


Figure 5.3: Wheel Reaction Force over the Workspace

The force is constant at instrument weight  $F_M$  until the wheel mounts the workpiece, after which the x and y components of the spring force act radially on the arch over the surface. There is a relatively low variation in force over much of the wheel track over the workpiece. The 35mm rad. wheel contacts the 100mm rad. arch when the axle is  $\approx$  110mm along the x-axis.

The static deformation model (Roark's) produced a deformed-surface profile for a range of fat thicknesses subjected to the applied force conditions shown in Figure 5.3 above. The fat thicknesses considered were 4 and 12mm, which are the recommended thicknesses for an automated trimming operation to add value to beef striploin processing (Khodabandehloo 2016), and 20, 30 and 50mm for the purpose of providing a range of thicknesses similar to those measured by Border et al. (2019).

An example of the magnitude of potential deformation under a static force load condition is illustrated in Figure 5.4. This example shows the wheel axle position (blue) when positioned over the non-deforming arch and the axle position over a 12mm (grey) and 4mm (orange) thick arch. The plots originate slightly past the 110mm x-axis position where the wheel-tissue contact has commenced and the y-axis deformations are in the negative (down) direction. The region around the contact point is not considered within the modelling due to inconsistent results across the different arch thicknesses.

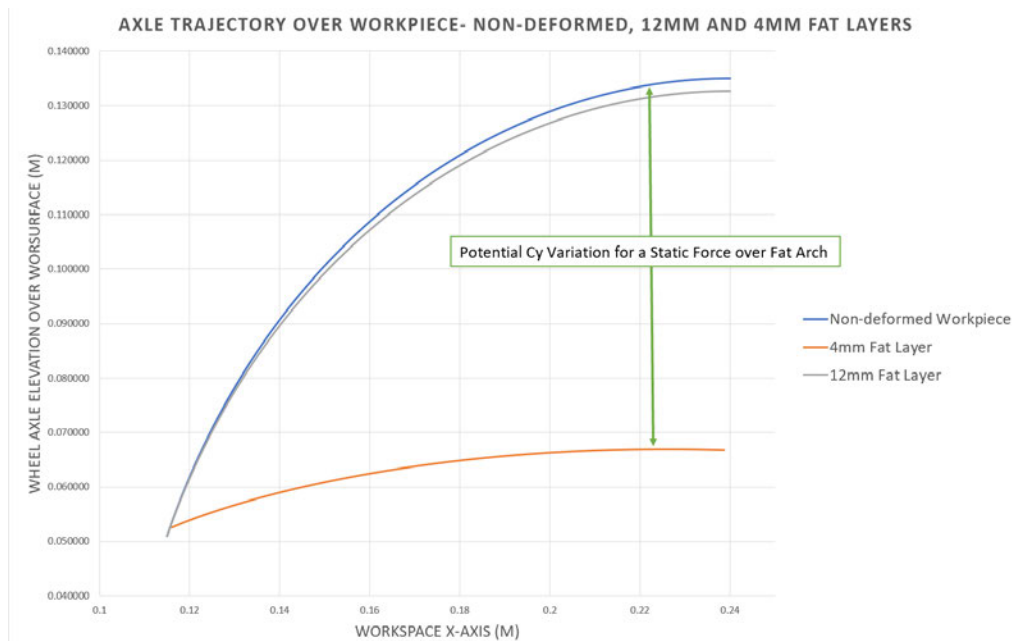


Figure 5.4: Static Deformation Results - Wheel Elevation  $C_y$  for Non-Deforming Surface, 12mm and 4mm Thick Fat Layers

### 5.3 Quasi-Steady System Modelling

The system model produces plots of the viscoelastic deformation time-response as well as predictions of the depth of deformation from quasi-static placement of the wheel over the workpiece with 4, 12, 20, 30 and 50mm thick fat layers.

The plot in Figure 5.5 is the second-order time response of deformation with a 4mm fat layer coupled with the viscoelastic model for the meat underneath. The simulation runs for 1 second, with the workpiece and wheel from the prototype instrument model overlaid to provide a reference to the approximate position on the surface to which the deformation responses relate. The upper portion of the workpiece produces results that are more tightly grouped and exhibit an under-damped response. This region is also where the applied force was shown to be approximately constant in Figure 5.3.

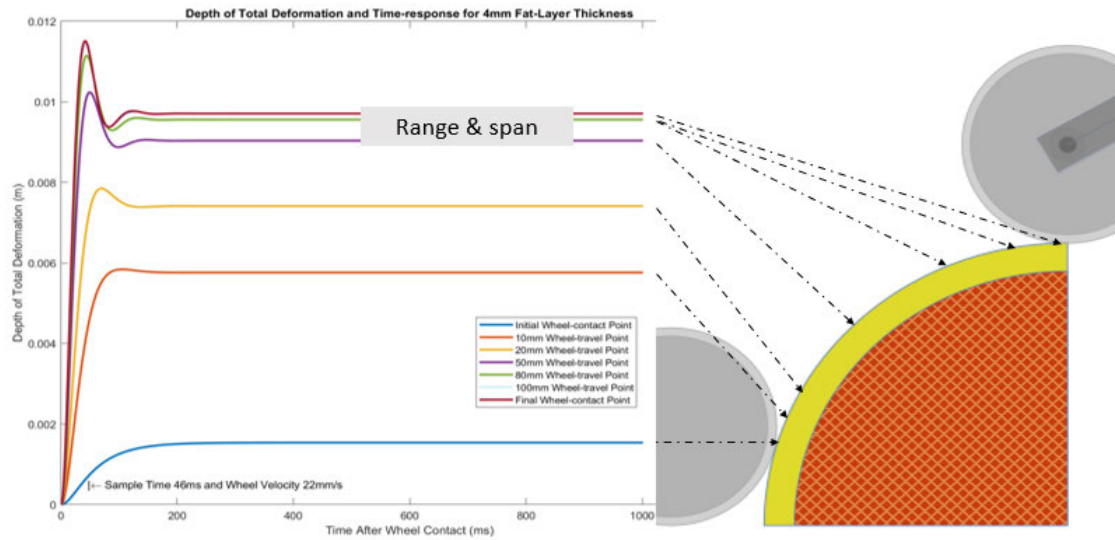


Figure 5.5: Quasi-static Deformation Time Response - 4mm Fat Layer over Viscoelastic Workpiece

The time for peak deformation at each test-point over the workpiece (Figure 5.5) has also been determined and averaged to estimate a sampling rate and wheel velocity synchronised with the average peak deformation. In Figure 5.5 the result of peak-deformation sampling time estimate was 46ms, with a corresponding velocity of the wheel of 22mm/s assumed to be representative of the dwell-time required at each 1mm test point to achieve maximum deformation.

The time responses for each thickness of fat layer (4 to 50mm) have been sampled at the average peak time for all fat layer thicknesses over the portion of the surface 50mm from initial contact to the end (top 4 points in Figure 5.5). The resulting deformation plot in Figure 5.6 is oriented with zero along the upper x-axis and deformation increasing in the downward y-axis direction. The results show that the thinnest fat layer (4mm) produces a maximum deformation of  $\approx 10\text{mm}$ , while a 12mm or thicker layer exhibits less than 1mm deformation.

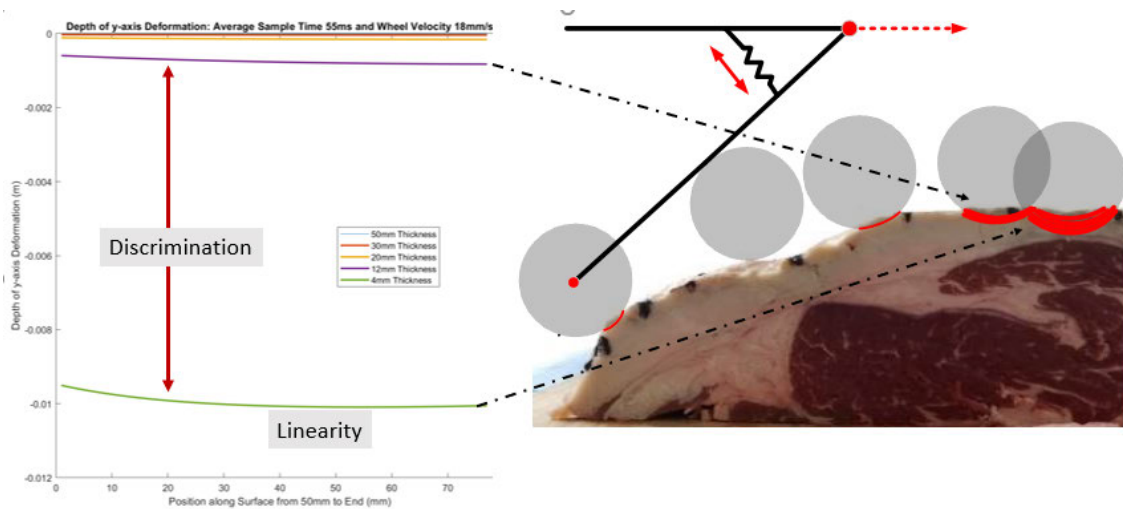


Figure 5.6: Deformation of Different Fat Layer Thickness at Average Peak Sampling Time

## 5.4 Design Parameter Sizing

### 5.4.1 Workpiece-Trailing Arm Clearance (gap)

The prototype trailing arm design, based largely on wheel, workpiece and test rig elevation dimensions, established a clearance *gap* from the workpiece surface and the trailing arm at the point of wheel-tissue contact. The initial contact point is considered to be the worst case for arm-workpiece contact, and the arm is less exposed to the surface of the meat as the wheel is moved up the arch (see Figure 5.7).



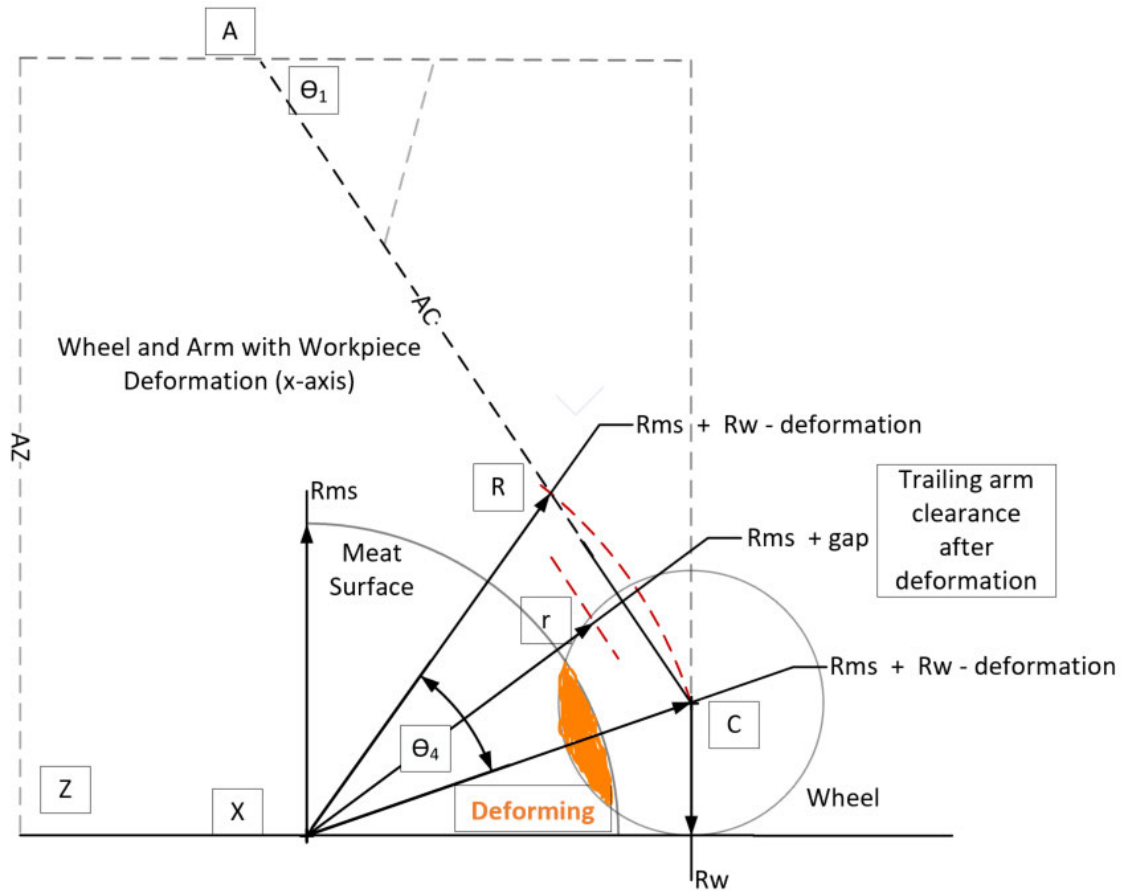


Figure 5.7: Wheel-tissue Interactions with Modelled Trailing arm and Wheel Mechanism for Deforming Workpiece

With prototype dimensions established, the clearance at the closest point between the arm and surface is calculated with the circular segment formula for the radial distance  $r$  to the chord (Weisstein 2020). The maximum deformation estimate from system modelling results has been entered into the design calculations of the BOM model (Figure C.1 in App.C) and the *gap* between the workpiece and arm after 10mm deformation is  $\approx 11\text{mm}$ .

#### 5.4.2 Test Rig Towing Force

The maximum x-axis force produced at the wheel-tissue interface ( $F_{Cx}$ ) has been estimated using the static force model for a non-deforming arch. This is the maximum force applied to maintain an static equilibrium position for the wheel over the arch, relative to the spring force and weight force applied to the workpiece by the mechanism, illustrated in Figure 5.8:

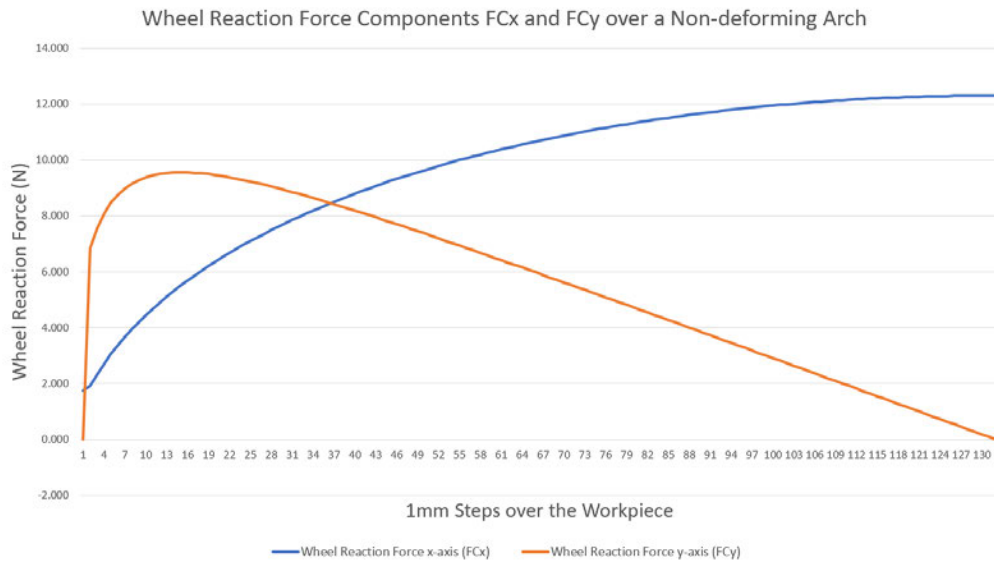


Figure 5.8: Wheel Reaction Force x-axis and y-axis Components over the Workpiece

The estimate of test rig x-axis towing force has been determined for a static equilibrium conditions over the non-deforming arch, by extracting the contributions of the spring x-axis forces from the total wheel reaction force estimations:

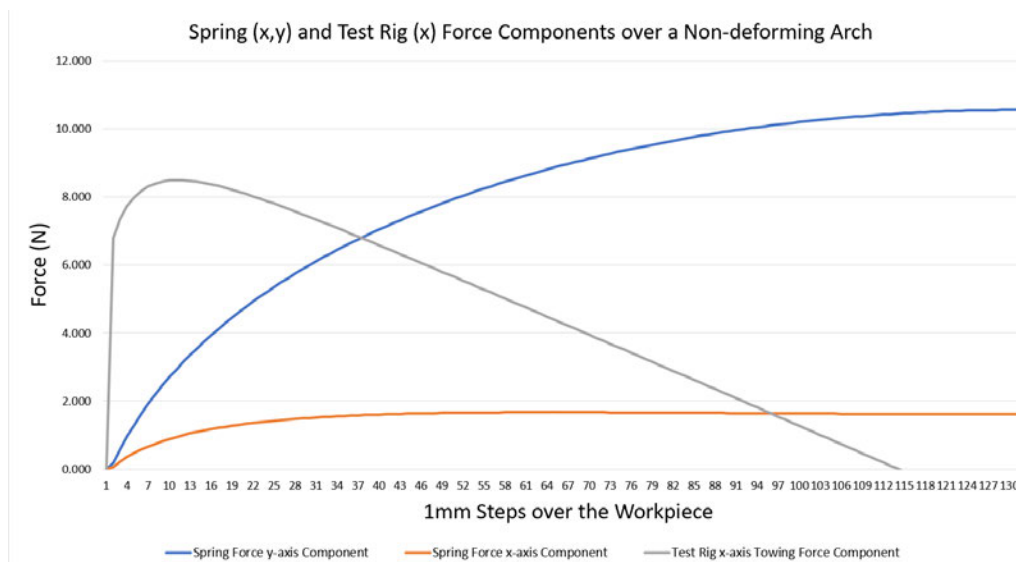


Figure 5.9: Spring and Test Rig Force Contributions for Static Equilibrium

### 5.4.3 Wheel Dimensions

It is important to note that the system model, like the static force model, is not sensitive to wheel radius, as the forces are considered to be concentrated at a point. This is one of the conditions of Roark's formulas for stress and strain over an arched structure (Young & Budynas 2002).

The wheel width however, has contributed to the force modelling through the use of this parameter in the static deformation of the arch structure. The arch deformation formulas (Young & Budynas 2002) apply the width of the wheel in determining the cross-sectional area of the arch, for use in determining the moment of inertia and a bending moment at each end when a concentrated radial force is applied.

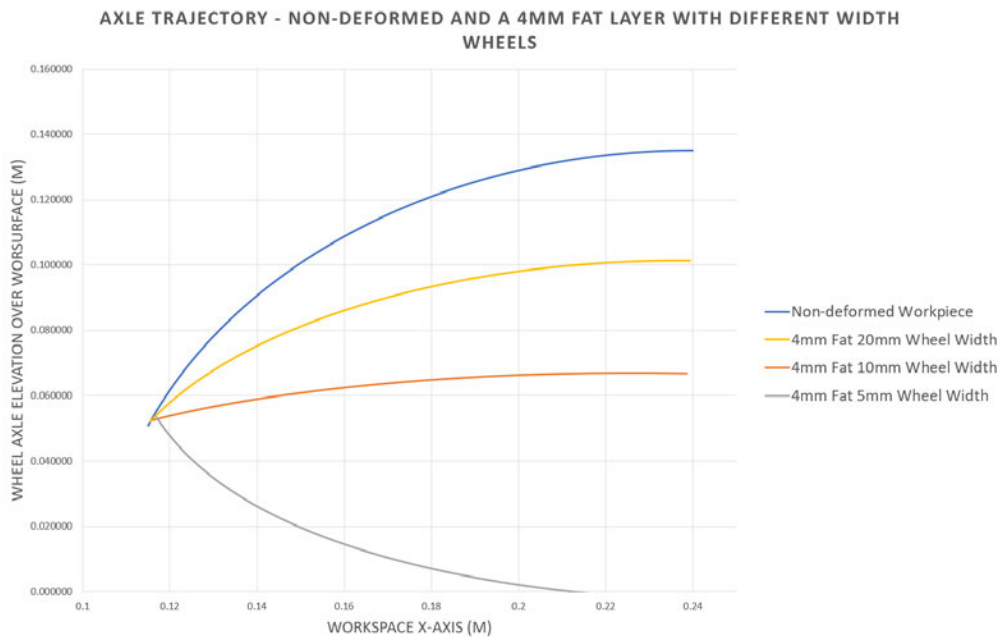


Figure 5.10: Wheel Width Variations and Effect on Deformation Predictions

The predicted static deformation is sensitive to wheel width, as illustrated in Figure 5.10. For a 4mm thick fat layer, a doubling in wheel width produces around half the expected deformation. While halving the wheel width produces deformation predictions beyond the physical range of the workspace.

Finally, the decision to use a 35mm wheel can be assessed in terms of the predicted local deformation stress under the wheel in a static elastic deformation condition.

1. Force applied for 10mm deformation  $\approx 12.3N$
2. Contact surface area for 35mm radius wheel  $\approx 5.5e^{-4}$
3. Local deformation stress  $\approx 23kPa$

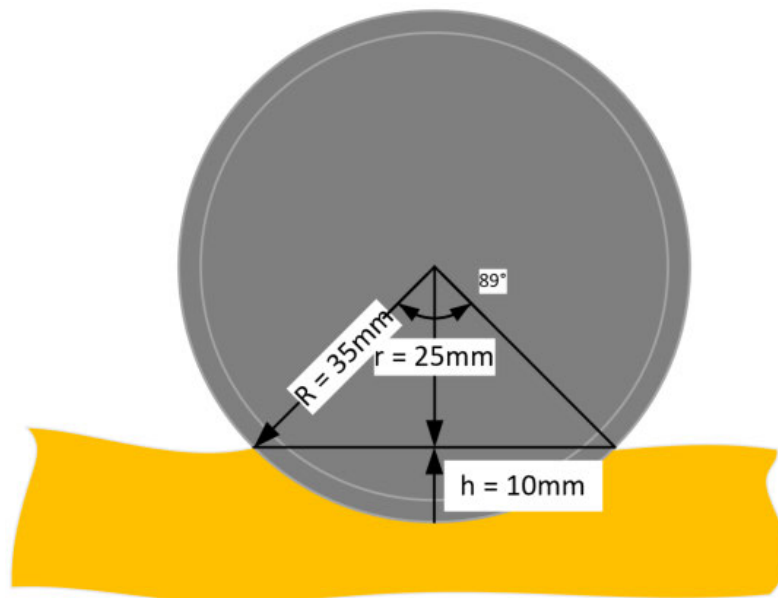


Figure 5.11: 35mm Wheel Deforming the Surface 10mm

Local deformation stress under the wheel has been estimated for a range of wheel radii. 20mm radius is a reasonable minimum size for 10mm deformation, as only 10mm remains for clearance between the meat surface and hub/arm attachment. A 50mm radius wheel is the same height as the workpiece and a reasonable maximum wheel size.

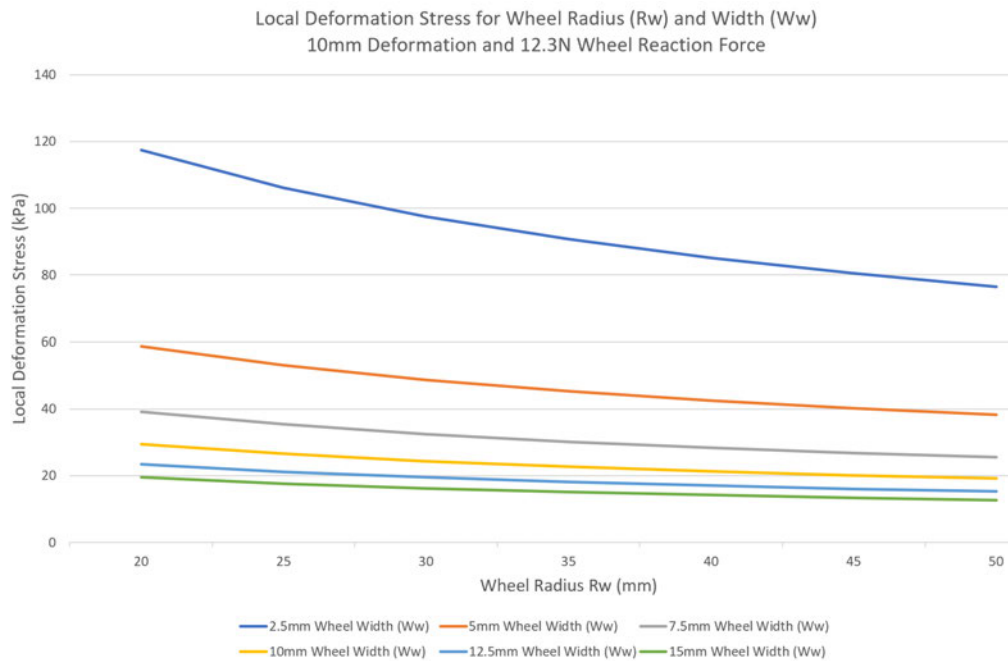


Figure 5.12: Local Deformation Stress Under Different Wheel Dimensions

Figure 5.12 suggests that the radius has a small effect on deformation stress while narrow wheels ( $\approx 2.5\text{mm}$ ) increase the level to that reported in the literature, across the range of wheel radii considered.

## Chapter 6

# Discussion and Design Review

The results produced in the performance models are reviewed in terms of the predicted wheel-tissue interactions between the instrument and the workpiece and the key design parameters that influenced the results.

### 6.1 Modelled Instrument Performance

The modelled instrument responses to wheel-tissue interactions comprise the static elastic deformation of the surface fat layer and the viscoelastic response of the beef sub-layer, which are generally characterised by the:

1. magnitude and direction of deformation at the surface, influenced by the fat thickness, wheel width and spring force loading profile
2. magnitude and rate of viscoelastic beef tissue response to the step-change in applied force.

Importantly, all predicted instrument responses are based on estimations of beef and fat mechanical properties. Future experimental work is required to validate these parameters before the results of modelling can be used as a reference for the prototype instrument.

The predicted deformation across the selected range of fat thicknesses (Figure 5.5), suggest that the instrument span could exclude the lower section of the workpiece where wheel-

contact is initiated. The response becomes more consistent and under damped once the wheel travels  $\approx 50\text{mm}$  along the surface. Increasing the preload spring force might improve the initial response but would cause the instrument to lose sensitivity at higher elevations as the instrument spring constant would not be matched to that of the beef.

The rate of deformation has been analysed to determine a preliminary estimate of average peak time, which would be used in a sampling algorithm to capture peak trailing arm deflections as required to interface with transducer specifications and improve discrimination between fat thicknesses. Dynamic instrument characterisation would also require analysis of the peak time when establishing an optimum wheel travel speed.

Fat thickness discrimination, the key aim of the instrument design, is demonstrated in the preliminary system model results in Figure 5.6. The estimated parameters for meat and fat in the deformation models have produced up to 10mm deflection of the wheel at the surface, with fat thicknesses over the target range of 4 - 12mm. This result is not a formal verification of the instrument specification, rather an observation that the modelling is sensitive to the key parameters. The proposed optimum operating range of 50mm beyond initial wheel-tissue contact is also shown to produce a reasonably linear output for increasing elevation and applied spring force.

The instrument geometry (Figure 5.7), designed to maintain clearance between the arm and workpiece as the instrument contacts and deforms the workpiece, is shown to be effective up to the maximum predicted deformation of  $\approx 10\text{mm}$ .

The basic test rig towing force requirements to overcome spring force and weight provide over 50% margin for maximum available towing force (Figure 5.9). This is assumed to be adequate to account for the wheel rolling friction and 'bogging-down' in the deforming surface.

The decision to use a 35mm radius wheel is assessed in terms of the static elastic deformation stress under a symmetrically displaced contact surface under the wheel. These are the conditions for which the experimental derivation of spring and damper constants for the meat are carried out, using the methods of Moreira et al. (2012). The results indicate however, that the stress produced by a 35mm radius 10mm wide wheel is around half that applied in the literature. The effect of reducing the wheel width to 5mm suggests that a comparable level of stress is achievable, with the radius also shown to have little effect

on altering the local deformation stress (Figure 5.12). However, the static deformation model output varies considerably with a reduction in cross sectional area of fat (Figure 5.10), therefore an analytical approach will be required to derive an optimum wheel size, once experiments provide a reasonable characterisation of beef striploin.

Finally, the dynamic wheel-tissue interaction results reported by Rentschler et al. (2006) offer an insight into how the contact surface area under the wheel may also reduce due to the tendency for viscoelastic rolling contact to concentrate the reaction forces towards the front half of the wheel (Figure 6.1).

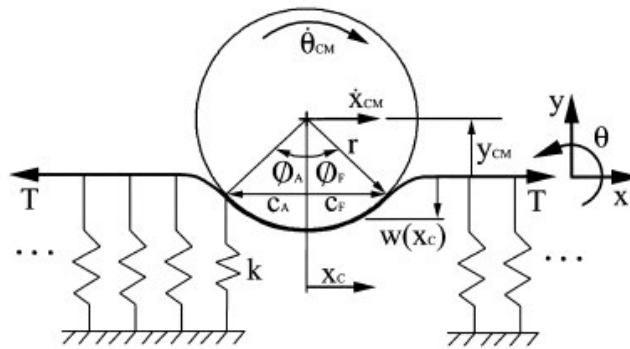


Fig. 4. Elastic tissue model where  $k$  is the tissue stiffness.

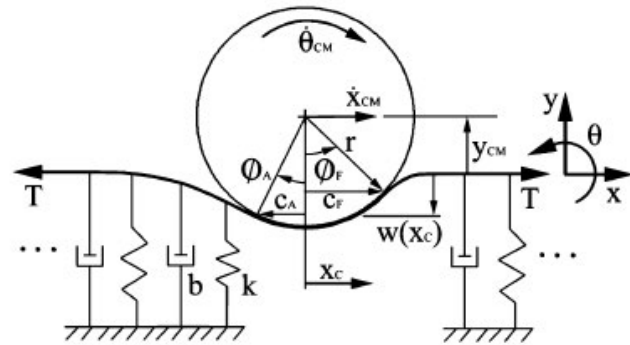


Fig. 5. Viscoelastic model, where  $k$  is the tissue stiffness and  $b$  is the viscous damping of the tissue.

Figure 6.1: Comparison of Wheel-tissue Contact for Viscoelastic and Elastic Materials (Rentschler et al. 2006)



## 6.2 Key Parameters: Instrument and Workpiece

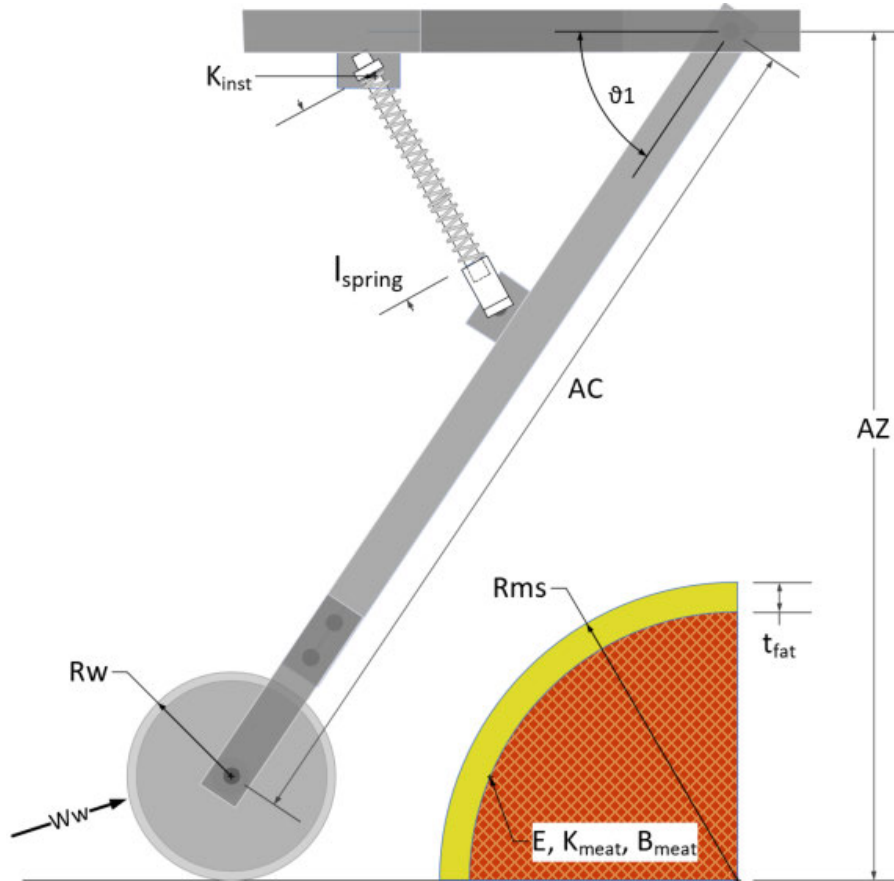


Figure 6.2: Key Design Parameters - Tactile Sensing Instrument and Workspace

Table 6.1: Key Design Parameters

Parameter	Definition	Significance & Impacts
$R_w$	Wheel radius	<ul style="list-style-type: none"> <li>• Determines the arm length and angle</li> <li>• Larger wheel = more clearance between arm and workpiece</li> <li>• Parameter not applied in static deformation or system modelling</li> <li>• Small effect on local deformation stress</li> <li>• Experimental calibration including indentation testing with wheel could help determine relationship between radius and viscoelastic spring-damper parameters of workpiece used in system modelling</li> </ul>

Parameter	Definition	Significance & Impacts
Ww	Wheel width	<ul style="list-style-type: none"> <li>• Significant parameter in static arch-deformation model</li> <li>• Bending moment determined by arch cross-section, based on Ww</li> <li>• Narrow wheel increases local deformation stress</li> <li>• Need to avoid cutting the surface with too-narrow wheel</li> <li>• Contact surface area may reduce to forward-lower quadrant, during dynamic rolling over the surface (Rentschler et al. 2006), potentially increasing local deformation stress</li> </ul>
AZ	Arm pivot elevation	<ul style="list-style-type: none"> <li>• Constrained by test rig tool attachment adjustment limits</li> <li>• Expected meat workpiece variations require an appropriate elevation setting, optimising operating range of instrument mechanism</li> <li>• Combines with wheel radius <math>Rw</math> to establish trailing arm length</li> <li>• Limits the range of potential spring lengths</li> </ul>
AC	Trailing arm length	<ul style="list-style-type: none"> <li>• Maximum length constrained by <math>Rw</math> and workpiece clearance</li> <li>• Minimum length constrained by spring mounting mechanics</li> <li>• Key parameter relating wheel elevation, tool attachment elevation <math>AZ</math> and angle <math>\theta_1</math></li> </ul>
$\theta_1$	Trailing arm angle	<ul style="list-style-type: none"> <li>• Proportional to wheel elevation</li> <li>• Potential measurement point; used to discriminate variations in wheel-tissue interactions</li> <li>• If the prototype instrument operated in accordance with results, only 1mm surface deflection would be expected for the upper target fat thickness of 12mm. Only 10mm deformation would be expected for 4mm fat thickness, a variation in <math>\theta_1</math> of <math>\approx 2.5^\circ</math></li> <li>• A high-resolution rotary encoder may be a suitable transducer</li> </ul>
$l_{spring}$	Instrument spring length	<ul style="list-style-type: none"> <li>• Manufacturer determines free-length, solid-length and maximum recommended compression, spring constant</li> <li>• Trailing arm range of travel <math>\Delta\theta_1</math> and position along arm to mount spring mechanism, determines applicability of spring</li> <li>• Spring length varies non-linearly with <math>\theta_1</math>, but compresses <math>\approx</math> half the increase in wheel elevation</li> <li>• Free-length matched to space within mechanism at preload state</li> </ul>

Parameter	Definition	Significance & Impacts
$K_{inst}$	Instrument spring constant	<ul style="list-style-type: none"> <li>• Spring constant matched to modelled workpiece spring constant <math>K_{meat}</math> to optimise instrument sensitivity (impedance match)</li> <li>• System model feedback based on <math>K_{inst}</math> and <math>\Delta l_{spring}</math></li> <li>• Trailing arm stiffness and other assembled component rigidity assumed to be significant (completely rigid)</li> <li>• Two springs are fitted, to increase options for adjusting the parameter</li> <li>• Rods prevent buckling of springs, compensating for the high slenderness ratio. Friction is assumed to be negligible</li> </ul>
Rms	Workpiece arch radius	<ul style="list-style-type: none"> <li>• Contributes to the estimate of maximum wheel-contact force and minimum length of <math>l_{spring}</math></li> <li>• Static deformation modelling calculates the arch centroid radius from Rms and <math>t_{fat}</math></li> <li>• Results indicate that the instrument results are more consistent beyond <math>\cong 50mm</math> travel over the 100mm Rms arch. A significantly smaller arch may not adequately contribute to spring compression to produce deformation that the prototype instrument could detect.</li> </ul>
$t_{fat}$	Fat layer arch thickness	<ul style="list-style-type: none"> <li>• Key parameter for static deformation modelling, to calculate centroid radius, moment of inertia and bending moment when combined with <math>Ww</math> and <math>E</math></li> <li>• Research suggests that 4-12mm is the target for automated trimming (Khodabandehloo 2016)</li> <li>• Target range displayed good discrimination results <math>\cong 10mm</math> deflection, although strongly related to <math>E</math></li> <li>• Above 12mm <math>t_{fat}</math> potentially difficult to detect at modelled value of <math>E</math>.</li> </ul>

Parameter	Definition	Significance & Impacts
E	Young's modulus (fat)	<ul style="list-style-type: none"> <li>• Static deformation model is designed for engineering materials such as steel and concrete (Young &amp; Budynas 2002)</li> <li>• Young's modulus <math>E</math> of fat is difficult to estimate without experimentation</li> <li>• The <math>E = 15MPa</math> estimate was chosen to keep modelled 4mm arch-surface deflection approximately horizontal to the x-axis. This value is also within an order of magnitude of test results in the literature (Comley &amp; Fleck 2012).</li> <li>• <math>E</math>, once known, would be influenced by the temperature of the experimentation environment, which also makes this parameter controllable</li> </ul>
$B_{meat}$	Viscosity (damper) constant (meat)	<ul style="list-style-type: none"> <li>• Parameter chosen from beef experiments in literature (Moreira et al. 2014)</li> <li>• Experimental calibration using a prototype wheel could support re-definition of this parameter for beef striploin</li> <li>• Significant attenuation of the modelled static deformation occurs due to application of this property in the system model</li> <li>• The Kelvin-Voigt model using this parameter, could be assessed for suitability and possible replacement with a more complex model, following experimental calibration</li> </ul>
$K_{meat}$	Spring constant (meat)	<ul style="list-style-type: none"> <li>• Parameter chosen from beef experiments in literature (Moreira et al. 2014)</li> <li>• Experimental calibration using a prototype wheel could support re-definition of this parameter for beef striploin</li> <li>• Significant attenuation of the modelled static deformation occurs due to application of this property in the system model</li> <li>• The Kelvin-Voigt model using this parameter, could be assessed for suitability and possible replacement with a more complex model, following experimental calibration</li> </ul>

## Chapter 7

# Conclusions

Similar work in beef industry automation, robotics and meat cutting has reported limited success with substituting the tactile sensory modality with vision/imaging systems to guide automated tool trajectories. Large and dimensionally variable workpieces are impeding the implementation of cutting tool-trajectory guidance systems to the level currently improving the productivity and value-add of small-stock (sheep/pig) processors. Overcoming the physical challenges in realising automated beef-boning rooms could streamline preliminary 'front-end' processes. However, once primal cuts like beef striploin are removed from the relative stable carcass structure, the deforming soft-tissue characteristics become the dominant influence variable, impacting the real-time guidance of a cutting tool.

The relevance of pre-process measurements is likely to diminish as the tissues deform under contact-loads. The stiff, isotropic layer of fat tissue requires trimming to a specified uniform thickness, however there is also a significant structural interface with an anisotropic, viscoelastic beef muscle tissue component. Integrating the workpiece characteristics into the broader system model and embedding a tactile sensing capability into an automated fat trimming system, could complement the work currently underway in beef industry trials and research and potentially expedite the introduction of automated striploin fat trimmers into service.

Viscoelastic models and force-feedback systems are the focus of research into new tactile sensing approaches to improve the quality of robotic-assisted surgery. The literature has provided a valuable source of information to establish some preliminary design parameters

from which to build the models of deformation and tissue responses to rolling contact. The medical research into tactile sensing also provides ideas for the testing methodology to attain the parameters required:

1. Young's modulus for beef striploin fat tissue. This could be approximated using established techniques for compression and tensile tests of samples to estimate engineering stress and strain. Similar testing for shear stress may also prove useful, as Roark's static deformation modelling can be tuned for shear modulus parameters
2. Spring and damper constants for beef tissue. These could be approximated using the trailing arm and wheel assembly as an indenter, mounted in a vertical configuration under the test rig tool attachment fixture. The fixture would need to be actuated in a useful input mode such as step, ramp or cyclical function as it moves the arm/wheel and deforms the surface to known depths and rates of deformation

The expectations for tool-tissue interactions with a rolling indenter have been modelled, with reasonable results produced. The deformation and force magnitudes and rates are commensurate with similar studies in the literature. The parameters applied in models are evidence-based, and in the case of fat tissue elasticity, within an order of magnitude of similar approximations derived from formal tests using natural soft tissue samples.

The design is supported by functional and technical design specifications, derived from industry and academic research and the requirements of the project sponsor, the USQ Centre for Agricultural Engineering (CAE). The choice of wheel size affects the entire mechanical design, with the mechanism designed to minimise the physical size of components and simplify the interconnections and assembly of parts. Review of the quasi-steady modelling results suggests that having a range of different sized wheels available would be advantageous for dynamic testing. Optimising the wheel geometry, depth of deformation, speed of rolling, sampling rate and the application of preload and sensing state forces will require further analysis to balance the controllable parameters with the approximated soft tissue characteristics.

The instrument provides a relatively steady wheel reaction force over most of the operating range. There is a transition region around the wheel-tissue initial contact point, where the applied force is low and the arch segment is small. The arch model assumes a fixed lower end which is not really the case with striploin. The modelling used in the results

---

excludes data points from this small region ( $<10\text{mm}$ ). The magnitude of applied wheel reaction force increases to a relatively steady  $\approx 11 - 12\text{N}$  after  $\approx 10 - 20\text{mm}$  rolling contact. A preliminary operating range specification can be determined from these results with the viscoelastic response of the workpiece suggesting that low level, sluggish, over-damped deformations can be expected in the first  $20\text{mm}$  of wheel contact. When  $\approx 12\text{N}$  of spring force is available, the under-damped response is fairly consistent over the remaining surface contact area.

The transducer requirement is based on expectations of the wheel/trailing arm deflections as the workpiece deforms. The modelling suggests that discrimination of fat thickness layers in the target  $4\text{-}12\text{mm}$  range requires sub-millimetre transducer sensitivity to support analogue to digital discrimination of wheel trajectory variations over a  $\approx 10\text{mm}$  span. The wheel axle (Point C) position in the y-axis would be difficult to measure directly, with the parallel plates of the spring mechanism potentially more suitable as a mount/reflector for a time-of-flight (TOF) optical or ultrasonic distance sensor. The kinematics of the mechanism reduce the deflections of the spring length by  $\approx$  half the deflection of the wheel axle. Therefore, a millimetre deflection of the wheel results in  $0.5\text{-}0.6\text{mm}$  change in spring length; while the trailing arm angle varies by  $\approx 0.2\text{-}0.4^\circ$  for a  $1\text{mm}$  wheel deflection. A high resolution rotary encoder could sense angular deflection of the arm, but may also increase damping and reduce peak deflections of the wheel-tissue interactions. Therefore, the proposed transducer ((Sick 2020) see App.B) for a prototype is an ultrasonic sensor, either measuring spring length or possibly another point on the arm/wheel where reliable reflectivity and range could be achieved within transducer specifications.

A second transducer is also required to measure the workpiece surface y-axis elevation in front of the wheel. A Light Detection and Ranging (LiDAR) device is already installed on the tool-attachment gantry of the USQ CAE test rig. The non-deformed surface profile can be stored ahead of the wheel-contact and compared to the variations in wheel axle trajectory in close-to-real-time over the scanning period in Active Mode. With peak deformations likely to occur when the fat layer thickness is low, the wheel may tend to follow the hidden fat-meat interface while rolling over thin fat layers. With thicker fat and less deformation, the wheel would tend to follow the surface. Therefore, a comparison of surface profile and wheel trajectory could be used to identify regions of the workpiece where fat thickness is within or approaching the target specification ( $4\text{-}12\text{mm}$ ).

# References

- Associated Spring, Barnes Group Inc. (2005), 'Engineering guide to spring design', <http://www.faculty.fairfield.edu/wdornfeld/ME311/AssocSpringBarnes-SpringDesignHandbook.pdf>. Viewed 12 May 2020.
- Australian Competition & Consumer Commission (ACCC) (2017), 'Cattle and beef market study - final report', <https://www.accc.gov.au/system/files/ACCC%20Cattle%20and%20beef%20market%20studyFinal%20report.pdf>. Viewed 03 April 2020.
- Australian Government, D. o. D. (2019), 'Conducting and recording risk assessments', <http://drnet.defence.gov.au/dsrg/SPA/BWHSM/Pages/Implementation-Elements.aspx>.
- Beef Central (2019), 'Govt regulatory burden crippling processing competitiveness', <https://www.beefcentral.com/processing/govt-regulatory-burden-crippling-processing-competitiveness/>. Viewed 03 June 2020.
- Border, F., Khodabandehloo, K. & Brett, P. (2019), Robots for complex cutting operations in beef processing. paper to be presented at MMVP Australia.
- Comley, K. & Fleck, N. (2012), 'The compressive response of porcine adipose tissue from low to high strain rate', *International Journal of Impact Engineering* **46**.
- Condon, J. (2019), 'Beef boning automation next frontier for \$32m teys rocky research project', <https://www.beefcentral.com/processing/beef-boning-automation-next-frontier-for-32m-teys-rocky-research-project/>. Viewed 03 June 2020.
- Cook, J., Martchenko, V., Hughes, A., Shirazi, M. & Starling, S. (2017), 'Objective primal measurement (opm) – pack-off primal pick and pack: Fundamental vision and sensing evaluation', <https://www.mla.com.au/research-and-development/search-rd-reports/final-report-details/Objective-Primal-Measurement->



- OPM-Pack-off-Primal-Pick-and-Pack-Fundamental-Vision-and-Sensing-Evaluation/3618#. Viewed 08 April 2020.
- Cooney, B. (2020), Design of a rig for automated tissue discrimination in beef striploin during cutting and use of the rig for gathering data. Draft Dissertation, University of Southern Queensland.
- Damez, J.-L. & Clerjon, S. (2008), 'Meat quality assessment using biophysical methods related to meat structure', *Meat Science* **80**(1), 132,149.
- Damez, J.-L., Clerjon, S., Abouelkaram, S. & Lepetit, J. (2007), 'Dielectric behavior of beef meat in the 1–1500 khz range: Simulation with the fricke/cole–cole model', *Meat Science* **77**(4), 512,519.
- Davis, F., Sackey, M., Andrews, A. & Owusu-Ofori, S. (2017), 'Realistic friction coefficient model between a rolling cylindrical element and a deformable flat surface', *Tribology International* **109**, 252–257.
- Derington, A., Brooks, J., Garmyn, A., Thompson, L., Wester, D. & Miller, M. (2011), 'Relationships of slice shear force and warner-bratzler shear force of beef strip loin steaks as related to the tenderness gradient of the strip loin', *Meat Science* **88**(1), 203,208.
- Fairfax Media (2019), 'Automated beef boning to change australian meat processing.(livestock)', *Stock Journal (Adelaide, Australia)* .
- Greenwood, P. L., Gardner, G. E. & Ferguson, D. M. (2018), 'Current situation and future prospects for the australian beef industry—a review.(report)', *Asian - Australasian Journal of Animal Sciences* **31**(7), 1007–1016.
- Guire, G., Sabourin, L., Gogu, G. & Lemoine, E. (2010), 'Robotic cell for beef carcass primal cutting and pork ham boning in meat industry', *Industrial Robot: An International Journal* **37**(6), 532,541.
- Hibbeler, R. C. (2010), *Engineering Mechanics: Statics*, twelfth edition, si edition edn, Pearson Education South Asia, Singapore ;.
- Honikel, K. O. (1998), 'Reference methods for the assessment of physical characteristics of meat', *Meat Science* **49**(4), 447–457.

- Khodabandehloo, K. (2016), 'Technology evaluation for fat removal for beef striploins leaving a uniform thickness behind- final report', <https://www.ampc.com.au/uploads/pdf/Processing%20Technologies/2016.1032%20-%20Final%20M5%20report.pdf>. Viewed 03 May 2020.
- MatWeb (2020), 'Astm a228 steel (uns k08500)', [http://www.matweb.com/search/datasheet\\_print.aspx?matguid=4bcaab41d4eb43b3824d9de31c2c6849](http://www.matweb.com/search/datasheet_print.aspx?matguid=4bcaab41d4eb43b3824d9de31c2c6849). Viewed 26 June 2020.
- Meat & Livestock Australia Limited (2015), 'Objective carcass measurement', <https://www.mla.com.au/globalassets/mla-corporate/research-and-development/program-areas/automation-and-value-chain-technologies/objective-carcass-measurement.pdf>. Viewed 01 April 2020.
- Meat & Livestock Australia Limited (2019), 'State of the industry report. the Australian red meat and livestock industry', <https://www.mla.com.au/globalassets/mla-corporate/prices--markets/documents/trends--analysis/soti-report/mla-state-of-industry-report-2019.pdf>. Viewed 01 April 2020.
- Misumi Corporation (2020), 'Round wire springs', <https://us.misumi-ec.com/vona2/mech/M1200000000/M1202000000/M1202030000/M1202030100/>. Viewed 12 May 2020.
- Moreira, P., Liu, C., Zemiti, N. & Poignet, P. (2012), Soft tissue force control using active observers and viscoelastic interaction model, *in* '2012 IEEE International Conference on Robotics and Automation', IEEE, pp. 4660,4666.
- Moreira, P., Zemiti, N., Liu, C. & Poignet, P. (2014), 'Viscoelastic model based force control for soft tissue interaction and its application in physiological motion compensation', *Computer Methods and Programs in Biomedicine* **116**(2), 52,67.
- Nabil, E., Belhassen-Chedli, B. & Grigore, G. (2015), 'Soft material modeling for robotic task formulation and control in the muscle separation process', *Robotics and Computer Integrated Manufacturing* **32**, 37,53.
- Nason, J. (2020), 'Abattoirs working to reduce closure risk, as consumer meat demand soars', <https://www.beefcentral.com/processing/covid-19-are-abattoir-closures-possible/#gallery-1>. Viewed 20 August 2020.
- Nise, N. S. (2008), *Control systems engineering*, 5th ed. edn, Wiley, Hoboken, N.J.

- Rentschler, M. E., Dumpert, J., Platt, S. R., Lagnemma, K., Oleynikov, D. & Farritor, S. M. (2006), ‘Modeling, analysis, and experimental study of in vivo wheeled robotic mobility’, *IEEE Transactions on Robotics* **22**(2), 308–321.
- Roberts, A. J. (1994), *A one-dimensional introduction to continuum mechanics*, World Scientific, Singapore ;.
- Sangpradit, K., Liu, H., Dasgupta, P., Althoefer, K. & Seneviratne, L. D. (2011), ‘Finite-element modeling of soft tissue rolling indentation’, *IEEE Transactions on Biomedical Engineering* **58**(12), 3319–3327.
- S.G. Helibron Economic & Policy Consulting (2018), ‘Cost to operate and processing cost competitiveness - a combined report’, <https://www.ampc.com.au/2019/03/Cost-to-Operate-and-Processing-Cost-Competitiveness>. Viewed 03 May 2020.
- Sick (2020), ‘Distance sensors precision for measuring tasks’, [https://cdn.sick.com/media/docs/3/93/393/Product\\_segment\\_overview\\_Distance\\_Sensors\\_Precision\\_for\\_Measuring\\_Tasks\\_en\\_IM0061393.PDF](https://cdn.sick.com/media/docs/3/93/393/Product_segment_overview_Distance_Sensors_Precision_for_Measuring_Tasks_en_IM0061393.PDF) Viewed 10 October 2020.
- Sim, T. (2019), ‘Dexa plus robotics cost payback in three years on lamb’, <https://www.sheepcentral.com/dexa-plus-robotics-cost-payback-in-three-years-on-lamb/>. Viewed 03 June 2020.
- Steelwork, ECCS - European Convention for Constructional (2017), *Design of Joints in Steel Structures: Eurocode 3: Design of Steel Structures; Part 1-8 Design of Joints*, Wilhelm Ernst & Sohn Verlag fur Architektur und Technische, Berlin.
- U.S Government (2000), ‘Data item description: Operational concept description (ocd)’, [https://quicksearch.dla.mil/qsDocDetails.aspx?ident\\_number=205909](https://quicksearch.dla.mil/qsDocDetails.aspx?ident_number=205909). Viewed 24 April 2020.
- Wang, X.-D., Sun, Y.-H., Wang, Y., Hu, T.-J., Chen, M.-H. & He, B. (2009), ‘Artificial tactile sense technique for predicting beef tenderness based on fs pressure sensor’, *Journal of Bionic Engineering* **6**(2), 196,201.
- Weisstein, E., W. (2020), ‘Circular segment’, <https://mathworld.wolfram.com/CircularSegment.html>. From MathWorld–A Wolfram Web Resource, Viewed 01 May 2020.

- Wong, J.-Y. & Reece, A. (1967), 'Prediction of rigid wheel performance based on the analysis of soil-wheel stresses: Part ii. performance of towed rigid wheels', *Journal of Terramechanics* **4**(2), 7–25.
- Yoo, L., Gupta, V., Lee, C., Kavehpore, P. & Demer, J. L. (2011), 'Viscoelastic properties of bovine orbital connective tissue and fat: constitutive models.(report)', *Biomechanics and Modeling in Mechanobiology* **10**(6), 901–914.
- Young, W. C. & Budynas, R. G. (2002), *Roark's formulas for stress and strain*, 7th ed. edn, McGraw-Hill, New York.
- Zamora, F., Debiton, E., Lepetit, J., Lebert, A., Dransfield, E. & Ouali, A. (1996), 'Predicting variability of ageing and toughness in beef m. longissimus lumborum et thoracis', *Meat Science* **43**(3-4), 321–333.

Appendix A

**Project Specification**

## ENG 4111/2 Research Project

**Project Specification**

For: **Will Marshall**  
Topic: Real-time distributive tactile sensing system  
Supervisors: P. Brett  
F. Border  
Sponsorship: Faculty of Health, Engineering & Sciences

Project Aim: Determine promising approaches for automated real-time sensing that can be used to guide a cutting tool relative to deforming tissue interfaces during beef trimming processes.

Program: BENH - Instrumentation & Control

Version 2, 16 April 20

1. Investigate relevant literature, information and similar work involving beef industry automation, robotics and meat cutting.
2. Investigate relevant literature, information and similar work involving tissue deformation in response to applied force (stress), influence variables such as temperature and relevant sensing techniques and technology.
3. Model the tool-tissue interactions expected during operation of a roller-based sensing scheme used to discriminate features of tissue deformation in a beef workpiece.
4. Derive technical specifications and determine assumptions for a roller-based tactile sensor system design.
5. Design the tactile sensing scheme. Specify the range of operating conditions, output presentation and intended interface design for mechanical and electronic considerations. Develop engineering artefacts including specifications, drawings and verification plan.
6. Model the performance of the tactile sensing system, within the context of discriminating critical states and features of beef striploin primals with observable tissue structure and deformation.

*As time and resources permit:*

1. Manufacture the prototype tactile sensor roller sub-system.
2. Integrate the prototype sensor with interfacing electronics and test rig at USQ Centre for Agricultural Engineering (CAE).

Agreed:

Student Name: Will Marshall

Date: 16 April 20

Supervisor Name: Peter Brett

Date: 16 April 20

Supervisor Name: Fraser Border

Date: 16 April 20

# Appendix B

## Supporting Information

### B.1 Hazard Analysis and Risk Assessment

The hazard analysis/risk assessment has been conducted using an adaptation of the Defence Department engineering project risk assessment tool (Australian Government 2019).

The analysis tool includes provisions for Safety (S), Performance (P) and Environmental (E) categories of technical risk. Safety risks are those which impact on human health and safety, while performance risks are associated with the schedule and budget risks to project aims and objectives, including the impacts on physical hardware and support equipment/resources. Environmental risks are those which impact on the natural environment, with severities based on the cost of potential damage remediation and the ability of the environment to recover from impacts (Australian Government 2019).



ERP20-WM-002 - System Safety Hazard Analysis

Risk I.D.	Description of Hazard	Description of Consequence	Risk Substantiation (Establish and justify Likelihood, detail Consequence if required)	Risk Assessment			Enduring Mitigations (To eliminate or minimise the risk)	Mitigation Responsibility	Planned Applied By Date	Residual Risk Assessment			
				Risk Category	Likelihood	Consequence				Risk	Likelihood	Consequence	Risk
1	COVID-19	Flu-like illness and complications for existing health conditions	The project research and design development require considerable time, effort and extended periods of concentration. The impacts of this virus may include time away from the task including hospitalisation. The virus is highly contagious which increases the likelihood of transmission, the virus is also incurable which makes it highly likely that catching the disease will lead to symptoms.	S	Probable	Major	High	The student is working/studying from home for the duration of the 2020 academic year.  USQ have restricted access to laboratories and shared facilities including the library. There is no requirement for the student to attend these facilities.	Student and USQ	Applied in S1	Occasional	Major	Medium
2	Modelling does not represent behaviour of prototype instrument interacting with real beef samples	Rework of instrument specifications due to ineffective operating states and modes. New concepts of operation required.	The design decisions are based largely on predictions of the interactions between the instrument hardware architecture and highly variable and unpredictable behaviour of a deforming beef product. The research evidence base is not exclusively specific to beef processing applications, and the inhomogeneous characteristics of beef striploin. The restrictions described in Risk ID 1 also prevent the manufacture and experimental calibration/test of an instrument.	P	Probable	Moderate	Medium	The design is modular, to enhance maintainability through the design process, as research evidence becomes available and understanding is improved.  The design is aimed at prototype manufacture when resources become available, therefore supporting efforts to continue with physical instrument build and test as part of future work, using the artefacts produced in this project.	Student	S2 2020	Probable	Minor	Low
3	Electrical hazards	Shock, burns, electrocution	The Electronics subsystem for the prototype and experimentation is likely to be composed of bench-level laboratory equipment powered by 240VAC mains supply	S	Improbable	Critical	Medium	1. Use ELCB protection device in line with mains powered equipment. 2. USQ CAE laboratories may be installed with RCD	1. Student 2. USQ	Not planned for 2020 due to COVID-19 restrictions	Rare	Critical	Low
4	Carbon fibres	Dust / fibre ingress to skin, eyes, lungs	Carbon fibre / composite structures would be good for the Trailing Arm subsystem components, light weight and high rigidity. If this material is worked by hand/machine to manufacture parts then carbon fibres could present a hazard to health	S	Probable	Major	High	1. Use of personal protective equipment 2. Use of environmental guards and air quality controlled machines to do work 3. Substitute carbon fibre component design with safer material such as nylon/plastic	1,2,3. Student	Not planned for 2020 due to COVID-19 restrictions	Improbable	Major	Low
5													

Figure B.1: Hazard Analysis & Risk Assessment. Template adapted from (Australian Government 2019)

## B.2 Spring Datasheet

(Misumi Corporation 2020)

Instructions and precautions for the use of coil springs

- Always use a spring guide.**  
If used without a spring guide, problems such as buckling or bending of the spring body may occur, resulting in concentrated high stress on the inside of the bend and then leading to breakage. Be sure to use a spring guide, such as a shaft or outer diameter guide.  
\*In general the best results are obtained by inserting a shaft all the way through the coil spring from top to bottom to serve as an inner diameter guide.
- Clearance between spring inner diameter and shaft**  
The shaft diameter should be set approximately 1.0mm smaller than the inner diameter of the coil spring. If the clearance with the shaft is too small, the spring inner diameter will become worn by the shaft, leading to breakage occurring at the worn points. If the clearance is too large, buckling or other problems may occur. If the spring has a long free length (Free length ÷ Outer dia. = 4 or more), add a step to the shaft as shown on the left side of Figure 1 in order to prevent inner diameter contact when the spring body is bent.
- Clearance between spring outer diameter and counterbore hole**  
The counterbore hole diameter should be set approximately 1.5 mm larger than the coil spring outer diameter. If the clearance with the counterbore hole is too small, the outer diameter becomes restrained by expansion on the outer diameter side when the spring is flexed. The resulting concentration of stress may cause the spring to break. For a spring with a long free length, a counterbore hole shape such as that shown on the right side of Figure 1 is ideal.
- Avoid short guide lengths and shallow counterbore hole depths.**  
If the guide is too short, the spring may contact the end of the guide when the spring buckles, and the resulting friction may cause the spring to break. The guide length should be to a minimum of 150% of the initial set height. Also be sure to chamfer the shaft to approximately C3.
- Do not use in excess of the maximum allowable deflection (the maximum allowable deflection). (Do not use close to the solid height.)**  
If the spring is used beyond the maximum allowable deflection, high stress in excess of the calculated value occurs in the cross section. This can cause the spring to break. In addition, if the coil spring is used close to its solid height, the active coils will gradually adhere to each other, increasing the spring constant value and causing the load curve to rise as shown in Fig. 2. The resulting high stress may cause the spring to break. This also is a cause of strain. Do not use the coil spring in excess of the maximum allowable deflection.

- Set an initial deflection.**  
If there is a gap, the spring will move vertically, resulting in an impact force and causing bending of the body or buckling. Setting an initial deflection stabilizes the top and bottom ends of the spring.
- Do not use when scrap or other foreign substances are caught in the spring.**  
Foreign substances which get caught between the coils prevent that part of the coil spring from functioning as an active coil, forcing the other coils to deflect as shown in Fig. 3. This effectively reduces the number of active coils, increasing the stress on the spring, and eventually causing it to break. Be careful to prevent scrap or other foreign substances from entering the coils.
- Do not use in locations where the mounting surfaces are not sufficiently parallel.**  
If the mounting surfaces are insufficiently parallel, bending of the spring body occurs, resulting in concentrated high stress on the inside of the bend that may cause the spring to break. In addition, if the die is not sufficiently parallel, as shown in Figure 4, the spring may break due to bending or to exceeding the maximum allowable deflection. Ensure that the coil spring's mounting surfaces are as close to perfectly parallel as possible in order to prevent the maximum allowable deflection from being exceeded.
- Do not use coil springs in series.**  
If two coil springs are used in series, the springs will bend as shown in Figure 5. In some cases, the spring will ride up on the shaft or counterbore hole, causing breakage by the same mechanism described in ①. Variation in the spring load capacities will also result in the weaker spring being overcome by the stronger spring (Figure 6). This increases the deflection of the weaker spring, resulting in a difference in durability between the springs or else in breakage. In addition, when two springs are used in series, the spring constant of each is reduced by 1/2.
- Do not use two coil springs in a double-spring arrangement.**  
The use of two coil springs in a double-spring arrangement, as shown in Figure 7, may result in the inner coils being sandwiched between the outer coils (or vice versa) when the springs buckle. This can cause the coil springs to break for the same reason described in ④.
- Do not use the coil spring horizontally.**  
If the spring is used horizontally, the shaft will cause wear of the spring inner diameter, resulting in breakage at the points of wear.

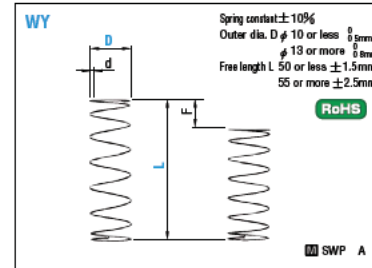
MISUMI endurance test conditions

① **Spring guide type**  
Inside shaft  
Shaft diameter: d 1.0 mm

② **Initial deflection**  
1.0mm

③ **Amplitude**  
Amount of deflection at the maximum allowable deflection

④ **Speed**  
180spm  
\* Durability count may vary depending on the conditions of use.



Spring constant		D12 and D14 are not available for WY type.							
D	Type	WY	WR	WF	WL	WT	WM	WH	WB
2					0.5 (0.05)				
3						1.5 (0.15)	2.0 (0.2)	2.0 (0.3)	3.0 (0.4)
4									4.0 (0.5)
5									
6									
8									
10									
12									
13									
14									
16									
18									
20									
22									
27									
Fmax.		F=LX75%	F=LX80%	F=LX85%	F=LX80%	F=LX85%	F=LX90%	F=LX95%	F=LX95%

Order **Catalog No.**  
WY13 60

Days to Ship

Quotation

Price Quotation

WY : Fmax. (Maximum allowable deflection) = LX75%

d	Solid height	F max.	Load N (kgf) max.	Catalog No.	Base unit price
Type	D	L			
0.16	1.0	3.75	0.38 [0.04]	WY3 5	
0.2	2.0	7.5	0.75 [0.08]	10	
0.23	3.6	11.2	1.12 [0.11]	15	
0.23	3.6	15	1.5 [0.15]	20	
0.25	5.5	18.7	1.87 [0.19]	25	
0.26	6.5	22.5	2.25 [0.23]	30	
0.2	1.1	3.75	0.38 [0.04]	WY4 5	
0.23	1.9	7.5	0.7 [0.08]	10	
0.23	1.9	11.2	1.1 [0.11]	15	
0.25	2.7	15	1.5 [0.15]	20	
0.29	5	18.7	1.8 [0.19]	25	
0.29	5	22.5	2.2 [0.23]	30	
0.32	7.7	26.2	2.6 [0.26]	35	
0.32	7.7	30	2.9 [0.3]	40	
0.25	1.7	7.5	0.7 [0.08]	WY5 10	
0.25	1.7	11.2	1.1 [0.11]	15	
0.3	3.2	15	1.5 [0.15]	20	
0.3	3.2	18.7	1.8 [0.19]	25	
0.35	6.3	22.5	2.2 [0.23]	30	
0.35	6.3	26.2	2.6 [0.26]	35	
0.38	9.2	30	2.9 [0.3]	40	
0.38	9.2	33.7	3.3 [0.34]	45	
0.38	9.2	37.5	3.7 [0.38]	50	
0.3	2.1	7.5	0.75 [0.08]	WY6 10	
0.32	2.8	11.2	1.1 [0.11]	15	
0.32	2.8	15	1.5 [0.15]	20	
0.35	4.1	18.7	1.8 [0.19]	25	
0.38	5.6	22.5	2.2 [0.23]	30	
0.38	5.6	26.2	2.6 [0.26]	35	
0.4	7.2	30	2.9 [0.3]	40	
0.4	7.2	33.7	3.3 [0.34]	45	
0.4	7.2	37.5	3.7 [0.38]	50	
0.45	12.2	41.2	4.0 [0.41]	55	
0.45	12.2	45	4.4 [0.45]	60	
0.45	12.2	48.7	4.8 [0.49]	65	
0.45	12.2	52.5	5.1 [0.53]	70	

d	Solid height	F max.	Load N (kgf) max.	Catalog No.	Base unit price
Type	D	L			
0.35	2.1	7.5	0.75 [0.08]	WY8 10	
0.38	3	11.2	1.1 [0.11]	15	
0.4	3.5	15	1.5 [0.15]	20	
0.4	3.5	18.7	1.8 [0.19]	25	
0.45	5.7	22.5	2.2 [0.23]	30	
0.45	5.7	26.2	2.6 [0.26]	35	
0.45	5.7	30	2.9 [0.3]	40	
0.45	5.7	33.7	3.3 [0.34]	45	
0.5	9	37.5	3.7 [0.38]	50	
0.5	9	41.2	4.0 [0.41]	55	
0.5	9	45	4.4 [0.45]	60	
0.5	9	48.7	4.8 [0.49]	65	
0.5	9	52.5	5.1 [0.53]	70	
0.5	3	11.2	2.26 [0.23]	WY10 15	
0.55	4.6	15	2.9 [0.3]	20	
0.55	4.6	18.7	3.7 [0.37]	25	
0.6	6.6	22.5	4.4 [0.45]	30	
0.6	6.6	26.2	5.1 [0.52]	35	
0.65	9.1	30	5.9 [0.6]	40	
0.65	9.1	33.7	6.6 [0.67]	45	
0.65	9.1	37.5	7.4 [0.75]	50	
0.65	9.1	41.2	8.1 [0.82]	55	
0.9	11.3	45	8.8 [0.9]	60	
0.9	11.3	48.7	9.6 [0.97]	65	
0.9	11.3	52.5	10.3 [1.05]	70	

d	Solid height	F max.	Load N (kgf) max.	Catalog No.	Base unit price
Type	D	L			
0.6	3.9	15	2.9 [0.3]	WY13 20	
0.65	5.1	18.7	3.7 [0.37]	25	
0.65	5.1	22.5	4.4 [0.45]	30	
0.7	6.7	26.2	5.1 [0.52]	35	
0.75	8.7	30	5.9 [0.6]	40	
0.75	8.7	33.7	6.6 [0.67]	45	
0.8	11.8	37.5	7.4 [0.75]	50	
0.8	11.8	41.2	8.1 [0.82]	55	
0.8	11.8	45	8.8 [0.9]	60	
0.85	15.3	48.7	9.6 [0.97]	65	
0.85	15.3	52.5	10.3 [1.05]	70	
0.65	3.6	15	2.9 [0.3]	WY16 20	
0.7	4.6	18.7	3.7 [0.37]	25	
0.75	5.7	22.5	4.4 [0.45]	30	
0.8	7	26.2	5.1 [0.52]	35	
0.85	9	30	5.9 [0.6]	40	
0.85	9	33.7	6.6 [0.67]	45	
0.9	11.3	37.5	7.4 [0.75]	50	
0.9	11.3	41.2	8.1 [0.82]	55	
0.9	11.3	45	8.8 [0.9]	60	
0.9	11.3	48.7	9.6 [0.97]	65	
0.9	11.3	52.5	10.3 [1.05]	70	

Load calculation method: Load = Spring constant × Deflection  
(SI unit) N = N/mm × F/mm  
kgf = kgf/mm × F/mm  
(kgf = N × 0.101972)

Ⓜ Neither end is ground for all WY type springs.  
Ⓜ The solid height values are for reference only.  
There may be some variation between lots.  
Ⓜ Operation count: 1 million  
Ⓜ Instructions and precautions for the use of coil springs P. 1397

## B.3 Ultrasonic Transducer Datasheet

(Sick 2020)



<p>13 mm ... 150 mm, 250 mm</p>	<p>20 mm ... 1,000 mm, 1,300 mm</p>	<p>20 mm ... 240 mm, 350 mm</p>
<p>≥ 0.1 mm</p>	<p>≥ 0.069 mm</p>	<p>≥ 0.069 mm</p>
<p>± 0.15 %</p>	<p>± 0.15 %</p>	<p>± 0.15 %</p>
<p>1 x 4 mA ... 20 mA (≤ 500 Ω) / 1 x 0 V ... 10 V (≥ 100 kΩ)</p>	<p>1 x 4 mA ... 20 mA (≤ 500 Ω) / 1 x 0 V ... 10 V (≥ 100 kΩ)</p>	<p>1 x 4 mA ... 20 mA (≤ 500 Ω) / 1 x 0 V ... 10 V (≥ 100 kΩ)</p>
<p>1 x PNP 1 x NPN 1 x push-pull PNP/NPN</p>	<p>1 x PNP 2 x PNP 1 x NPN 2 x NPN 1 x push-pull PNP/NPN 2 x push-pull PNP/NPN</p>	<p>1 x PNP 1 x NPN</p>
<p>✓, V1.1 (process data, parameterization, diagnosis, data storage)</p>	<p>✓, V1.1 (process data, parameterization, diagnosis, data storage)</p>	<p>-</p>
<p>Straight</p>	<p>Straight / angled</p>	<p>Straight</p>

- Reliable measurement, regardless of material color, transparency, gloss, or ambient light
- Ultrasonic technology in a small housing
- Detection, measurement, and positioning with ultrasonic technology
- Variants with PNP/NPN switching output, analog output or push-pull output with IO-Link
- Teach-in button
- Precise background suppression
- Immune to dirt, dust, humidity, and fog



→ [www.sick.com/UC4](http://www.sick.com/UC4)

- Reliable measurement, regardless of material color, transparency, gloss, or ambient light
- Sensing ranges up to 1,300 mm
- Short metal or plastic M18 housing from 42 mm in length
- Straight or angled design
- Immune to dirt, dust, humidity, and fog
- Versatile interfaces including IO-Link available



→ [www.sick.com/UM18](http://www.sick.com/UM18)

- Reliable measurement, regardless of material color, transparency, gloss, or ambient light
- Very short and rugged M12 metal housing
- Variants with PNP/NPN switching output or analog output
- Immune to dirt, dust, humidity, and fog
- Detection, measurement, or positioning with ultrasound technology
- Cable teach-in



→ [www.sick.com/UM12](http://www.sick.com/UM12)

# Appendix C

## Models and Code

### C.1 Bill of Materials (BOM) Model

Design calculations presented in Section 3 were applied in the Bill of Materials model (.xls) to define the build parameters for the prototype instrument. User input is required for design decisions:

1. wheel radius  $Rw$
2. wheel bore  $Bw$
3. wheel hub width  $Hw$
4. meat surface arch radius  $Rms$
5. tool-support elevation  $AZ$ .

Options are presented for the positioning of the spring mechanism, where the maximum space available for the springs and the minimum space remaining after full compression are used to find a suitable compression ratio spring at a suitable free-length. Weight, balance, force and geometric constants/variables are then available to the static force and system models.





## C.2 BOM and System Model Faceplate

The BOM model also has a faceplate, where design and modelling parameters are presented:

TSI System Model			Input conditions				Output conditions									
Modelled Prototype Instrument Targets			Work piece	Arm Dimensions			Spring Dimensions			Spring Properties			Instrument Specifications			
Model	Configuration I.D	Model Phase	Rms	AC	Wheel Rw	Spring Mount AB:AC	Spring L <sub>preload</sub>	Spring L <sub>minimum</sub>	Working Comp. Ratio (L <sub>pre</sub> -L <sub>min</sub> ) / L <sub>pre</sub>	Selected Spring L <sub>free</sub>	Selected Spring L <sub>min</sub>	Max Force (F <sub>max</sub> )	Instrument Preload Force (F <sub>preload</sub> )	Instrument Weight (F <sub>My</sub> )	Instrument Stiffness (k)	Instrument Span Δθ <sub>1</sub>
1	TSI-35/10-6/15-100-1.8/100	1	0.100	0.301	0.035	0.200	0.015	-0.013	1.877	0.070	0.018	12.43	7.26	1.75	200.00	0.45
Modelling Objectives		2	tfat		Ww	0.400	0.071	0.018	0.748				1.75			
		3	0.010	AZ	0.010	0.600	0.128	0.049	0.617				1.75	1.75	200.00	25.72
		4	X	0.285		0.744	0.169	0.071	0.577				1.75	F <sub>pre</sub> Target	kTarget	deg
		5	0.240			1.000	0.242	0.111	0.540				1.75			
			m	m		m	m		m	m	N	N	N	N/m	rad	

Figure C.2: BOM and System Modelling Faceplate



## C.3 Model/Function Code (MATLAB)

### System Model - Tactile Sensing Instrument & Beef Striploin

The function `MeatModel.m` is the model of instrument deflection while traversing a specified thickness of fat layer over a representative sample of beef striploin exhibiting viscoelastic response to applied forces under the wheel.

Listing C.1: `StaticForceModelNoDeformation`.

```

%% SET FLAG FOR DATA – FAT THICKNESS
%*****
%
flag =4; % CHANGE THICKNESS FLAG HERE
%
%*****
%% IMPORT DATA FROM XL
%
clc
MeatModelImports = importfile('MeatModelImports.xlsx','Sheet1',2,127);
ForceMAX = MeatModelImports.FC;
DEFRoark4 = MeatModelImports.mmDEF4;
DEFangle4 = MeatModelImports.DefAngle4;
DEFRoark12 = MeatModelImports.mmDEF12;
DEFangle12 = MeatModelImports.DefAngle12;
DEFRoark20 = MeatModelImports.mmDEF20;
DEFangle20 = MeatModelImports.DefAngle20;
DEFRoark30 = MeatModelImports.mmDEF30;
DEFangle30 = MeatModelImports.DefAngle30;
DEFRoark50 = MeatModelImports.mmDEF50;
DEFangle50 = MeatModelImports.DefAngle50;
CyNoDef = MeatModelImports.CyNoDef;
dLdy = MeatModelImports.dLdy;
%
% CYvar4 = DEFRoark4 .* sin(DEFangle4);
% CYvar12 = DEFRoark12 .* sin(DEFangle12);
% CYvar20 = DEFRoark20 .* sin(DEFangle20);
% CYvar30 = DEFRoark30 .* sin(DEFangle30);
% CYvar50 = DEFRoark50 .* sin(DEFangle50);

%
%% Meat
Bmeat = 14.7; % Viscosity
Kmeat = 192.7; % Stiffness
%
```

```

%% Instrument
Kinst = 200; % Spring stiffness
dlspringdCy = -dLdy; % spring length change to Cy elevation change
Minst = 1.75/9.81; % Mass
%
%% Choose sample
if flag == 4
    DEFroark = DEFroark4;
    DEFangle = DEFangle4;

end
if flag == 12
    DEFroark = DEFroark12;
    DEFangle = DEFangle12;

end
if flag == 20
    DEFroark = DEFroark20;
    DEFangle = DEFangle20;

end
if flag == 30
    DEFroark = DEFroark30;
    DEFangle = DEFangle30;

end
if flag == 50
    DEFroark = DEFroark50;
    DEFangle = DEFangle50;

end

%
%% Roark's Deformation under constant force
% Calculate the Roark system parameters for each deformation over the
% workpiece
wnRoark = zeros(size(DEFroark));
zetaRoark = zeros(size(DEFroark));
gainRoark = zeros(size(DEFroark));
for i = 1:length(ForceMAX)
    wnRoark(i) = sqrt(Kmeat./Minst);
    zetaRoark(i) = (Bmeat.*wnRoark(i))./(2.*Kmeat);
    gainRoark(i) = ((DEFroark(i).*Kmeat)./ForceMAX(i))./Kmeat;
end
%
% Calculate the open loop Roark Deformation
%to = 0:0.001:1;
%
%for io = 1:length(to)
    %fRoark = FCo*(gaino * (1 - exp(-wn.*t)).*(1 + wn.*t)); ...
    %critical damping
    %underdamped

```

```

%fRoark = FCo*(gaino * (1 - exp(-zetao.*wno.*to).* ...
%(cos(wno.*sqrt((1 - zetao.^2)).*to) + (zetao./sqrt(1 - zetao.^2)).* ...
%sin(wno.*sqrt((1 - zetao.^2)).*to)))));
%overdamped
%fRoark = FCo*(gainRoark * (1 - exp(-zetaRoark.*wnRoark.*to).* ...
%(cosh(wnRoark.*sqrt((zetaRoark.^2 - 1)).*to) + ...
%(zetaRoark./sqrt(zetaRoark.^2 - 1)).*sinh(wnRoark.*sqrt((zetaRoark.^2 - 1)
%end
%

%% Wheel-Tissue Deformation under TSI force conditions
%
brackets = zeros(size(DEFRoark));
wnInst = zeros(size(DEFRoark));
zetaInst = zeros(size(DEFRoark));
gainInst = zeros(size(DEFRoark));
Kfeedback = zeros(size(DEFRoark));
%
for j = 1:length(ForceMAX)
    Kfeedback(j) = Kinst.*dlspringdCy(j).*(sin(DEFangle(j)));
    brackets(j) = Kmeat.*(1 + Kfeedback(j).*DEFRoark(j));
    wnInst(j) = sqrt(brackets(j)./Minst);
    zetaInst(j) = (Bmeat.*wnInst(j))./(2.*brackets(j));
    gainInst(j) = ((DEFRoark(j).*Kmeat)./ForceMAX(j))./brackets(j);
end
%
t = 0:0.001:1;
fInst = zeros(length(DEFRoark),length(t));
for k = 1:length(ForceMAX)
    if zetaInst(k) < 1 % underdamped
        for l = 1:length(t)
            fInst(k,l) = ForceMAX(k).*(gainInst(k) .* ...
            (1 - exp(-zetaInst(k).*wnInst(k).*t(l)).* ...
            (cos(wnInst(k).*sqrt((1 - zetaInst(k).^2)).* ...
            t(l)) + (zetaInst(k)./sqrt(1 - zetaInst(k).^2)).* ...
            sin(wnInst(k).*sqrt((1 - zetaInst(k).^2)).*t(l)))));
        end
    elseif zetaInst(k) == 1 % critically damped
        for l = 1:length(t)
            fInst(k,l) = ForceMAX(k).*(gainInst(k) * ...
            (1 - exp(-wnInst(k).*t(l)).*(1 + wnInst(k).*t(l))));
        end
    else %overdamped
        for l = 1:length(t)
            fInst(k,l) = ForceMAX(k).*(gainInst(k) * ...
            (1 - exp(-zetaInst(k).*wnInst(k).*t(l)).* ...
            (cosh(wnInst(k).*sqrt((zetaInst(k).^2 - 1)).* ...
            t(l)) + (zetaInst(k)./sqrt(zetaInst(k).^2 - 1)).* ...
            sinh(wnInst(k).*sqrt((zetaInst(k).^2 - 1)).*t(l))));
        end
    end
end
end

```

```

end

%

%
%plot(fInst(:,25));

% CyDEF = fInst(:,25).*sin(DEFangle);
% plot(CyDEF);
filename = 'MeatModelImports.xlsx';
%xlswrite(filename, fInst(:,25), 2, 'C1:C126');

[maxValue50, indexOfMax50] = max(fInst(50,:));

[maxValue126, indexOfMax126] = max(fInst(126,:));

peakRange = [indexOfMax50 indexOfMax126];

sampleTime = mean(peakRange);

figure(1)
plot(fInst(1,:))
hold on
plot(fInst(10,:))
hold on
plot(fInst(20,:))
hold on
plot(fInst(50,:))
hold on
plot(fInst(80,:))
hold on
plot(fInst(100,:))
hold on
plot(fInst(126,:))
hold off
title(['Depth_of_Total_Deformation_and_Time-response_for_', ...
       num2str(flag), 'mm_Fat-Layer_Thickness']);
xlabel('Time_After_Wheel_Contact_(ms)');
ylabel('Depth_of_Total_Deformation_(m)');
legend('Initial_Wheel-contact_Point', '10mm_Wheel-travel_Point', ...
       '20mm_Wheel-travel_Point', '50mm_Wheel-travel_Point', ...
       '80mm_Wheel-travel_Point', '100mm_Wheel-travel_Point', ...
       'Final_Wheel-contact_Point');
legend('Location', 'southeastoutside')
text(sampleTime,0.0005, ['\leftarrow Sample_Time', ...
                        num2str(sampleTime), 'ms_and_Wheel_Velocity_', ...
                        num2str(round(1/(sampleTime/1000))), 'mm/s']);
%% DATA FROM EXPERIMENTS
%
averageSampleTime = median([44 49 55 66 114]);

```

```

fastSampleTime = round(averageSampleTime/1.58);
slowSampleTime = averageSampleTime*2;
%
%% Instrument behaviour
% Use instrument from 50mm to 126mm travel over the workpiece
span = (50:126);
%*****
figure(2);
%*****
if flag == 4
    defSample4 = fInst(span, averageSampleTime);
    fastdefSample4 = fInst(span, fastSampleTime);
    slowdefSample4 = fInst(span, slowSampleTime);
    deltaCyaverage4 = defSample4.*sin(DEFangle4(averageSampleTime));
    deltaCyfast4 = defSample4.*sin(DEFangle4(fastSampleTime));
    deltaCyslow4 = defSample4.*sin(DEFangle4(slowSampleTime));
end
if flag == 12
    defSample12 = fInst(span, averageSampleTime);
    fastdefSample12 = fInst(span, fastSampleTime);
    slowdefSample12 = fInst(span, slowSampleTime);
    deltaCyaverage12 = defSample12.*sin(DEFangle12(averageSampleTime));
    deltaCyfast12 = defSample12.*sin(DEFangle12(fastSampleTime));
    deltaCyslow12 = defSample12.*sin(DEFangle12(slowSampleTime));
end
if flag == 20
    defSample20 = fInst(span, averageSampleTime);
    fastdefSample20 = fInst(span, fastSampleTime);
    slowdefSample20 = fInst(span, slowSampleTime);
    deltaCyaverage20 = defSample20.*sin(DEFangle20(averageSampleTime));
    deltaCyfast20 = defSample20.*sin(DEFangle20(fastSampleTime));
    deltaCyslow20 = defSample20.*sin(DEFangle20(slowSampleTime));
end

if flag == 30
    defSample30 = fInst(span, averageSampleTime);
    fastdefSample30 = fInst(span, fastSampleTime);
    slowdefSample30 = fInst(span, slowSampleTime);
    deltaCyaverage30 = defSample30.*sin(DEFangle30(averageSampleTime));
    deltaCyfast30 = defSample30.*sin(DEFangle30(fastSampleTime));
    deltaCyslow30 = defSample30.*sin(DEFangle30(slowSampleTime));
end

if flag == 50
    defSample50 = fInst(span, averageSampleTime);
    fastdefSample50 = fInst(span, fastSampleTime);
    slowdefSample50 = fInst(span, slowSampleTime);
    deltaCyaverage50 = defSample50.*sin(DEFangle50(averageSampleTime));
    deltaCyfast50 = defSample50.*sin(DEFangle50(fastSampleTime));
    deltaCyslow50 = defSample50.*sin(DEFangle50(slowSampleTime));
end
%

```

```

plot(-deltaCyaverage50);
hold on
plot(-deltaCyaverage30);
hold on
plot(-deltaCyaverage20);
hold on
plot(-deltaCyaverage12);
hold on
plot(-deltaCyaverage4);
hold on

title(['Depth_of_y-axis_Deformation: Average_Sample_Time', ...
       num2str(averageSampleTime), 'ms_and_Wheel_Velocity', ...
       num2str(round(1/(averageSampleTime/1000))), 'mm/s']);
xlabel('Position_along_Surface_from_50mm_to_End_(mm)');
ylabel('Depth_of_y-axis_Deformation_(m)');
legend('50mm_Thickness', '30mm_Thickness', '20mm_Thickness', ...
       '12mm_Thickness', '4mm_Thickness');
legend('Location', 'southeast')

%*****
figure(3);
%*****
%
%
plot(-deltaCyfast50);
hold on
plot(-deltaCyfast30);
hold on
plot(-deltaCyfast20);
hold on
plot(-deltaCyfast12);
hold on
plot(-deltaCyfast4);
hold on
%
title(['Depth_of_y-axis_Deformation: Fast_Sample_Time', ...
       num2str(fastSampleTime), 'ms_and_Wheel_Velocity', ...
       num2str(round(1/(fastSampleTime/1000))), 'mm/s']);
xlabel('Position_along_Surface_from_50mm_to_End_(mm)');
ylabel('Depth_of_y-axis_Deformation_(m)');
legend('50mm_Thickness', '30mm_Thickness', '20mm_Thickness', ...
       '12mm_Thickness', '4mm_Thickness');
legend('Location', 'southeastoutside')

%*****
figure(4);

```

```
%*****  
%  
%  
plot(-deltaCyslow50);  
hold on  
plot(-deltaCyslow30);  
hold on  
plot(-deltaCyslow20);  
hold on  
plot(- deltaCyslow12);  
hold on  
plot(-deltaCyslow4);  
hold on  
%  
title ([ 'Depth_of_y-axis_Deformation: Slow_Sample_Time', ...  
        num2str(slowSampleTime), 'ms_and_Wheel_Velocity', ...  
        num2str(round(1/(slowSampleTime/1000))), 'mm/s' ]);  
xlabel( 'Position_along_Surface_from_50mm_to_End(mm)' );  
ylabel( 'Depth_of_y-axis_Deformation(m)' );  
legend( '50mm_Thickness', '30mm_Thickness', '20mm_Thickness', ...  
        '12mm_Thickness', '4mm_Thickness' );  
legend( 'Location', 'southeastoutside' )
```